The Thesis Committee for Yaser Abdullah Alzayer
Certifies that this is the approved version of the following thesis:

Fracture Growth Kinematics in Tight Sandstone Reservoirs

APPROVED BY
SUPERVISING COMMITTEE:

Supervisor:

Peter Eichhubl

Stephen E. Laubach

Whitney Behr

William Fisher

Fracture Growth Kinematics in Tight Sandstone Reservoirs

by

Yaser Abdullah Alzayer, B.S.

Thesis

Presented to the Faculty of the Graduate School of

The University of Texas at Austin

in Partial Fulfillment

of the Requirements

for the Degree of

Master of Science in Geological Sciences

The University of Texas at Austin

August 2014

Dedication

This thesis is dedicated to my parents, fiancé, and family for their love, endless support, and encouragement.

Acknowledgements

I would like to thank my adviser Dr. Peter Eichhubl for his supervision, guidance, and incredible support throughout my graduate school career at UT. His editorial comments have improved this work significantly. I thank my thesis committee members Dr. Steve Laubach, Dr. Whitney Behr, and Dr. William Fisher for taking time to review this work and providing insightful feedback. I would also like to acknowledge Dr. Laubach for teaching me his bridge reconstruction method and having numerous discussions with me on fractures in tight sandstones. I would like to thank Dr. Randy Marrett for having discussions with me on fractures and brittle structures and their growth and spatial organization in the Earth's crust. This work was supported by the Industrial Associates of the Fracture Research and Application Consortium at the Bureau of Economic Geology. I am very grateful for my employer (Saudi Aramco) for providing scholarship support and time to pursue a master's degree. I thank Maher Almarhoon and Dave Cantrell of Saudi Aramco for their constant support and encouragement.

I would like to acknowledge the Bureau of Economic Geology staff for their support and assistance throughout my work. I am grateful for Dr. Esti Ukar for training me on the SEM, petrographic microscope, and providing a cheerful atmosphere at the FRAC group. I thank Dr. András Fall for teaching me about fluid inclusions, applying epoxy to samples, and polishing thin sections. I thank Patrick Smith for providing training on carbon coating and for supporting my work at the SEM lab. I thank James Donnelly and the BEG core warehouse staff for assisting in core viewing and sample cutting. I am also thankful for Sarah Elliot help and assistance on multiple occasions from carbon coating to sending samples.

I would like to acknowledge my fellow graduate students and friends in Austin who provided me with moral and academic support; I will forever cherish their friendship. I thank Canalp Ozkul, Nike Tokan-Lawal, Jon Major, and Lauren Copley for providing feedback and support whenever I needed it and engaging in discussions. I would like to thank Owen Callahan for assisting me in sample collection in Scotland and unknowingly motivating me to improve my fitness. Finally, I would not be where I am today without the support and guidance of my parents and family. I am also very thankful for my fiancé for her love, support, and understanding during the busy times.

Abstract

Fracture Growth Kinematics in Tight Sandstone Reservoirs

Yaser Abdullah Alzayer, M.S. Geo. Sci.

The University of Texas at Austin, 2014

Supervisor: Peter Eichhubl

Opening-mode fractures—joints and veins—are widespread structures in sedimentary rocks even in slightly deformed and flat-lying sequences. Understanding the growth and connectivity of fractures in low permeability sandstone reservoirs is essential for optimal hydrocarbon exploitation. In a linear elastic fracture mechanics framework, it is generally assumed that fractures widen in aperture while they propagate in length or height. However, it is also conceivable that a phase of proportional aperture to length or height growth is followed by a phase of aperture growth with relatively slow or arrested tip propagation. Slow propagation relative to aperture opening can occur by non-elastic deformation processes or if the material elastic properties change over time. Fracture propagation in length or height can be halted by material strength heterogeneities.

To test for concurrent length versus aperture growth of these fractures, I reconstructed the crack-seal opening history for multiple cement bridges sampled at different distances from the tip of three opening-mode fractures in Travis Peak Sandstone of the SFOT-1 well, East Texas. Crack-seal cement bridges have been interpreted to form by repeated incremental fracture opening and subsequent precipitation of quartz cement

that bridges the fractures. Crack-seal cement textures were imaged using a scanning electron microscope with a cathodoluminescence detector, and the number and thickness of crack-seal cement increments determined. Trends in crack-seal increments number and thickness are consistent with fast initial fracture propagation relative to aperture growth, followed by a stage of slow propagation and pronounced aperture growth. Cumulative fracture opening displacement based on palinspastic reconstruction of two cement bridges was compared to analytical solutions for a stationary and a propagating fracture aperture as a function of position relative to the fracture tip in an elastic medium. Based on this comparison, I conclude that the crack-seal cement record reflects largely the phase of dominant aperture growth and subcritical fracture propagation under constant loading stress.

Table of Contents

Abstract vii

List of Tables xi

List of Figures xiv

Chapter 1: Introduction 1

Terminology 4

Chapter 2: Fracture Growth Processes 6

Fracture Initiation and Propagation 6

Fracture Geometry 18

Fracture Growth Modeling 20

Chapter 3: Methods 23

Selection Criteria and Sampling Procedures 23

SEM Sample Preparation Procedure 28

SEM- Cathodoluminescence Imaging 29

Crack-Seal Measurements 33

Quartz Bridge Restoration 36

Comparison to Linear Elastic Fracture Mechanics Predictions 38

Chapter 4: Growth Kinematics of Opening-Mode Fractures in the Cretaceous Travis Peak Formation, East Texas 41

Introduction 41

Geologic Background 44

Methods 46

Results 50

Discussion 56

Conclusions 65

Chapter 5: Evolution of Crack-Seal Fracture Shape 66

Observations In Fracture Kinematic Aperture 66

Discussion: 74

Chapter 6: Conclusions 80

Appendix A: Observations in Crack-seal Increments 83

Appendix B: Fractures and Bridges Data 86

SFOT-1-10,108.3- Fracture 1 87

SFOT-1-10,108.3- Fracture 2 110

10,106'-Fracture 1- Bridge Images and Measurements 127

SFOT-1-10,106.7-10107 131

Appendix C: Bridge Reconstruction 161

SFOT-1-10106.85- Bridge 6 reconstruction 161

References 164

Vita…. 178

List of Tables

Table 3.1: List of examined samples. 25

Table 4.1. Fracture and material properties used for calculation of cumulative fracture opening displacement.....64

Table 5.1: Fracture properties for Travis Peak fracture 1 in SFOT-1- 10,106' 69

Table 5. 2 : Fracture properties for Travis Peak fracture 2 in SFOT-1 samples 10,106.7-10,107 ft.....71

Table B. 1: Summary of cement bridge measurements in Fracture 1- SFOT-1-10,108.3'. 87

Table B. 2: Bridge 7 crack-seal measurements.....89

Table B. 3: Bridge 8 crack-seal measurements.....91

Table B. 4: Bridge 9 crack-seal measurements.....93

Table B. 5: Bridge 10-11 crack-seal measurements. 95

Table B. 6: Bridge F crack-seal measurements. 97

Table B. 7: Bridge G crack-seal measurements.....99

Table B. 8: Bridge H crack-seal measurements.....101

Table B. 9: Bridge D crack-seal measurements.....103

Table B. 10: Bridge 1 crack-seal measurements.....105

Table B. 11: Bridge C crack-seal measurements. 107

Table B. 12: Bridge E crack-seal measurements. 109

Table B. 13: Summary of cement bridge measurements in Fracture 2- SFOT-1-10,108.3'. 110

Table B. 14: Bridge 5 crack-seal measurements.....112

Table B. 15: Bridge 3 crack-seal measurements.....114

Table B. 16: Bridge 2 crack-seal measurements.....116
Table B. 17: Bridge 6 crack-seal measurements.....118
Table B. 18: Bridge B crack-seal measurements. 120
Table B. 19: Bridge J crack-seal measurements. 122
Table B. 20: Bridge I crack-seal measurements. 124
Table B. 21: Bridge 1 crack-seal measurements.....128
Table B. 22: Key calculated parameters for Bridge 1.....128
Table B. 23: Measurements for the partial crack-seal bridge next to bridge 1....129
Table B. 24: Key parameters for the partial crack-seal bridge next to bridge 1 ..129
Table B. 25: Summary of cement bridge measurements in Fracture SFOT-1-10,106.7-10,107'.....131
Table B. 26: 10107-Bridge 7 crack-seal measurements. 132
Table B. 27: 10107-Bridge 6 crack-seal measurements. 133
Table B. 28: 10107-Bridge 2 crack-seal measurements. 135
Table B. 29: 10107-Bridge 1 crack-seal measurements. 136
Table B. 30: 10107-Tip Bridge 3 crack-seal measurements.....137
Table B. 31: 10107- Bridge 3 crack-seal measurements. 138
Table B. 32: 10107- Bridge 4 crack-seal measurements. 139
Table B. 33: 10107-Tip bridge crack-seal measurements. 140
Table B. 34: 10107-Bridge 5 crack-seal measurements. 142
Table B. 35: 10107-Bridge 8 crack-seal measurements. 143
Table B. 36: 10107-Bridge 9 crack-seal measurements. 144
Table B. 37: 10107-Bridge 10 crack-seal measurements. 145
Table B. 38: 10107-Tip bridge 2 crack-seal measurements. 147
Table B. 39: 10107-Bridge 11 crack-seal measurements. 149

Table B. 40: 10106.85-Bridge 6 crack-seal measurements. 151
Table B. 41: 10106.85-Bridge 5 crack-seal measurements. 153
Table B. 42: 10106.85-Bridge 1 crack-seal measurements. 156
Table B. 43: 10106.85-Bridge 1 key calculated parameters with comparison of counted versus estimated number of increments. 156
Table B. 44: 10106.85-Bridge 4 crack-seal measurements. 157
Table B. 45: 10106.85'-Bridge 3 crack-seal measurements. 159
Table B. 46: 10106.85-Bridge 2 crack-seal measurements. 160
Table C. 1: Linear elastic fracture models parameter used in Figure C.3. 163

List of Figures

Figure 1.1: Fracture types based on the sense of displacement. 5

Figure 2.1: A model for fracture linkage evolution 9

Figure 2.2: Model of crack-seal cement bridge evolution in sandstone 12

Figure 2.3: Model of crack-seal bridge evolution.....13

Figure 2.4: Types of penny-shaped fracture loading and displacement 15

Figure 2.5: Penny-shaped fracture in 3D 20

Figure 3.1: A diagram showing the method used for complete fracture preservation while cutting thin section chips.....26

Figure 3.2: A plane-polarized photomicrograph of a quartz bridge 27

Figure 3.3: Top and side views of a mounted standard thin section.....29

Figure 3.4: The scanning electron microscope system utilized in this study.....31

Figure 3.5: Blue filter SEM-CL image of SFOT-1-10107 Fracture 34

Figure 3.6: An example of an apparently partial crack-seal bridge.....35

Figure 3.7: A schematic of a crack-seal bridge evolution showing the method of interpreting crack-seal relative age 37

Figure 3.8: A panchromatic image of a quartz crack-seal bridge with bordering lateral euhedral quartz cement. 38

Figure 4.1: Location of the SFOT-1 and SFE-2 wells. 46

Figure 4.2: Fracture images of SFOT-1 well, depth: 10,107 ft.....49

Figure 4.3: Examples of increment thickness and kinematic aperture measurements on SEM-CL image of a crack-seal bridge.....50

Figure 4.4: Photomicrograph of two partially cemented en-echelon fractures imaged along strike (SFOT-1 well: depth 10,108.3')....52

Figure 4.5: Photomicrograph of a partially cemented fracture imaged parallel to the fracture dip (SFOT-1 well, depth of 10,107')....53
Figure 4.6: Selected stages of a bridge reconstruction labeled by number of increments....54
Figure 4.7: Selected stages of a second bridge reconstruction labeled by number of increments....55
Figure 4.8: Models for fracture growth by propagation and aperture increase....59
Figure 4.9: Predicted trends in thickness and number of fracture opening displacement increments for fracture kinematic models....60
Figure 4.10: Cumulative fracture opening displacement for the reconstructed bridge in Figure 4.6....63
Figure 5.1: Kinematic aperture profile from SEM-CL images for fracture 1....68
Figure 5.2: Kinematic aperture profile from measurements on SEM-CL images of part of fracture 2 sampled along its height....70
Figure 5.3: Combined kinematic aperture profile measured from SEM-CL images for two fractures....72
Figure 5.4: Blue-filter SEM-CL image of the overlap zone marked in figure 5.3 between two fractures....73
Figure 5.5: Schematic drawing of a cohesive-crack, uniformly bridged-crack, and a bridged-crack with discontinuous reinforcements....75
Figure 5.6: Comparison between cohesive-crack and bridged-crack....76
Figure 5.7: Three progressive stages of sigmoidal fracture evolution....79
Figure A.1: A schematic drawing showing growth triangles....84
Figure B. 1: Petrographic image of SFOT-1-1,108.3 ft....86
Figure B. 2: Kinematic aperture of Fracture 1 at examined bridges locations....87

Figure B. 3: Panchromatic SEM-CL image of Bridge 7.....88
Figure B. 4: Panchromatic SEM-CL image of bridge 8 90
Figure B. 5: Panchromatic SEM-CL image of bridge 9. 92
Figure B. 6: Panchromatic SEM-CL image of bridges 10 and 11 94
Figure B. 7: Panchromatic SEM-CL image of bridge F. 96
Figure B. 8: Panchromatic SEM-CL image of bridge G. 98
Figure B. 9: Panchromatic SEM-CL image of bridge H. 100
Figure B. 10: Panchromatic SEM-CL image of bridge D. 102
Figure B. 11: Panchromatic SEM-CL image of bridge 1 104
Figure B. 12: Panchromatic SEM-CL image of bridge C.....106
Figure B. 13: Panchromatic SEM-CL image of bridge E.....108
Figure B. 14: Fracture 2 kinematic aperture profile from examined bridges. 110
Figure B. 15: Panchromatic SEM-CL image of bridge 5 111
Figure B. 16: Panchromatic SEM-CL image of bridge 3 113
Figure B. 17: Panchromatic SEM-CL image of bridge 2 115
Figure B. 18: Panchromatic SEM-CL image of bridge 6. 117
Figure B. 19: Panchromatic SEM-CL image of bridge B.....119
Figure B. 20: Panchromatic SEM-CL image of bridge J.....121
Figure B. 21: Panchromatic SEM-CL image of bridge I. 123
Figure B. 22: A thin section view under plane polarized light microscope of en-echelon fractures 125
Figure B. 23: SEM-Cl image (blue filter) of the isolated fracture at 10,106'.....126
Figure B. 24: Panchromatic SEM-CL image of bridge 1 of fracture 1.....127
Figure B. 25: Plane polarized images of a continuous fracture sample (SFOT-1-10106.7-10107).....130

Figure B. 26: Panchromatic SEM-CL image of 10107-Bridge 7. 132
Figure B. 27: Panchromatic SEM-CL image of 10107-Bridge 6. 133
Figure B. 28: Color Mosiac SEM-CL image of 10107-Bridge 2 134
Figure B. 29: Panchromatic SEM-CL image of 10107-Bridge 1. 135
Figure B. 30: Panchromatic SEM-CL image of 10107-Tip bridge 3. 137
Figure B. 31: Panchromatic SEM-CL image of 10107- Bridge 3. 138
Figure B. 32: Panchromatic SEM-CL image of 10107-Bridge 4. 139
Figure B. 33: Panchromatic SEM-CL image of 10107-Tip bridge. 140
Figure B. 34: Panchromatic SEM-CL image of 10107-Bridge 5. 141
Figure B. 35: Panchromatic SEM-CL image of 10107-Bridge 8. 143
Figure B. 36: Panchromatic SEM-CL image of 10107-Bridge 9. 144
Figure B. 37: Panchromatic SEM-CL image of 10107-Bridge 10. 145
Figure B. 38: Panchromatic SEM-CL image of 10,107-Tip bridge 2. 146
Figure B. 39: Panchromatic SEM-CL image of 10107-Bridge 11. 148
Figure B. 40: Panchromatic SEM-CL image of 10106.85-Bridge 6. 150
Figure B. 41: Panchromatic SEM-CL image of 10106.85-Bridge 5. 152
Figure B. 42: Color SEM-CL image of 10106.85-Bridge 1 154
Figure B. 43: Panchromatic SEM-CL image of 10106.85- Bridge 4. 157
Figure B. 44: Panchromatic SEM-CL image of 10106.85'-Bridge 3. 158
Figure B. 45: Panchromatic SEM-CL image of 10106.85-Bridge 2. 160
Figure C. 1: Stages of SFOT-1-10106.85- bridge 6 reconstruction.....161
Figure C. 2: Change in increment thickness over time as recorded by crack-seal cement in the reconstructed bridge (SFOT1-10106.85-Bridge6). ..162
Figure C. 3: Comparison between cumulative displacement and linear elastic fracture mechanics models. 162

Chapter 1: Introduction

Fractures are widespread structures in the Earth's crust (National Research Council, 1996). The term fracture includes faults, opening-mode fractures, i.e. fractures with predominant opening displacement, and structures having various combinations of lateral and opening displacement (Pollard and Aydin, 1988; Schultz, 2000). The focus of my study is opening-mode fractures. Opening-mode fractures may be barren (joints) or partly to completely filled with mineral cement (veins). Partially to completely cemented opening-mode fractures and mechanisms of their formation are the topic of this thesis.

In hydrocarbon reservoirs, barren or partly cemented fractures tend to increase permeability, providing pathways for oil and gas migration, and enhancing flow of production fluid during recovery (Aydin, 2000; Philip et. al., 2005). Opening-mode fractures can significantly contribute to production in low permeability reservoirs that are otherwise uneconomic to produce (e.g., Pittman, 1979; Laubach, 2003). In unconventional reservoirs, even where sealed (mineral filled), opening-mode fractures that formed by natural geologic processes may interact mechanically and hydraulically with hydraulic fractures during well completion and potentially enhance production (Potluri et al., 2005; Gale et al., 2007).

Fractures in a diagenetically reactive environment such as hot, water-saturated subsurface rocks tend to accumulate cement deposits (Batzle and Simmons, 1977; Milodowski et. al., 1998; Hood et. al., 2003; Lander and Laubach, 2014). Sealed fractures are fractures in which cement deposits completely occlude fracture porosity (and thus probably render it an insignificant conduit for fluid flow). Open fractures are those that are barren of cement or partially cemented such that some porosity is preserved. Temperature, water chemistry, and host rock compositions and how these attributes vary

through time and fracture timing, opening rate and size are key to determining whether fractures are sealed or open (Laubach, 2003; Lander and Laubach, 2014).

Quartz crack-seal cement is precipitated when a fracture opens repeatedly over a long period of time, such that each time the fracture reopens a cement increment is deposited to fill the gap. The outcome of this process produces a quartz cement bridge that contains a detailed record of fracture opening at the location of the bridge (Laubach et al., 2004a; Becker et al., 2010). Characterizing the spatial and geometric attributes of fractures is vital for optimal hydrocarbons exploration and production (Stearns and Friedman, 1972; Nelson, 1985). Several methods are employed to infer and predict fracture distribution and geometry away from the well bore including using outcrop analogs (e.g. Hennings et al., 2000; Ortega and Marrett, 2000; Laubach and Diaz-Tushman, 2009), geostatistical models (e.g. Datta-Gupta et al., 1995; McLennan et al., 2009), and geomechanical models (e.g. Olson, 1993, 2004; Wilkins, 2007; Smart et al., 2009). Information about fracture growth history and mechanism can be very valuable in providing additional constraints on fracture sizes and geometry in geomechanical models; however, little has been done to address fracture growth in the subsurface from an observational standpoint.

In this study, I reconstructed the geometric evolution of opening-mode fractures—the width and height or length history--by mapping and palinspastically restoring crack-seal texture in partially cemented fractures sampled from a tight sandstone reservoir. In tight gas sandstones crack-seal texture is locally preserved in partly to largely open fractures within synkinematic quartz crack-seal cement bridges (Laubach, 1988; Laubach et al., 2004b). I used bridges near the tip and center of fractures to measure local widening histories and used the point measurements to infer the opening history of entire fractures. Geometric evolution of fractures is predicted by linear elastic

fracture mechanics and I compared model predictions against the structural record of fracture growth that I measured. I also systematically measured aperture along fracture traces to determine fractures shape and I compared them to fracture mechanics predictions.

Using textural imaging and analysis of crack-seal fracture cement of opening-mode fractures in the Cretaceous Travis Peak Formation of East Texas, I test kinematic models of fracture growth. A fracture may grow to a certain aperture, length and height then increase in aperture (width) incrementally over time without further increase in length and height (a circumstance I term a *stationary* fracture). Alternatively, a fracture may have contemporaneous aperture opening and increase in both length and height by tip propagation over a long period of time. In the first case, I expect the number of crack-seal increments to be nearly constant throughout the fracture with smaller increment thicknesses near the tips. In the latter case, I expect the number of increments to decrease toward the tips of the fracture. I also expect to have a variable increment thickness within each bridge. Other variations of these two models were also tested. This study is the first to attempt to reconstruct entire fracture growth in the subsurface for brittle sedimentary rocks using fracture mineralization textures.

In this thesis, chapter 2 provides a review on fracture growth mechanisms and explains the current understanding of fracture initiation and propagation from observational point of view as well as the mathematical framework of linear elastic fracture mechanics. Chapter 3 details the methods and procedures employed over the course of this study. Chapter 4 is a self-contained journal paper-styled chapter on fracture growth kinematics, to be submitted to the Journal of Structural Geology. Chapter 5 presents observations on fracture shape that will not be included in the journal article, and

discusses these observations in the context of linear elastic fracture mechanics. Finally, chapter 6 provides a summary of the main findings and conclusions.

TERMINOLOGY

Terms for brittle structures such as fractures, faults, joints, and veins are often used inconsistently in the published literature (Pollard and Aydin, 1988; Twiss and Moores, 1992; Gudmundsson, 2011). Fracture is a general term referring to any mechanical discontinuity along which rock or minerals broke creating two free surfaces across which the rock has lost cohesion (Twiss and Moores, 1992). The two surfaces are referred to as the fracture walls. The fracture surfaces meet at the fracture tips. Crack is synonymous with fracture but is a term usually used in the context of fracture mechanics (experimental or theoretical). Fractures are subdivided based on the orientation of the displacement vector relative to the fracture walls. Fractures with displacement vector perpendicular to the fracture walls are commonly referred to as extension or tensile fractures (Nur, 1981; Valerio et. al., 2000) (Figure 1.1A). I use the fracture mechanics term opening-mode (mode I) fracture. Fractures with displacement vector parallel to the fracture walls and with a discernible shear displacement are referred to as sheared fractures or faults (mode II) (Figure 1.1B). For tearing-mode fractures (mode III), the displacement vector is parallel to both the fracture walls and the edge of the fracture (Figure 1.1C). A mixed mode in which more than one type of displacement occurs is possible (e.g.: Hudson and Harrison, 1997).

Twiss and Moores (1992) define veins as extension fractures that are filled with mineral deposits. However, the term *vein* can be a confusing because it is also used to

refer to other features that are not opening-mode fractures like replacement bodies (e.g.: Mayor and Fisher, 1972) and dilatant faults (e.g.: Penczak and Mason, 1997). Joint is a general term referring to opening-mode fractures with little or no shear displacement (Pollard and Aydin, 1988).

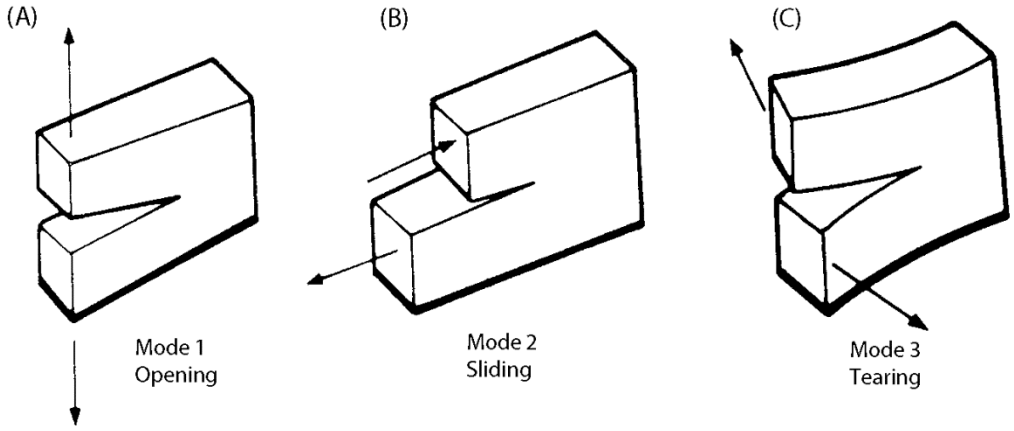

Figure 1.1: Fracture types based on the sense of displacement (modified from Rossmanith, 1983).

Chapter 2: Fracture Growth Processes

This chapter reviews previous work on fracture growth processes.

FRACTURE INITIATION AND PROPAGATION

Lab and Field Observations of Fracture Propagation

Fractures are generally considered to grow by nucleation from some pre-existing weakness (Engelder and Lacazette, 1990; Ykutake, 1992), propagation, and coalescence with neighboring fractures. Field evidence for propagation is provided by plumose structures and hackles on fracture surfaces that are consistent with fracture initiation from a point with subsequent growth by progressively propagating outward, but this evidence is almost exclusively from barren joints (Woodworth, 1896; Hodgson, 1961b; Hodgson, 1961a; Pollard and Aydin, 1988). The geometry of the fracture front as it propagates can be inferred by drawing curves perpendicular to the hackles of a plumose structure (Kulander et al., 1979; DeGraff and Aydin, 1987). Evidence of this type shows that some fractures initiate from planar bed boundaries and geometrically complex features such as trace fossils, bed forms, and dewatering structures (Hodgson, 1961b; McConaughy and Engelder, 2001). These observations are consistent with sedimentary features locally amplifying the remote stresses enough to initiate new fractures (Bahat and Engelder, 1984; McConaughy and Engelder, 2001). Triaxial rock deformation experiments also suggest that porosity and grain size are inversely related to the stress required for the onset of fracture initiation (Hatzor and Palchik, 1997). Bahat and Engelder (1984) postulated that fan-like plume structures on joint surfaces are the result of a cyclic process such as variation in pore pressure. Lacazette and Engelder (1992) attributed

fracture propagation in the Appalachian Basin to hydrocarbon charge and measured propagation episodes from plumose structures to be 0.6 - 1 m long intervals.

While natural fracture growth processes in the subsurface cannot be directly observed, Weinberger (1999) analyzed the initiation and growth of mud cracks in wet mud using the well-developed morphologies of exposed fracture surfaces. While prior studies found that fracture initiation in mud cracks can be initiated from the surfaces by defects such as air bubbles (Corte and Higashi, 1964), Weinberger (1999) found that, in the absence of such defects, fractures initiate from the bottom of the cracks at a layer boundary. This is consistent with observations of hackles on rock fractures in outcrop.

In layered rocks, a propagating fracture approaching a discontinuity such as a bedding plane may either (1) stop at the discontinuity, (2) cross the discontinuity and continue into the layer above, (3) deflect along the discontinuity in one direction, or (4) deflect along the discontinuity in two directions (T shaped intersection) (Hutchinson, 1996; Gudmundsson et al., 2002; Gudmundsson, 2011). Among the main reasons for vertical fracture arrest is abrupt change in Young's modulus, horizontal discontinuity, and the presence of a layer with unusually high fracture-perpendicular stresses (Gudmundsson and Brenner, 2001). Fractures in dissimilar layers were interpreted to have been arrested at the layers interfaces nevertheless they can communicate to form a composite fracture (Helgeson and Aydin, 1991; Gross and Eyal, 2007).

The direction of fracture propagation and displacement can change over time with changing remote stresses reactivating pre-existing fractures and producing new fracture sets with different orientations (Engelder and Geiser, 1980; Petit, 1995). The interaction between fracture sets with different orientations can be used to estimate the paleostress ratios (Dyer, 1988). Cross-cutting and abutting relationships between fracture sets can be used to determine the relative timing and sequence of structural events (Hancock, 1985;

Bergerat et al., 1992; Gross, 1993; Peacock, 2001; Bellahsen et al., 2006; Ellis et al., 2012).

Fracture Coalescence

In addition to fracture propagation, fracture linkage is a significant process of fracture growth. Shen et al. (1995) performed uniaxial tests on gypsum with two pre-existing fractures with different configuration and observed fractures coalescence in the laboratory. They found that pre-existing fractures can coalesce under uniaxial loading by shear or tensile failure. They also concluded that the coalescence mechanism depends on the relative position of the two fractures. Shear failure is observed when the two fractures are co-planer or slightly offset and a mixed shear/tensile mode of failure is observed when the fractures are overlapping in the loading direction. Another experimental study analyzed the behavior and sequence of three fractures coalescing under uniaxial compression in brittle sandstone using photographic techniques (Yang et al., 2012). Other studies on fracture coalescence in rocks and rock-like materials include rock deformation experiments (Einstein et al., 1969; Einstein and Hirschfeld, 1973; Chen et al., 1995; Wong and Chau, 1998), numerical simulations (Reyes and Einstein, 1991; Bobet and Einstein, 1998a; Bobet and Einstein, 1998b), and outcrop observations (Granier, 1985; Nicholson and Pollard, 1985).

According to these studies, linkage can occur in several ways. An isolated fracture may propagate toward a second stationary fracture. Depending on the stress boundary conditions, the propagating fracture curves toward the tip of the stationary fracture owing to the elastic stress perturbation caused by the presence of the two fracture tips, leading to fracture linkage (Figure 2.1). Fracture growth path is dependent on the stress state. Fractures that curve smoothly toward each other indicate isotropic remote stresses relative to the fracture induced stresses while fractures that has straight paths imply the

dominance of fracture-parallel differential compression over fracture induced stresses (Olson, 1993). Einstein and Stephansson (2000) provided a systematic analysis of possible coalescence paths with varying modes of failure under uniaxial and biaxial compression.

Fractures that are in the process of linking without being physically connected are said to be soft-linked. On the other hand, fractures that are physically connected are said to be hard-linked. Fracture linkage imposes a strong control on fracture aperture profile in compound fracture paths because the tips of previously isolated fractures produce local minima (Moros, 1999). In chapter 5 I demonstrate how tips of previously isolated fractures are preserved in such segmented compound fractures.

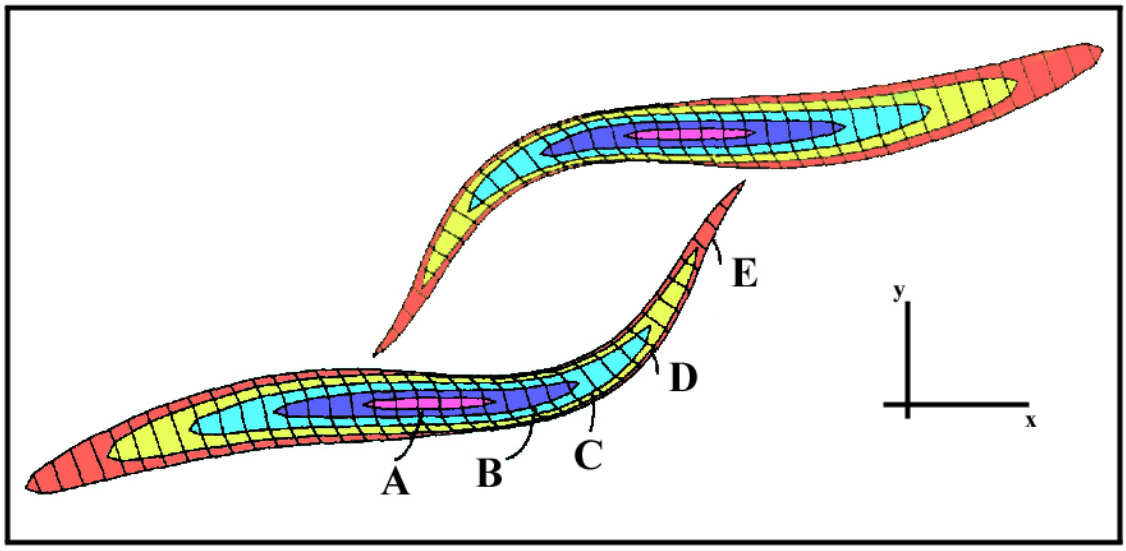

Figure 2.1: A model for fracture linkage evolution. Each letter and color represents a stage of fracture growth. Stage A the fracture tips are not affected by the adjacent fracture. The remaining stages the fracture tips increasingly curve toward the adjacent fracture before linkage occur (Modified from Olson and Pollard, 1991).

Crack-Seal Growth Mechanism

Crack-seal fracture cement was first described in veins in igneous and metamorphic rocks and epithermal deposits (Taber, 1916; Hulin, 1929; Batzle and Simmons, 1976; Knipe, 1977; Ramsay, 1980; Bons et al., 2012). Crack-seal fracture cement has been interpreted by these authors to reflect repeated opening and subsequent sealing of fractures along the host rock-fracture cement interface or within already precipitated fracture cement (Figure 2.2, Figure 2.3). Following cyclic events of fracture opening, cement precipitates from solution and seals the resulting gap.

Crack-seal cement can also form in partially and completely cemented fractures in sandstones (Laubach, 1988) and carbonates (Gaviglio, 1986; Srivastava and Engelder, 1990; Gale et al., 2010). In sandstone, crack-seal quartz cement precipitates in the form of isolated bridges (Laubach, 1988; Laubach et al. 2004a, b), separated by residual fracture porosity, preferentially on non-euhedral surfaces of quartz grains with favorable crystallographic orientation (Laubach, 2003; Lander and Laubach, 2014). According to these authors, quartz cement grows on quartz grains surfaces from both sides of the gap formed by fracture opening, meeting at a medial line (Figure 2.3-2). Euhedral quartz cement (blue in Figure 2.3-3) may grow onto existing crack-seal increment and on fracture walls not occupied by cement bridges (Figure 2.3-3). Subsequent fracture opening may split earlier crack-seal cement increments into two halves (Figure 2.3-4) resulting in complex crack-seal textures with small increment thicknesses (< 5μm) that make interpretation of the crack-seal cement record challenging. The opening histories of fractures, recorded by crack-seal bridges in five sandstones from different basins indicate that opening increment ranges between 1 μm and 1 mm with most of them under 5 μm (Laubach et al., 2004a).

Cervantes and Wiltschko (2010) compared tip-to-center cement textures in syntectonic veins in metamorphic rocks to determine the history of growth. They determined that veins grew in width and length by the addition of thin crack-seal veinlets (5-25 μm in kinematic aperture) within the boudin neck region of the veins.

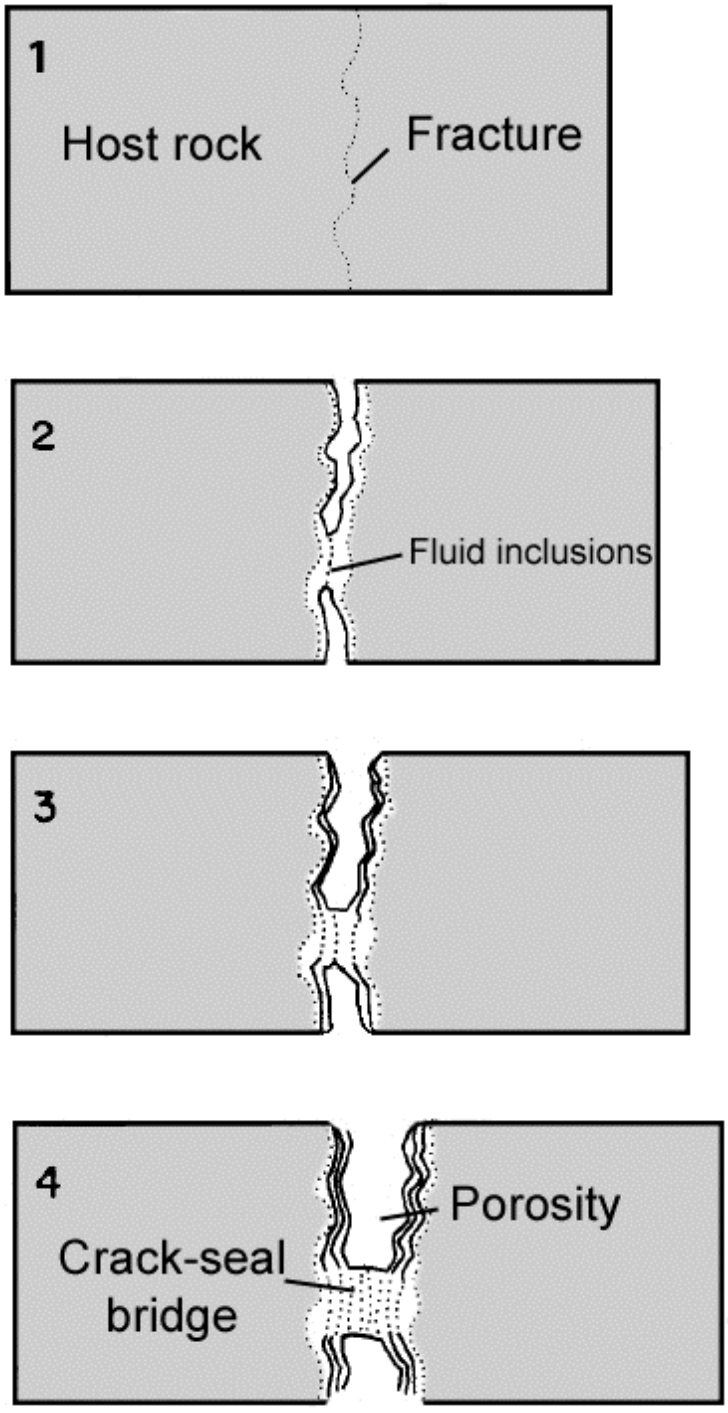

Figure 2.2: Model of crack-seal cement bridge evolution in sandstone. The shaded area represents the host rock and the white areas represent synkinematic quartz cement. Each dotted line represents a re-cracking event (modified from Laubach, 1988).

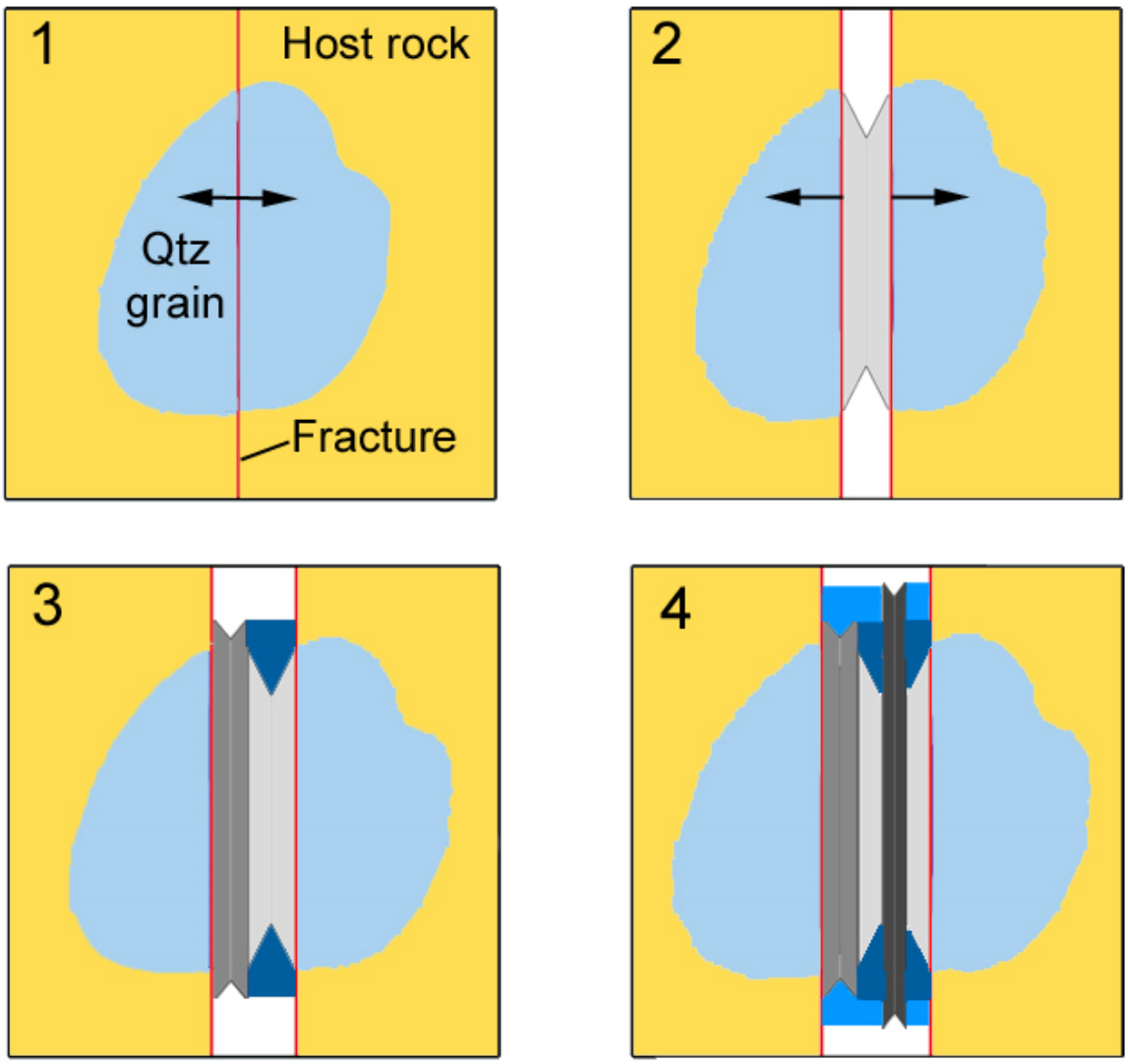

Figure 2.3: Model of crack-seal bridge evolution. Fracture walls are indicated by red lines and individual crack-seal increments in different shades of gray. (1) Arrows are displacement vectors. (2) A single crack-seal increment is produced, where the cement grew from both sides to meet at the middle of the gap. (3) A second increment is produced between the fracture wall and the first increment; euhedral quartz cement (dark blue) grew simultaneously. (4) A third increment is produced splitting the first increment in two halves; another phase of euhedral quartz cement (light blue) grew simultaneously.

Stresses and Fracture Initiation

Opening of a mode 1 fracture requires an effective tensile normal stress acting perpendicular to the fracture walls (Secor, 1965). In general, the Earth's crust at depth is under compressive total stress conditions (Zoback, 2010). While tensile total stress is locally possible in response to thermoelastic cooling, bending outside the neutral fiber of a fold, or around a cavity or pore, effective tension is generally considered necessary for propagation of opening-mode fractures (Engelder et al., 1993).

The least principal effective stress (σ_3') is equal to the total least principal stress (σ_3) minus the pore pressure (P_p). Mode 1 or opening-mode fractures are expected to form when the pore pressure exceeds the least principal stress (σ_3) resulting in tensile σ_3' (Secor, 1965; Secor, 1969; Hubbert, 1972). Opening-mode fractures propagate in the plane containing the maximum compressive principal stress (σ_1) and open in the direction of the least compressive principal stress σ_3.

High pore pressure can develop during sediment compaction while limiting the expulsion of pore fluids contained in the interstitial pore space, resulting in compaction disequilibrium. Another way to elevate the pore pressure is by topographic head gradients in confined aquifers, hydrocarbon generation, and by hydrocarbon accumulations in reservoirs (Spencer, 1987; Williamson and Smyth, 1992;Osborne and Swarbrick, 1997; Law and Spencer, 1998). High pore fluid pressure in combination with favorable stress state can produce extension fracture networks (e.g. Engelder and Oertel, 1985; Laubach, 1988; Lacazette and Engelder, 1992).

Fractures form in response to the local stress state which is a function of the remote and regional stresses, and; local stresses produced by material heterogeneities

and the fracture itself. The tractions acting on a fracture surface can be (effectively) tensile, shear, or a combination of both (Figure 2.4). Effective tensile loading is responsible for mode 1 fracture growth.

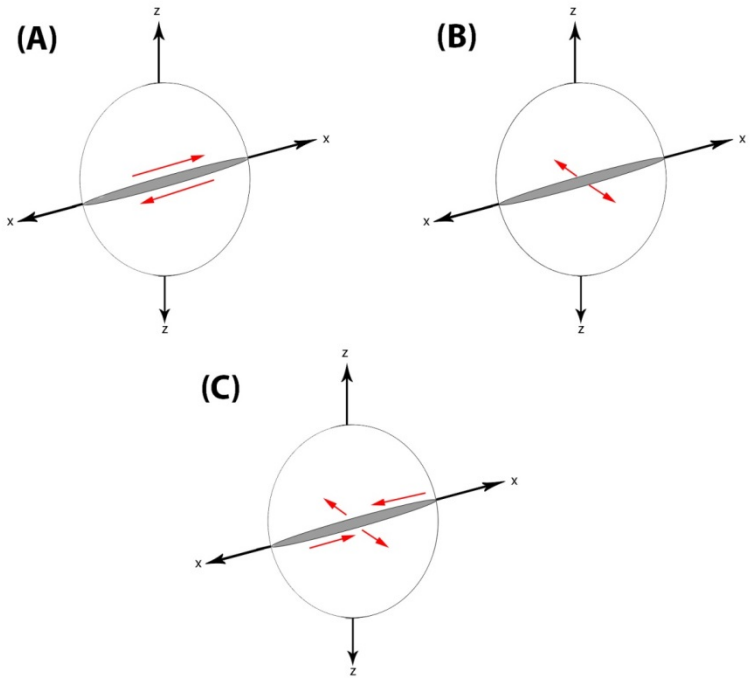

Figure 2.4: Types of penny-shaped fracture loading and displacement. (A) Tensile Loading in opening-mode displacement (B) Simple-shear loading in sliding/shearing-mode displacement (C) Mixed-mode loading in combination of sliding and opening-mode displacement (After Engelder et al., 1993).

Griffith Rupture Theory

Griffith (1921, 1924) presented a theory that is widely accepted today to be the foundation of fracture mechanics. He explained the difference between the observed and theoretical tensile strength of solids by postulating that all solids contain small flaws or microfractures. Due to the stress concentration at the tips of these flaws, the material fails at a stress lower than the macroscopic tensile strength of the intact material (Inglis, 1913). Griffith theory was initially proposed for in an infinitely thin plate (i.e. in 2D). However, later studies applied the theory to three dimensions and validated it experimentally in various materials including rocks (Sack, 1946; Robertson, 1955; Ode, 1956; Brace, 1960; Hoek and Bieniawski, 1965). In rock, grain boundaries, fossils, and bedding planes may serve as flaws or cracks for the nucleation of larger fractures (e.g. Engelder and Lacazette, 1990).

Fracture-Driving Stress

The magnitude of fracture-driving stress at the fracture tip can be quantified by the stress intensity factor K_i (i = I, II, or III- depending on the mode of displacement). In the subsurface, K_i at the tip depends on the fracture geometry, length (2c), stress which may be the remote minimum principal stress (σ_3), and pore pressure (P_p) (Lawn and Wilshaw, 1975; Engelder et al., 1993). In opening-mode fractures, K_I is given by

$$K_I = Y\,\sigma_3'\,\sqrt{\pi c} \qquad \text{(Eq. 2-1)}$$

where Y is a shape factor depending on the fracture geometry (penny-shaped: $Y = 2/\pi$; blade crack: Y = 1; edge crack: $Y = 2/\sqrt{\pi}$) and σ_3' is the minimum effective stress $\sigma_3' = \sigma_3 - P_p$. The parameter c is the half length of the fracture.

Critical fracture propagation occurs when $K_I = K_{Ic}$. where K_{Ic} is called the fracture toughness (Lawn and Wilshaw, 1975), a material property that describes the loading stress required for a fracture to propagate. Fracture toughness describes the continued growth of a pre-existing fracture or flaw (Engelder et al., 1993). Such flaws may include cleavage planes in crystals, grain boundaries, and pores. The application of fracture mechanics to rocks is most useful for fractures that are much larger than the size of single grains or pores.

Subcritical Fracture Growth

Fractures propagate critically if the stress concentration at the fracture tip exceeds the fracture toughness of the material. Under constant stress loading conditions, the critical fracture will propagate at a velocity approaching the sound velocity. However, under stress conditions below critical loading or $K_I < K_{Ic}$, fractures may propagate subcritically (Atkinson, 1982; Atkinson and Meredith, 1987). This may occur when chemical interaction between the pore fluids and the host rock weakens the bonds between molecules at the crack tips thus lowering the fracture resistance of the material and facilitating fracture growth. The most significant chemical process stimulating subcritical fracture growth in sandstone is the replacement of the strong silicon-oxygen bond in quartz with a weaker hydrogen bond (Martin, 1972; Scholz, 1972; Swain et al., 1973; Atkinson and Meredith, 1981; Atkinson, 1982). The phenomenon is termed stress corrosion. The chemical reaction for stress corrosion in a quartz-water system can be expressed as

$$(-Si - O - Si -) + H_2O \rightarrow (-Si - OH \cdot HO - Si-)$$

Subcritical crack growth is possible in areas undergoing relatively small but prolonged tectonic loading (Anderson and Grew, 1977; Atkinson, 1984; Kirby, 1984; Olson, 1993).

Subcritical fracture growth models suggest that the process can have a significant control on fracture spatial organization and network geometry (Olson, 2004).

Fracture Growth by Force of Crystallization

Experimental evidence suggests that crystal growth can exert pressure (Taber, 1916; Correns, 1949; Weyl, 1959). Force of crystallization in laboratory experiments produced a network of fractures in limestone and sandstone specimens immersed in sodium chloride saturated fluid under uniaxial loading (Noiriel et. al., 2010). Wiltschko and Morse (2001) suggested that banded fibrous veins, previously interpreted as crack-seal veins, are the product of pressure exerted by crystal growth aligned by a nonzero remote differential stress. However, Laubach et. al. (2004a) presented evidence against fracturing by force of crystallization. This includes sharply defined wall-rock fragments, fractured narrow cement bridges, and increased fracture porosity with increased fracture size.

FRACTURE GEOMETRY

Fracture size can be characterized by four elements: length, height, kinematic aperture (or opening displacement) and open aperture (Figure 2.5). Other parameters that control fracture geometry are fracture trace shape, segmentation, and aspect ratio. The fracture trace can be planar, curved, or sigmoidal. Fractures that are composed of several linked fractures with discernable distinct segments are visually segmented. The length of a fracture is the maximum horizontal distance measured between the fracture tips. The height of a fracture corresponds to the maximum vertical extent of the fracture relative to bedding. The kinematic aperture is the orthogonal distance between the fracture walls measured without regard to the presence of fracture mineral cement (Marrett et al., 1999).

The aspect ratio of a fracture is the ratio of kinematic aperture to the length or height of the fracture. Aspect ratio in combination with kinematic aperture can be used to estimate the fracture driving stress, accommodated strain, and fracture toughness (Delaney and Pollard, 1981; Gudmundsson, 1983; Segall and Pollard, 1983; Gross and Engelder, 1995). In practice, it is difficult to measure both true height and length without a 3D visualization of the fracture (e.g. CT scan). In outcrop, only a minimum length or height can generally be determined.

The fracture size attributes that are important for fluid flow are the components of size that have not been filled in with cement, the *open* length, width and height. Cement can systematically fill in fractures, reducing or eliminating *open* length, width and height as well as connectivity and consequently reducing fracture system porosity, permeability, and increasing rock strength (Olson et al., 2009).

Generally, fracture shape in the fracture mechanics literature is idealized to be penny-shaped or a blade-like (also called tunnel fracture) (e.g. Abé et al., 1976; Ho and Suo, 1993). In rocks, fracture shapes may be approximated to these idealized shapes for simplification. In a penny-shaped fracture, length is equal to its height and achieving this shape requires unrestricted fracture growth in all directions. In bedded rocks, fracture length parallel to bedding often exceeds fracture height perpendicular to bedding. This blade-like geometry is produced when height growth is limited by bedding-parallel mechanical layer boundaries while length growth is unconstrained (e.g. Corbett et al., 1987; Underwood et al., 2003). An edge fracture is another type of fracture that is often examined in the fracture mechanics literature (e.g. Gross et al., 1964; Cruse and

Vanburen, 1971). Such fractures occur at the physical boundary of the material or at the intersection with another discontinuity. Opening-mode fractures abruptly terminating against bedding planes, with maximum aperture against the interface, can be considered edge-fractures.

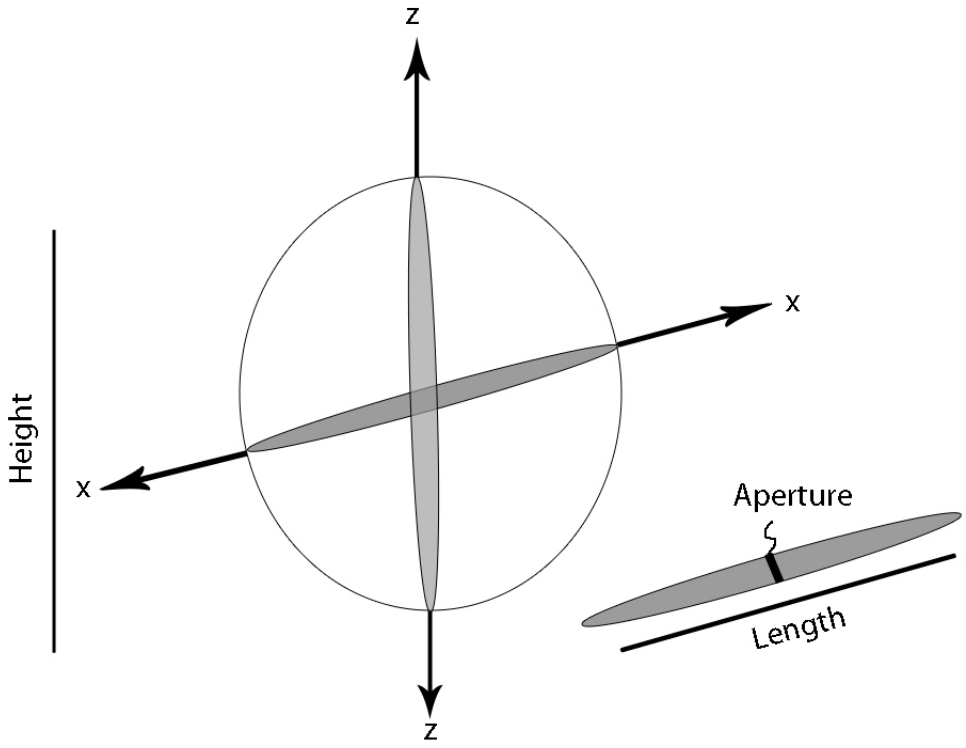

Figure 2.5: Penny-shaped fracture in 3D. The diagram defines variables needed to constrain the fracture geometry (After Engelder et al., 1993).

FRACTURE GROWTH MODELING

Several types of numerical approaches have been used to predict the shape and distribution of fractures in the subsurface and their growth over time. Such models are developed under certain boundary conditions determined by experimental data (e.g. Tang et al., 2013) or a mix of geomechanical data and diagenetic observations (e.g. Rijken et

al., 2002; Olson et al., 2009). In general, these models are built on the foundation of linear elastic fracture mechanics.

Linear Elastic Fracture Mechanics

Linear elastic fracture mechanics (LEFM) provides a mathematical framework to model and predict fracture initiation and propagation in elastic, isotropic, and homogeneous media. Since the focus of this study is on opening-mode fractures, LEFM concepts will only be discussed for the case of opening-mode fractures. Given elastic material properties such as the shear modulus G or Young's modulus E, Poisson's Ratio υ, and the crack-driving stress σ, the expected maximum displacement (ΔU^{max}) for a fracture can be calculated using the following equation:

$$\Delta U^{Max} = \frac{2(1-\nu)\Delta\sigma_I c}{\pi G} = \frac{4(1-\nu^2)\Delta\sigma_I c}{\pi E}$$

The displacement at any point x along the fracture can also be obtained by

$$\Delta U = \Delta U^{Max}\sqrt{1-\left(\frac{x}{c}\right)^2}$$

where x is the distance from the location of ΔU^{max} (i.e.: at x = 0 , $\Delta U = \Delta U^{max}$). For propagating fractures, c increases over time. For fractures that open without further propagation (stationary fracture), c is constant. These equations have been applied to describe the dilation of dikes (Delaney and Pollard, 1981; Pollard and Segall, 1987), but can also be applied to other types of opening-mode fractures such as partially cemented fractures in sandstone.

Observation-based Methods in Sandstone

Fluid Inclusion Thermometry Approach to Document Fracture Growth

Kaylor (2011) utilized fluid inclusion thermometry in crack-seal cement to infer the growth history of a single opening-mode fracture in the La Boca Formation, northeastern Mexico. The fracture was found to be the result of two isolated fractures coalescing to produce a larger fracture. The fracture was interpreted to initially have grown in length and aperture concurrently. A late phase of growth was interpreted to have growth in aperture with no further growth in length. Kaylor (2011) attributed the change in growth mechanism to a change in material response from increase in elastic compliance or increase in non-elastic flow properties.

Crack-seal Cement Texture Approach

Crack-seal increments represent periods of fracture opening. The relative age of increments can be established from cross-cutting relationship with lateral euhedral cement (Laubach et al., 2004a; Becker et al., 2010). Unraveling a fracture opening history is possible through careful analysis of crack-seal cement. I developed and utilized a method to reconstruct fracture growth based on textural observations of crack-seal fracture cement, further explained in chapter 3.

Chapter 3: Methods

This chapter describes methods and procedures including fracture sample collection, SEM sample preparation, and SEM-CL imaging. I also explain my methods for analyzing and quantifying crack-seal textures.

SELECTION CRITERIA AND SAMPLING PROCEDURES

Fracture selection criteria led me to work on fractures sampled from core (Table 3.1). Fractures suitable for this study had to meet the following requirements: (1) contain well developed quartz cement bridges (i.e. partially cemented fractures); (2) allow sampling of at least one fracture tip; (3) contain quartz cement bridges at the tip and in the fracture center to allow reconstruction of fracture opening history at least two locations along the fracture trace. The development of quartz cement bridges requires a minimum degree of diagenesis; quartz cementation in sandstone occurs in temperatures ranging between 60° and 145° C with rates of accumulation higher at higher temperatures (e.g. Burley et al., 1989; Bjorlykke and Egeberg, 1993; Walderhaug, 1994; Lander et al., 2008). In my effort to locate factures suitable for this study I focused on well-cemented sandstones including core from tight-gas sandstone reservoirs.

In searching for fractures suitable for this study there was no preference for outcrop versus subsurface fracture samples. Many disseminated fractures in sedimentary rocks are at high angles to bedding and near vertical in gently dipping beds (Hancock, 1985; Nelson, 1985). Therefore, cores from vertical wells may not encounter any fractures even when sampling a highly fractured reservoir. When fractures are encountered in core they usually sample only parts of the fractures, because they are often longer than the core diameter (diameter range: 1.75”-5.25”). In outcrops it is easier to sample fractures. Fractures in outcrops, however, may not have formed under the same

conditions as the ones that are present in the subsurface. Typical outcrops provide vertical exposure of rocks, such that only the height of fractures is well exposed. Bed parallel outcrops where fracture lengths can be observed are less common. In rare cases, both fracture length and height can be observed in outcrops, such outcrops would have staircase geometry.

Fracture Selection Criteria

For this study, initial fracture sample selection was made according to the following criteria:

1. Fractures are opening-mode with negligible or no shear component.
2. Fractures are macroscopic with measurable opening displacement.
3. Fractures are completely or partially filled with quartz cement. Fractures with visible quartz bridges were given priority in examination.
4. At least one fracture tip is present in the sample but samples with both tips were preferred because they allow determination of the center of the fracture.

Cores or outcrop samples were examined with a magnifying hand lens and a fluorescent flash light in search for fractures matching the selection criteria.

Thin sections for fractures of six formations that met these field criteria were prepared to determine the presence of crack-seal fracture cement textures suitable for this study (Table 3.1). I collected core samples of the Travis Peak and Cotton Valley Formations, East Texas, and outcrop samples from the Cambrian Eriboll and Proterozoic Applecross Formation (Torridonian) sandstones in Scotland during field work in summer 2013 specifically collected for this project. In addition, my advisor collected samples of Cambrian Tintic Quartzite from the Wasatch Range, the Proterozoic Hades Pass unit

from the Uinta Mountains, and from the Cretaceous Cardium Formation in Alberta, Canada. All formations contain partially cemented opening-mode fractures with fracture tips contained in hand samples. All samples were thin-sectioned and assessed petrographically for their suitability. The most suitable fractures for this study were found to be in core from the SFOT-1 well in the Travis Peak Formation, East Texas.

Formation	Location	Age	Well name	Fracture cement
Travis Peak Fm.	E. Texas	Cretaceous	S.F.O.T.#1	Crack-seal + Euhedral quartz
	E. Texas	Cretaceous	Mast A-1	Quartz lining (few bridges)
Cotton Valley Fm.	E. Texas	Jurassic	S.F.E. # 3	Crack-seal+ Euhedral quartz
Tintic Quartzite	Wasatch Mts., Utah	Cambrian	outcrop	Clay minerals
Hades Pass unit	Uinta Mts., Utah	Proterozoic	outcrop	No
Cardium Fm.	Alberta, Canada	Cretaceous	outcrop	Euhedral Quartz
	Alberta, Canada	Cretaceous	RAX OLSON	Euhedral quartz
Eriboll Group	NW Scotland	Cambrian	outcrop	Crack-seal quartz
Torridonian Group	NW Scotland	Proterozoic	outcrop	Crack-seal quartz

Table 3.1: List of examined samples.

Cutting Procedure

For all samples used in this study, I noted the sample and fracture orientation and position relative to bedding. For outcrop samples the attitudes of the fracture and bedding were recorded. For fractures observed in core, samples orthogonal and parallel to the core were taken to sample the length and height of the fracture. The samples were cut using a diamond blade rock saw. If the sample was fragile and the fracture was not well cemented, the risk of parting along the fracture while cutting the sample is high. In this

case, clear epoxy was applied on the fracture and left to cure overnight in a vacuum chamber prior to cutting the sample.

For fractures longer than the length of one standard thin section (24×46 mm), I followed the method of Gomez and Laubach (2006) for obtaining continuous thin sections without losing material between sections through that invariably occurs by cutting samples with the rock saw. The method overcomes that problem by making an incomplete cut (groove) through the sample with subsequent manual breaking along the incomplete cut (Figure 3.1).

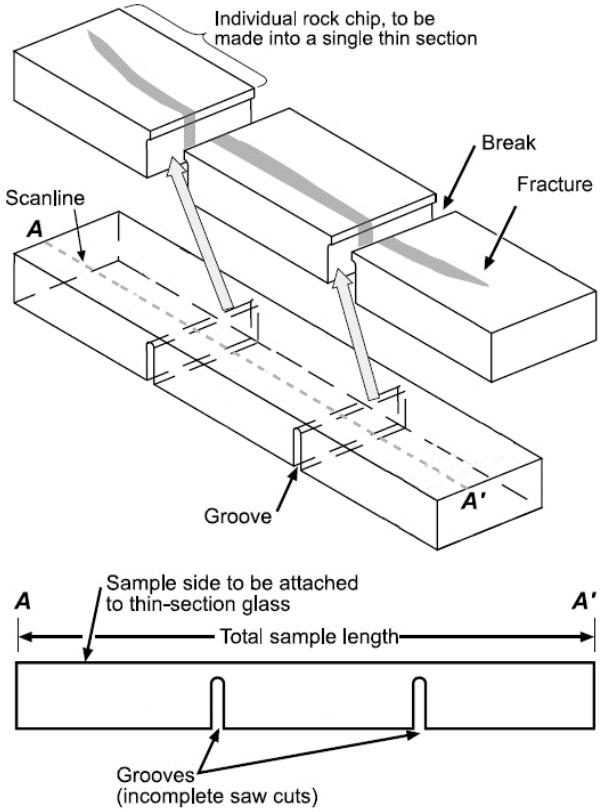

Figure 3.1: A diagram showing the method used for complete fracture preservation while cutting thin section chips (Modified from Gomez and Laubach, 2006).

Fracture Cement Petrography

Thin sections were examined under plane and cross polarized light microscope. Quartz cement bridges were identified petrographically looking for linear trails of fluid inclusions oriented parallel to the fracture wall characteristic of crack-seal cement bridges (Figure 3.2). The location of bridges potentially containing crack-seal textures were marked on a photomicrograph mosaic of the entire fracture for further investigation under scanning-electron microscopy (SEM) using a cathodoluminescence (CL) detector (SEM-CL).

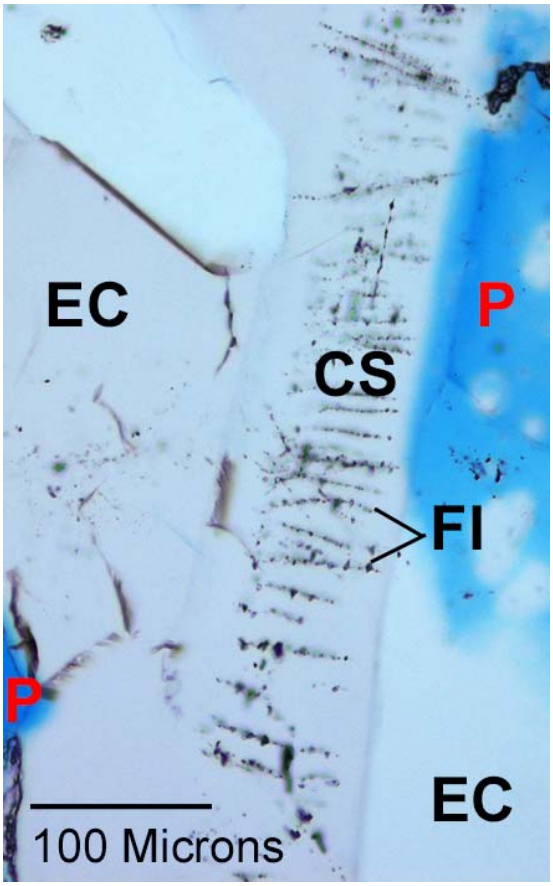

Figure 3.2: A plane-polarized photomicrograph of a quartz bridge with linear fluid inclusion trails indicating the presence of high quality crack-seal texture (Sample: SFOT-1-10,106.85'). Fracture walls are located just outside the top and bottom of the field of view.CS: crack-seal quartz cement; EC: euhedral quartz cement; FI: fluid inclusion trails; P: porosity.

SEM Sample Preparation Procedure

Cleaning

Cleaning thin-sections is an important part of sample preparation for SEM imaging. Any speck of dust or strand of fiber can reduce the quality of carbon coating and consequently affect the SEM image quality. The cleaning process includes removing any plastic label, removing adherent particles using the ultra-sonic cleaner, and finally clearing any dust using an air can. Thin sections are usually labeled with a plastic label glued on one of their ends by the vendor. Often, the label covers part of the rock sample. Using a razor blade and isopropyl alcohol the label is easily removed. Residual glue can be challenging to remove but applying the isopropyl and gently rubbing with extra-low lint rating laboratory wipes (e.g. KimWipes) can be effective. To label the thin section I etched the sample name and number on the back of thin sections with an etching pen. For the ultra-sonic cleaner, each thin section was placed in a small beaker at least half full with tap water. The ultra-sonic cleaner tub was also filled with water to the marked level. Thin sections were placed in the ultra-sonic cleaner between 3 and 5 minutes to delicately remove any adhering dust or other foreign particles from the thin section. After removing a thin section form the ultra-sonic cleaner, thin sections were cleaned with isopropyl alcohol and laboratory wipes. Immediately prior to applying the carbon coating, a few puffs of air from an air can were directed at each thin section for a final cleaning. Lab sample preparation procedures also avoid the use of luminescent diamond grit in sample polishing.

Carbon Coating

Nonconductive material tends to accumulate static charge on their surface under SEM which distorts the field of view (Leamy, 1982). Therefore, after cleaning thin

sections a very thin metallic coat was applied to make the surface of thin sections conductive allowing for electrical grounding. I utilized a vacuum evaporator to apply a very thin (20-30 nm) uniform graphite/carbon coat on thin sections. The vacuum evaporator runs electric current in a thin graphite rod that evaporates before being deposited as a thin uniform layer of graphite on the surface of thin sections. The coat is conductive but thin enough such that it will not interfere with imaging minerals and cements in the thin section.

Thin section mounting

A double sticky conductive sticker was used to mount the thin section on the specimen holder. I used carbon (conductive) paint to connect the surface of the thin section to the metallic holder. The carbon paint was left to dry under a heating lamp. Once the paint dries the thin section is ready for SEM imaging (Figure 3.3).

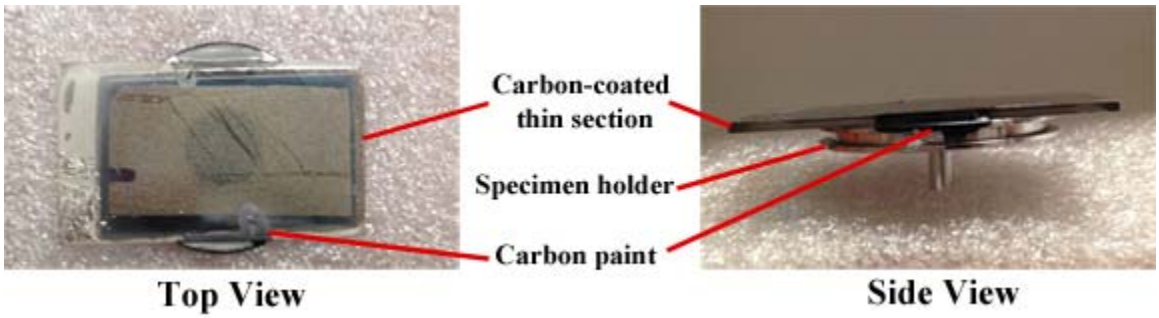

Figure 3.3: Top and side views of a mounted standard (24×46 mm) thin section ready for SEM imaging.

SEM- CATHODOLUMINESCENCE IMAGING

SEM-Cathodoluminescence imaging was performed on a Phillips XL30 SEM equipped with an Oxford Instruments MonoCL system (Figure 3.4). In geological applications, cathodoluminescence occurs when luminescent minerals are subjected to a

high energy beam of electrons (Miller, 1988; Boggs and Krinsley, 2006). Bombarding the minerals with electrons excites electrons in the host mineral which emit photons (visible and UV light) upon returning to their original state. SEM-CL imaging has many applications in sedimentary rocks. SEM-CL can reveal textures that are otherwise invisible such as mineral zoning, healed microfractures, crack-seal cement texture, shock lamellae, and original grain boundaries when overgrowth is present. The same mineral under SEM-CL could luminesce in different colors because of variation in some trace elements content (Landtwing and Pettke, 2005). Cathodoluminescence color of quartz grains can be used as a provenance tool (e.g. Zinkernagel, 1978; Matter and Ramseyer, 1985; Götze and Zimmerle, 2000; Walderhaug and Rykkje, 2000). In the scope of this study, SEM-CL was primarily used to view crack-seal cement, microfractures, and macrofractures boundaries. More information on the various applications of SEM-CL in sedimentary rocks can be found in Boggs and Krinsley (2006).

Figure 3.4: The scanning electron microscope system utilized in this study. The Oxford monoCL unit can be seen attached to the SEM chamber.

Instrument Settings

SEM-CL imaging is performed using the following instrument settings:

Voltage**:** 12-15 kV

Spot Size: 6.3

Filament Current: 28-50 μA

Magnification: 150X-1000X (mostly 500X)

CL PMT Voltage**:** 630

CL Color Filters: Mostly no filter (panchromatic), blue filter used sometimes to avoid streaking from highly luminescent carbonate cement.

Dwell Time**:** 400 µs

Imaging Procedure

Initially, I located the fracture of interest under secondary electron (SE) imaging before switching to CL imaging. The SE imaging minimum zoom on this instrument is around 22× which makes it easy to navigate through the thin-section to find the feature of interest. On the other hand, CL imaging minimum zoom is limited by the presence of the CL mirror to 150×, which makes it laborious to navigate to the desired feature.

To acquire high resolution CL images of quartz bridges I utilized automated SEM stage moving software (ISIS™). The software moves the SEM field of view systematically based on two points that I input prior to imaging. The number of images per mosaic is dependent on the size of the imaged area and the amount of magnification. The overlap between the mosaic images is ~ 15%, which was necessary to easily piece together the images of a bridge. I utilized Adobe Photoshop to optimize the brightness and contrast of the grayscale images prior to compiling them into one montage for each bridge.

Limitations

CL imaging using this particular SEM-CL system has some limitations. Each CL image takes 6 minutes to be acquired. A single bridge mosaic can take anywhere from 1 hour to 2.5 hours. Image resolution deteriorates for magnification greater than 500×. Acquiring images under greater magnification requires more images per mosaic and consequently more time without any noticeable improvement on the outcome. Another limitation to the system is that color CL images cannot be acquired on this CL detector in a single step. In order to acquire a color mosaic of a cement bridge, three grayscale images have to be acquired using blue, green, and red filters. The three images are then

assembled into an RGB image in Photoshop. Color CL images are visually more appealing, however, for the purpose of this study panchromatic and blue filter images were sufficient to view and analyze the crack-seal textures.

CRACK-SEAL MEASUREMENTS

For each crack-seal cement bridge that was imaged, I measured thicknesses of individual crack-seal increments and the kinematic aperture. Also, I calculated the average crack-seal increment thickness and estimated the number of fracture opening increments at each bridge.

Measuring a Single Crack-Seal Increment

I utilized a digital ruler calibrated to the SEM-CL image scale in a photo editing software (Adobe Photoshop™) to measure and record increment thicknesses. Increment thickness was measured perpendicular to the increment length to reflect the amount of displacement. The length of increments is mostly parallel to the fracture walls but in some instances some increments are oblique relative to the fracture walls. The thickness measurement angles relative to the width of the image were recorded.

Kinematic Aperture Measurement

Kinematic aperture is a measurement of displacement along an orthogonal line of observation relative to the fracture walls. The measurement includes fracture porosity and mineral fill but excludes any host rock grains or fragments that may have been dislodged within the fracture (Marrett et al., 1999). The kinematic aperture is an apparent aperture for fractures inclined to the image plane. However, sections were cut perpendicular to the fractures of interest thus assuring that the apparent aperture is close to the true kinematic aperture. Intergranular microfractures parallel to a larger “main” fracture and with the same sense of displacement were included in the kinematic aperture measurement of the

main fracture if the microfractures were observed within 200-300 μm distance from the main fracture walls (Figure 3.5). Intragranular microfracture apertures were excluded from kinematic aperture measurements because they may either be inherited from the source rock or formed in response to compaction (Laubach, 1997; Lander and Walderhaug, 1999). Kinematic aperture was measured at each observed crack-seal bridge and also at 200-500 μm spacing along selected fractures. Examples for fracture embedded grains, intergranular microfractures and intragranular microfractures can be found in Appendix B.

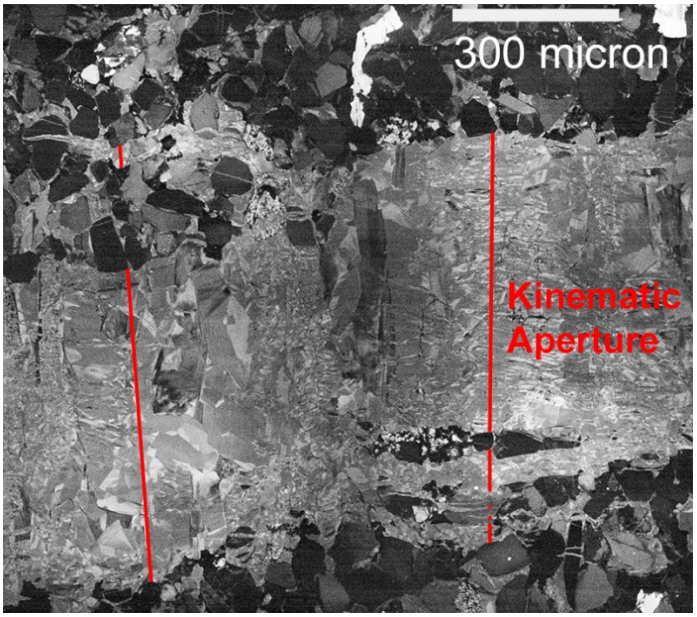

Figure 3.5: Blue filter SEM-CL image of SFOT-1-10107 Fracture. Kinematic aperture measurements at two locations are illustrated by the red lines.

Calculating the Number of Fracture Opening Increments

The number of fracture opening increments was calculated based on the measured fracture kinematic apertures divided by the thickness of clearly distinguishable opening increments. Counting the number of increments at each examined crack-seal bridge was

not a feasible option. Some increments are not well defined due to limited image resolution. In some instances crack-seal increments are not present across the entire length of the bridge because the thin section was not parallel to the bridge, thus intersecting only part of the bridge. Crack-seal bridges are commonly surrounded with layers of euhedral cement. Cutting a thin section oblique to the crack-seal increments might cause the bridge to deceptively appear to be partially crack-seal in the thin section (e.g. Figure 3.6).

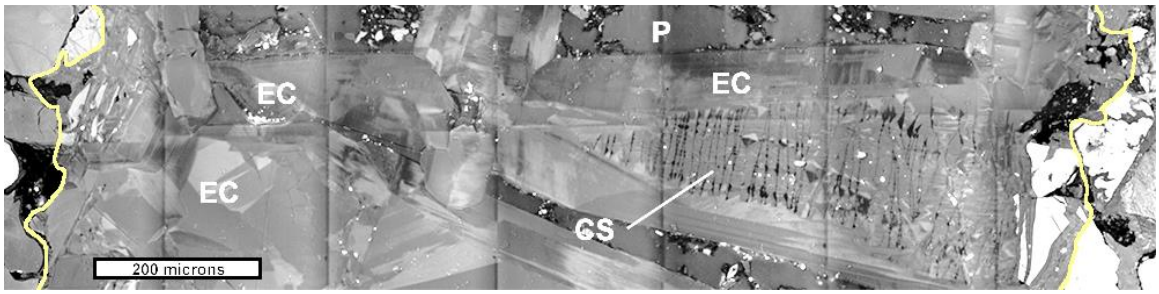

Figure 3.6: An example of an apparently partial crack-seal bridge (Sample: SFOT-1-10,108.3'). Fracture walls are marked by the yellow line. Crack-seal texture (CS) narrows toward the middle of the fracture before disappearing. Euhedral quartz cement (EC) surrounds the crack-seal and complete the bridge to the other fracture wall. This configuration is consistent of a thin section cutting a crack-seal bridge at an angle. Porosity (P) is present on both sides of the bridge.

Procedure for Increment Quantification

To estimate the number of fracture opening increments, I measured the thickness of as many crack-seal increments as possible with a minimum number of 10 measurements per bridge. The number of fracture opening increments was then calculated using

$$Number\ of\ opening\ increments = \frac{Kinematic\ Aperture}{Average\ Increment\ Thickness} \qquad \text{(Eq. 3-1)}$$

Method Validation

I tested the technique of estimating the number of fracture opening increments for two bridges containing continuous crack-seal textures across the entire width of the fracture, and with well imaged and defined increments. For the first bridge, the predicted number of opening increments using equation 3-1 and an average increment thickness determined for 30 crack seal increments was 70 increments, compared to 69 counted increments. For the second bridge the estimated number of opening increments was 86 while the counted number of increments was 80. From these results I concluded that my method for estimating the number of opening increments is valid given that enough and representative increment thickness measurements are taken.

Estimating Error

The standard error in average increment thickness error was calculated using the following equation:

$$Standard\ Error = \frac{Standard\ Deviation}{\sqrt{Number\ of\ measurements}} \qquad \text{(Eq. 3-2)}$$

The digital measuring tool can introduce small error into thickness measurements (~ 1 micron). This is inherent to the image resolution and not included in the standard error quantification but it is important to consider that 1-2 micrometer difference between two measurements is not significant.

QUARTZ BRIDGE RESTORATION

Bridge reconstruction provides a relative chronological record of fracture opening history at the bridge location. Since fracture re-cracking can occur anywhere within existing cement bridges during repeated crack-seal events, a young crack-seal increment can split an older one into two halves (e.g. Figure 3.8). Without palinspastic reconstruction of the bridge, differentiating between half-increments and full increments

can be difficult, especially when half-increments are separated by multiple younger increments. Therefore, proper bridge restoration will lead to accurate count of the number of increments. The method I utilized for bridge restoration is based on previous studies (Laubach et al., 2004a; Becker et al., 2010). The cross-cutting relationship between the crack-seal cement and the euhedral lateral cement is used to determine the relative time of each increment. Increments that encroach more into the lateral cement is typically younger (Figure 3.7). Also, cross-cutting relationship among crack-seal increments can be used to determine relative time. In Figure 3.8, the younger yellow increment cuts the pre-existing purple increment.

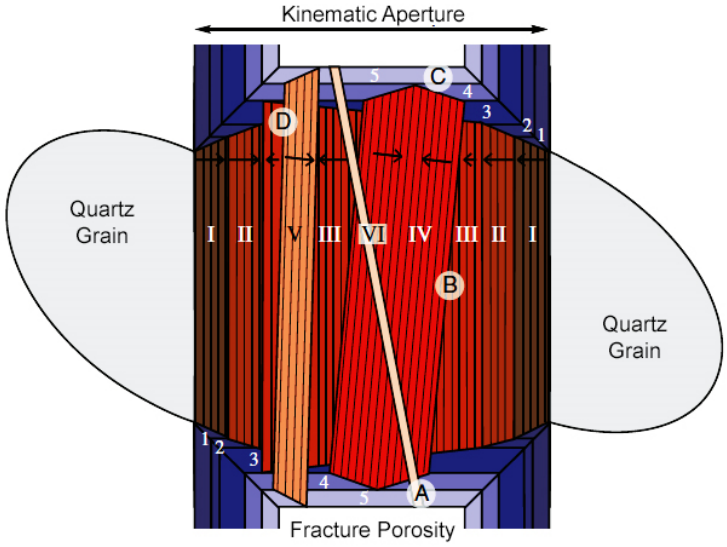

Figure 3.7: A schematic of a crack-seal bridge evolution showing the method of interpreting crack-seal relative age (Roman numerals) using cross-cutting relationship with lateral euhedral cement (Arabic numerals) (After Becker et al., 2010).

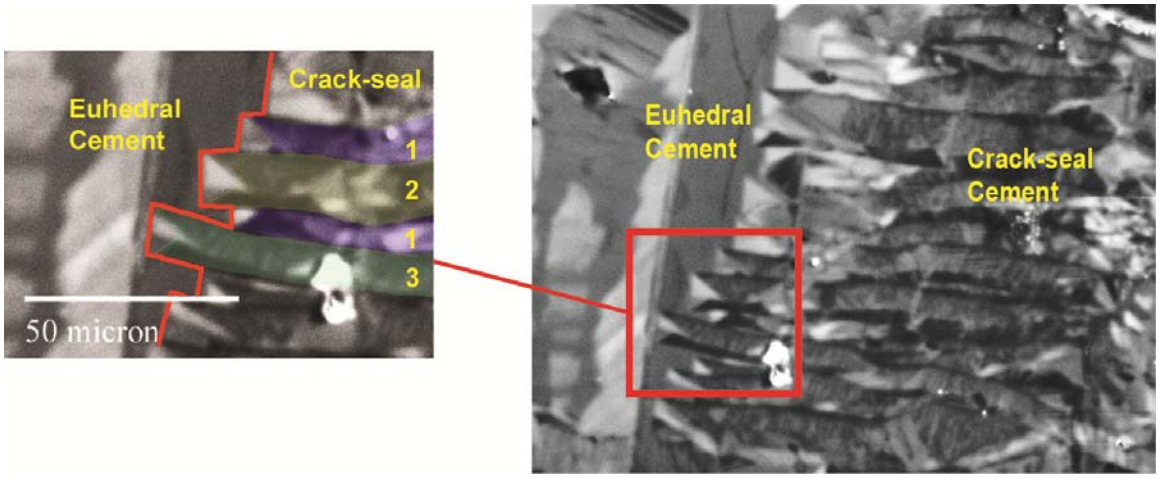

Figure 3.8: **Right:** a panchromatic image of a quartz crack-seal bridge with bordering lateral euhedral quartz cement (sample: SFOT-1-10108.3'). **Left**: interpretation of crack-seal increments relative time from encroachment into the euhedral cement. Increments are numbered from oldest to youngest.

Uncertainty and Error

Similar to geologic mapping, reconstruction of a cement bridge is an interpretation, especially determining relative time of neighboring crack-seal increments with little differences in the amount of encroachment into the euhedral cement. Since relative timing can be difficult to discern for adjacent crack-seal increments, groups of roughly contemporaneous increments were lumped into larger bridge growth segments.

Comparison to Linear Elastic Fracture Mechanics Predictions

Two linear elastic fracture mechanics models were created for each reconstructed bridge. The modeling is used to test whether the fracture is following linear elastic fracture mechanics expectations of a propagating fracture or a stationary fracture with concurrent aperture opening.

Procedure for LEFM Predictions

For both models I utilized the following equations with the assumption of a penny-shaped fracture following an elliptical function:

$$\Delta U_{max} = \frac{2(1-\upsilon)\Delta\sigma_I c}{\pi G} = \frac{4(1-\nu^2)\Delta\sigma_I c}{\pi E} \quad \text{(Eq. 3-3, Gudmundsson, 2011)}$$

$$\Delta\sigma_I = \frac{K_{Ic}}{Y\sqrt{\pi c}} \quad \text{(Eq. 3-4, Lawn and Wilshaw, 1975)}$$

$$\Delta U_{@x} = \Delta U_{max}\sqrt{1-\left(\frac{x}{c}\right)^2} \quad \text{(Eq. 3-5, Engelder et al., 1993)}$$

Where ΔU_{max} is equal to the expected maximum kinematic aperture (double crack wall displacement), υ is Poisson's ratio, $\Delta\sigma_I$ is the mode 1 crack-driving stress, c is equal to the crack half length, G is the shear modulus, E is Young's modulus, $\Delta U_{@x}$ is the expected kinematic aperture at any location x along the crack, with x the distance measured away from the point of maximum displacement (i.e. the center of the crack).

Model Parameters

For the propagating fracture model the crack length c was increased with each time step and all other parameters were kept constant. Conversely, the stationary fracture model all parameters are constant while increasing the crack-driving stress $\Delta\sigma_I$ with each time step.

For Poisson's ratio (υ) and Young's modulus I used measured values of samples with similar lithology from the same core of the Travis Peak Formation (Jizba, 1991). These values were significantly lowered for the stationary fracture model to produce aperture comparable to the observation. Similar values were also used for a propagating fracture model for comparison. For fracture toughness (K_{Ic}) a typical value for sandstones was used. The half-length of the fracture (c) was determined from observation of the

examined fracture. The shape factor (Y) is $2/\pi$ (penny-shaped). The following tables list the values of the models and their parameters:

1- Propagating Fracture Model:

c	0-0.0416 m	E*	40000 MPa
υ*	0.18	K_{Ic}	1.5 MPa/$\sqrt{m}$

2- Propagating Fracture Model (More compliant E):

c	0-0.0416 m	E	470 MPa
υ*	0.18	K_{Ic}	1.5 MPa/$\sqrt{m}$

3- Stationary Fracture Model

c	0.0416 m	E*	40000 MPa
υ*	0.18	K_{Ic}	1.5 MPa/$\sqrt{m}$

4- Stationary Fracture Model (More compliant E):

c	0.0416 m	E	470 MPa
υ*	0.18	K_{Ic}	1.5 MPa/$\sqrt{m}$

*Denotes data from Jizba (1991).

Chapter 4: Growth Kinematics of Opening-Mode Fractures in the Cretaceous Travis Peak Formation, East Texas

INTRODUCTION

Fractures and fracture networks control fluid flow and mass and heat transfer in the upper crust, and significantly govern its mechanical properties (National Research Council, 1996). Fracture size—the lengths, heights, and apertures of fractures and the connectivity of fracture networks—plays a central role in governing how fractures affect fluid flow and rock strength (Long and Witherspoon, 1985; Philip et al., 2005). Size attributes depend on growth history. The processes associated with nucleation and propagation of single fractures, and their coalescence into fracture networks have been observed in laboratory rock mechanics tests and described with fracture mechanics models that replicate reasonably well the end products of fracture growth as observed in fracture arrays in outcrop; thus fracture nucleation and growth have been considered reasonably well understood (Price, 1966; Segall, 1984; Engelder, 1985; Gudmundsson, 1987; Pollard and Aydin, 1988; Olson, 1993; Shen et al., 1995; National Research Council, 1996; Bobet and Einstein, 1998; Paterson and Wong, 2005; Anders et al., 2014). Formation of opening-mode fractures is understood to involve nucleation from grain- and pore-sized flaws or microfractures, fracture length and height growth is by propagation and concurrent aperture widening, and propagation of length and height involves the coalescence of single fractures into segmented fractures and linked fracture systems (Brace and Bombolakis, 1963; Olson, 1993; Flodin and Aydin, 2004; Engelder, 2007).

Testing this laboratory and model-based consensus about fracture growth is, however, limited by what can be deduced about the growth history of natural examples. For example, hackle and plumose structures on fracture surfaces are evidence for

episodic propagation and arrest (Woodworth, 1896; Bahat and Engelder, 1984; Kulander and Dean, 1985; Pollard and Aydin, 1988; Lacazette and Engelder, 1992; Engelder, 2007) but provide no evidence of how or if width changes during the lengthening process. Likewise, field observations of systematically curving traces of fractures in proximity are consistent with fracture propagation observed experimentally in elastic media (Pollard et al., 1982; Pollard and Segall, 1987; Dyer, 1988; Cooke and Pollard, 1996) but these field relations provide only glimpses of end products.

The mathematical framework of linear elastic fracture mechanics (LEFM) is effective at simulating fracture shape evolution, interaction of closely spaced fractures, and the evolution of fracture networks (e.g. Hoek and Bieniawski, 1965; Atkinson, 1987; Delaney and Pollard, 1981; Engelder et al., 1993; Renshaw and Pollard, 1995; Olson, 2004; Olson et al., 2009). However, some assumptions of LEFM as currently applied have not been tested. These include that critically propagating fractures widen with increasing fracture length, which is implicit to LEFM for simple fracture geometries and thus to most currently existing mechanics-based approaches to simulating fracture network evolution.

Recent work (e.g. Laubach et. al., 2004b; Becker et. al., 2010; Laubach et. al., 2014) on isolated quartz cement deposits in some otherwise open fractures provides a way to test the consensus about fracture growth and the application of LEFM by allowing reconstruction of the growth history of natural fractures. In sandstone that has experienced burial temperatures in excess of ~80°C, crack-seal quartz cement in partially cemented fractures forms isolated cement bridges that connect both fracture walls surrounded by residual fracture porosity (Laubach, 1988; Laubach, 2003; Lander and Laubach, 2014). Crack-seal texture forms by repeated episodes or stages of fracture

opening and subsequent fracture cementation resulting in banded cement textures (Taber, 1916; Hulin, 1929; Ramsey, 1980). Microthermometric and Raman microprobe studies of fluid-inclusion trapped during crack-seal cement growth show that crack-seal bridges track fracture opening over millions to tens of millions of years (Becker et al., 2010; Fall et al., 2012, 2014). Such fluid inclusion studies also allow for the reconstruction of pore fluid chemical, temperature, and pressure conditions during fracture opening (Parris et al., 2003; Hanks et al., 2006; Becker et al., 2010; Van Noten et al., 2011; Duncan et al., 2012; Fall et al., 2012, 2014).

In this study, I documented the widening and lengthening history of opening-mode fractures by measuring the fracture opening displacement recorded in crack-seal fracture cement. Crack-seal cement is broadly contemporaneous with or synkinematic relative to the fracture opening. The textural and compositional record contained in crack-seal cement thus represents a record of fracture opening kinematics (Durney and Ramsey, 1973; Cox and Etheridge, 1983; Cox, 1987; Urai et al., 1991; Hilgers and Urai, 2002; Laubach et al., 2004a,b; Renard et al., 2005; Bons et al., 2012). In quartz, crack-seal textures are best observed in scanning electron microscope-cathodoluminescence (SEM-CL), with individual crack-seal cement increments highlighted by variations in CL intensity and color (Dietrich and Grant, 1985; Laubach et al., 2004b). Analysis of cement deposit textures allows reconstruction of sequential fracture history (e.g., Lee and Wiltschko, 2000) including fracture widening (Becker et al., 2010) and lengthening (Cervantes and Wiltschko, 2010).

My results document fracture widening with limited lengthening. I use LEFM concepts to compare two processes by which fractures widen in aperture without concurrent propagation: (1) Fractures could widen in aperture without concurrent growth

in length or height if fractures experience an increase in loading stress without exceeding the threshold stress for critical propagation. (2) Under constant loading conditions, fracture aperture could widen without concurrent propagation if the host rock becomes more compliant or deforms by non-elastic deformation processes after initial propagation. Non-elastic deformation could be accommodated by chemical dissolution-precipitation reactions in the host rock (Eichhubl and Aydin, 2003; Eichhubl, 2004). To my knowledge, such processes have not been systematically investigated for brittle fractures.

GEOLOGIC BACKGROUND

Fractures analyzed in this study were collected from core of the Ashland Exploration, S. F. O. T. No. 1 well, Nacogdoches, N. W. Field, Nacogdoches County, Texas (Figure 4.1). This well was drilled as part of the Gas Research Institute extensive tight gas drilling program in the 1980's (Laubach, 1989). The well is located in the East Texas Basin, which is characterized by subsidence, very low strain Gulfward extension on small normal faults, and local salt diapirism (Jackson and Seni, 1983). The well is located in gently dipping strata, distant from normal faults with small displacement, and open folds. The well is located on the SW flank of the Sabine Arch, a low amplitude north trending anticline formed by two episodes of uplift (Figure 4.1) (Laubach and Jackson, 1990).

Fractures for this study were collected from the Lower Cretaceous Travis Peak Formation, a gas producing unit consisting of mainly quartzarenite and subarkose interbedded with mudstone (Dutton and Land, 1988). Significant porosity and permeability loss is caused by pervasive quartz cementation, resulting in average porosity of 8.8% and core plug permeability of less than 0.1 mD (Holditch et al., 1985; Dutton, 1986; Dutton and Land, 1988). Quartz cementation was noted to increase with increasing

present-day depth (Dutton and Diggs, 1990; Soeder and Chowdiah, 1990). Quartz cement gradually increases with burial depth within the Travis Peak and ranges from 16% at the top of the formation to 19% at the bottom (Dutton and Diggs, 1990).

The sand-rich intervals of the Travis Peak Formation contain cemented and partially cemented vertical opening-mode fractures striking east-northeast (Laubach, 1988). Fracture mineralization is dominated by crack-seal and euhedral quartz with small amounts of late ankerite and clay. There are two fracture shapes in the Travis Peak with similar types of cement and orientation; one is tall and thin and the other is short and wide (Laubach, 1989). Fractures with apertures > 0.1 mm tend to be only partially mineralized with remaining porosity between quartz cement bridges (Laubach, 2003). Fluid inclusion microthermometry correlated to a burial curve for the Travis Peak Formation at the nearby SFE2 well (Figure 4.1) suggested that fractures initiated near maximum burial depth around 48 Ma and continued to grow to present day (Becker et al., 2010). The maximum burial depth of the Travis Peak at the S.F.O.T. 1 well was 3.2 km corresponding to a maximum temperature of 145° C at the top of the formation. Currently, the top of the Travis Peak Formation is at a depth of 2.7 km (8,957 ft) (CER, 1985). The fractures in this study come from a depth of approximately 3 km (~10,100 ft).

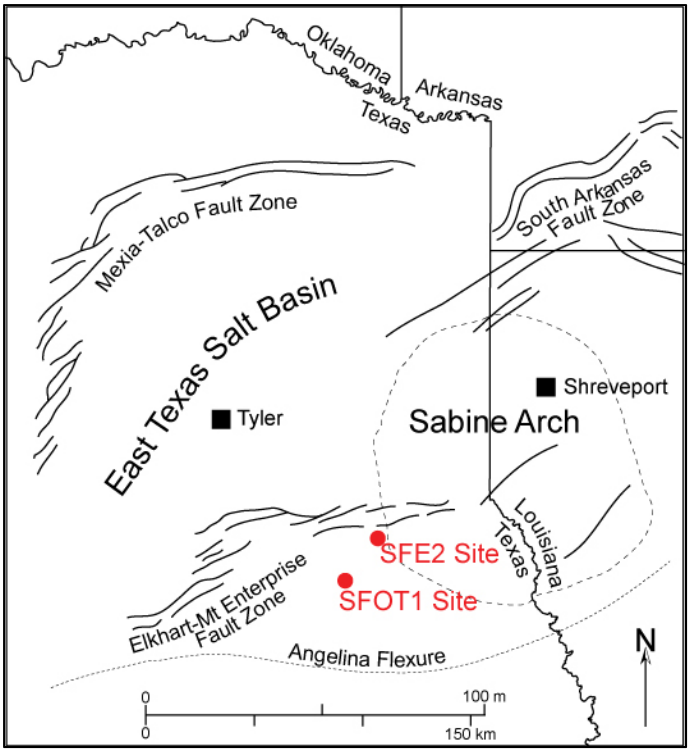

Figure 4.1: Location of the SFOT-1 and SFE-2 wells located southwest of the Sabine Arch in east Texas.

METHODS

To allow a comparison between textures in quartz deposits (bridges) near the center of fractures and near the tip, I collected 7 samples of fractures with preserved fracture tips of which 3 were used in this study. I sampled only fractures that were observed under a binocular microscope to be partially or completely filled with quartz cement thus avoiding barren fractures formed during core extraction and handling. Because most fractures observed in this core have lengths greater than the 4-inch (10 cm) core diameter, all fractures sampled for this study contained only one tip in the plan-view dimension of these mostly steeply dipping fractures. Thus, the total length and height of these fractures is not known (e.g.: Figure 4.2A). Crack-seal bridges were initially

identified in transmitted light microscopy by their characteristic fluid inclusion trails aligned parallel to crack-seal texture (which itself is not visible in transmitted light)(Figure 4.2B). Bridge crack-seal textures were imaged using a Phillips XL30 SEM equipped with an Oxford Instruments MonoCL system operated at 15 kV. Panchromatic CL images were obtained for each bridge by taking several images at 500×+ magnification with no color filter at 400 microsecond dwell time following techniques described by Milliken and Laubach (2000) and Reed and Milliken (2003). Grayscale photo mosaics for each bridge were created using Adobe Photoshop (Figure 4.2C). Images were digitally sharpened and corrected for optimal contrast and exposure.

Key textural elements measured in each bridge are illustrated in figure 4.3 and described later in the text. For each imaged bridge, I measured the thickness of 10 -80 crack-seal increments using a digital ruler calibrated to the SEM image scale. I also measured the kinematic aperture, i.e. the distance from fracture wall to wall independent of mineral fill orthogonal to the fracture trace, at the location of each bridge. The number of fracture opening increments at each bridge location was estimated by dividing the kinematic aperture by the average increment thickness.

A direct count of crack-seal cement increments would tend to provide an inaccurate count of the number and width of fracture opening increments for two reasons: (1) the crack-seal texture of some bridges is only incompletely imaged if the thin section is cut oblique to the long axis of the bridge. In these cases, the imaged crack-seal count underestimates the total number of crack-seal opening increments across the width of the fracture. (2) Continuous crack-seal processes tend to break earlier-formed crack-seal cement reducing the apparent size but increasing the apparent number of increments. Thus, younger crack-seal increments generally split earlier increments into what appears

to be two or more increments. Without accounting for split increments, a direct count of crack-seal cement layers would overestimate the number of fracture opening increments. The number of fracture opening increments at each bridge location was thus estimated by dividing the mechanical aperture by the average size of complete crack-seal increments.

In addition, two bridges located near the center of a fracture and providing a complete crack-seal cement record over the entire aperture of the fracture were reconstructed using palinspastic restoration that utilizes cross-cutting and overlapping relationships between crack-seal cement and bordering lateral euhedral cement to determine the relative sequence of crack-seal cement deposits (Figure 4.2). Bridge reconstruction followed geometric criteria described by Laubach et al. (2004a) and Becker et al. (2010). In this reconstruction, I attempted to identify and account for split cement increments. Because relative timing difference is difficult to discern for adjacent crack-seal increments, groups of roughly contemporaneous increments were lumped into larger bridge growth segments (Figure 4.2). More details on the mapping of cement bridges are provided in Appendix A. Thickness of all increments in the reconstructed bridges were measured and counted and compared to the calculated number of fracture opening increments based on the average increment thickness.

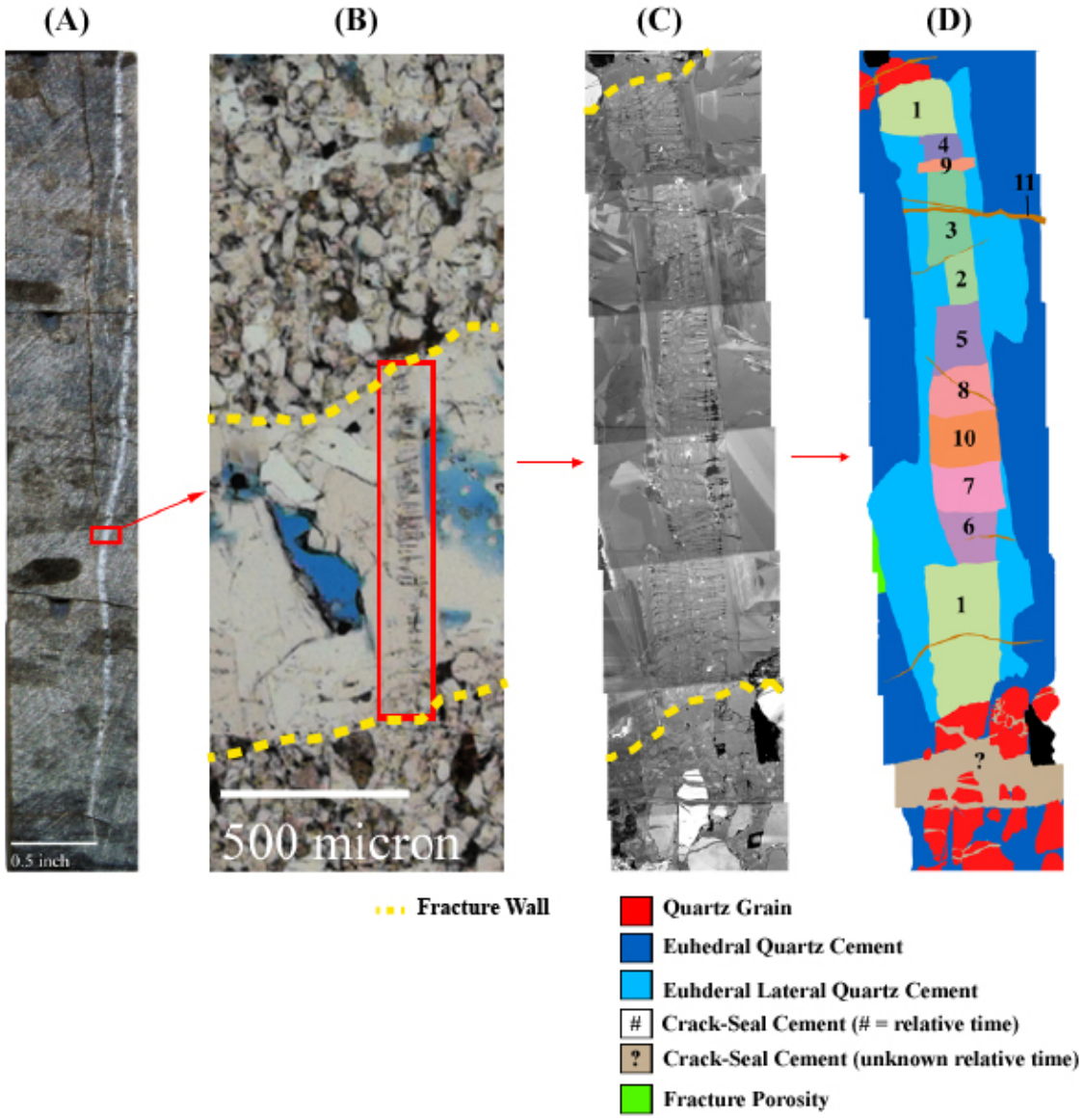

Figure 4.2: (A) Core image of SFOT-1 well, depth of 10,107', Travis Peak Formation. (B) Transmitted light photomicrographs of partially cemented fracture. Quartz fracture cement bridge indicated with red rectangle. Blue: residual fracture porosity filled with epoxy. (C) SEM-cathodoluminescence image of quartz cement bridge outlined in B. (D) Interpreted map of the quartz bridge indicating stages of bridge cement growth, numbered from oldest (1) to youngest (11).

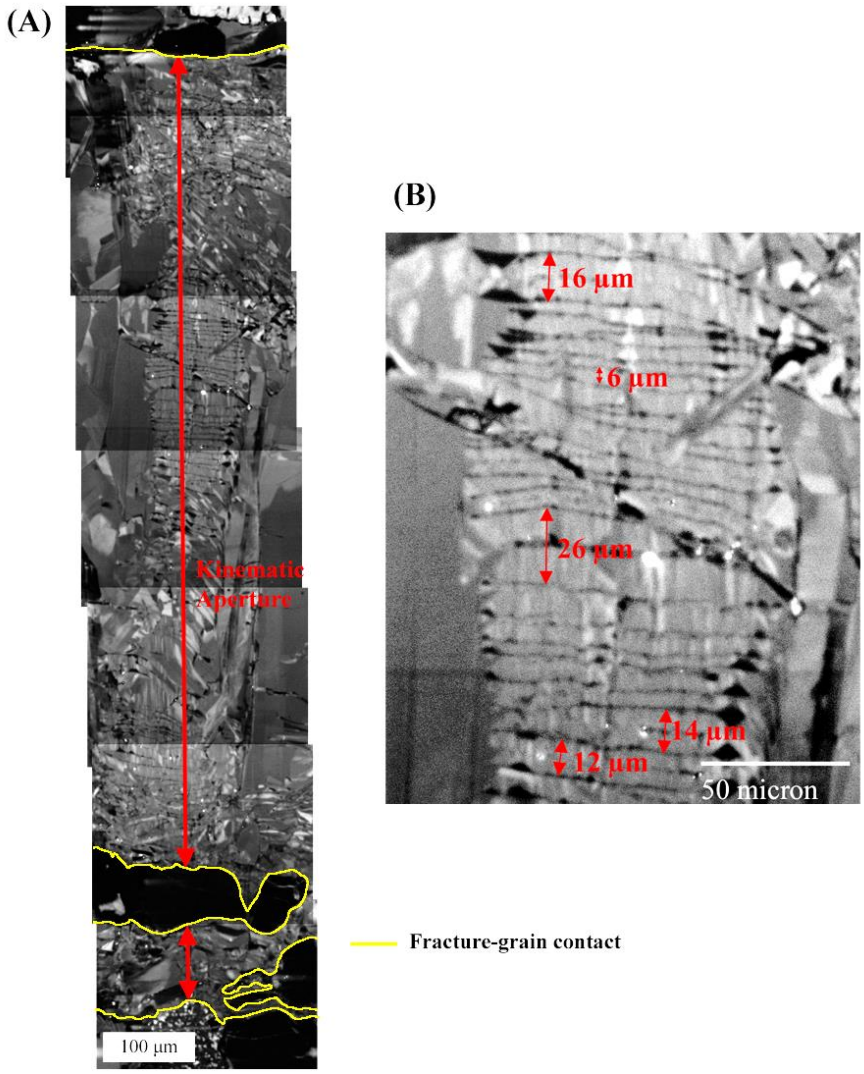

Figure 4.3: Examples of increment thickness and kinematic aperture measurements on SEM-CL image of a crack-seal bridge (Sample: SFOT-1-10,108.3 ft). (A) Kinematic aperture is the sum of distances indicated by the red arrows. (B) A close-up of the same bridge with examples of thickness measurements of complete crack-seal increments.

RESULTS

Of seven fracture samples collected, three partially cemented vertical fractures of Travis Peak Formation the SFOT-1 core were found to contain bridges suitable for

fracture growth analysis. Two of these three fractures are closely-spaced en-echelon fractures sampled for thin sections along their length or horizontal extent (perpendicular to the vertical core axis and parallel to bedding); one fracture was sampled along its height or vertical extent (parallel to core axis and perpendicular to bedding). For these three fractures, I imaged 38 crack-seal cement bridges and calculated the number of fracture opening increments based on the kinematic aperture and average crack-seal cement increment thickness. Bridges were selected to sample the fractures along transects from the fracture tips to a position approximately in the center of the fractures.

All three transects revealed an increase in the number of crack-seal increments and in average crack-seal increment thickness for a limited distance away from fracture tips before reaching a roughly constant value of both parameters for the remainder of the fracture (Figures 4.4, 4.5). Average crack-seal increment thickness for cement bridges ranges between 3 and 14 μm. The calculated number of fracture opening increments ranges between 16 and 105, with the majority of cement bridges away from fracture tips containing 70-95 fracture opening increments.

For the two cement bridges that were reconstructed, crack-seal increment thickness is variable over the growth history of the bridges, ranging between 1 and 30 μm (Figures 4.2, 4.6, 4.7). No systematic trend toward wider or narrower cement growth increments can be discerned from older to younger increments. Additional bridge images and measurements are given in Appendix B.

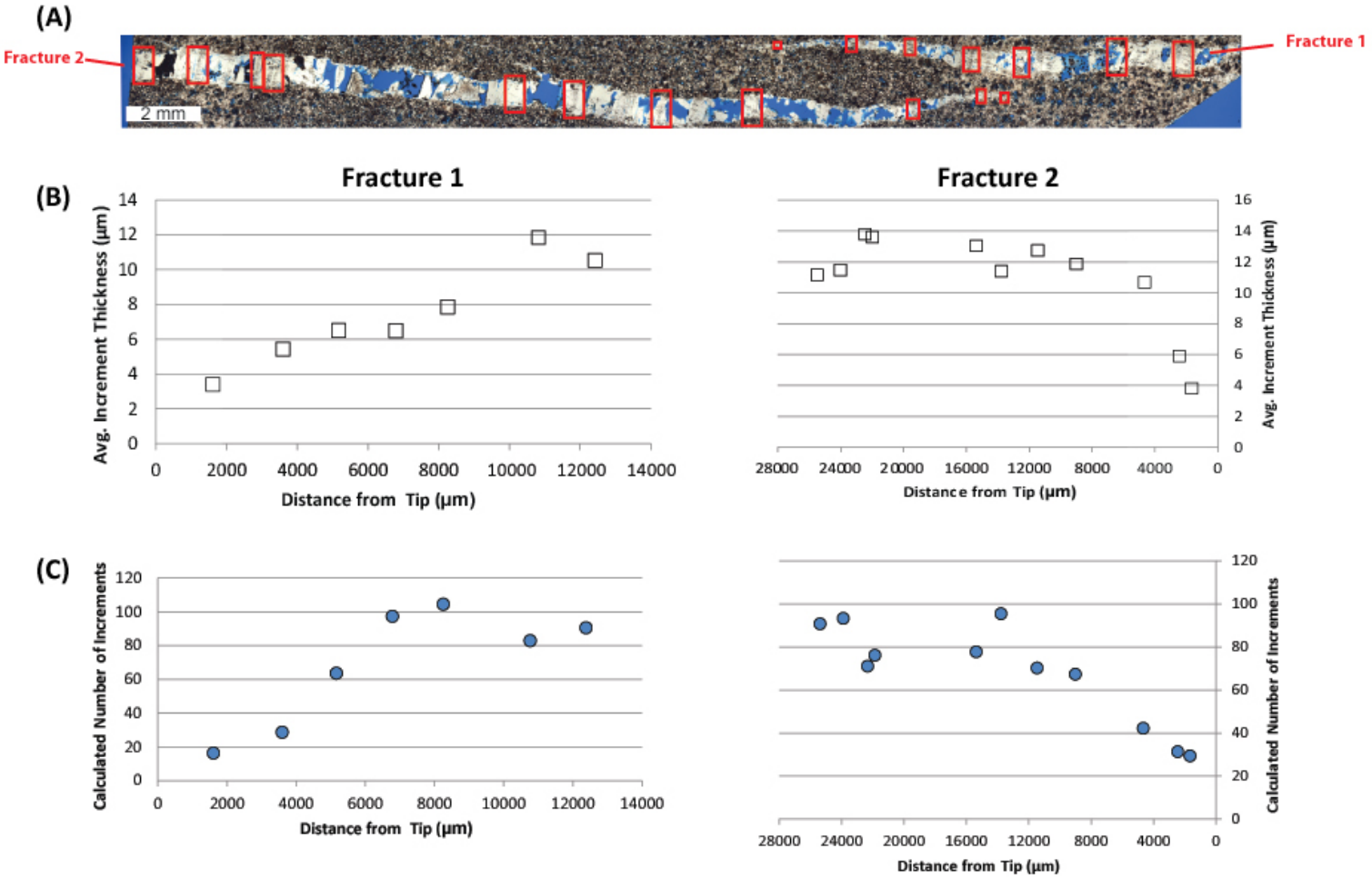

Figure 4.4: (A) Photomicrograph of two partially cemented en-echelon fractures imaged along strike (SFOT-1 well: depth 10,108.3'). Blue is epoxy filling remaining fracture porosity. Red rectangles indicate analyzed crack-seal cement bridges. (B)Average crack-seal increment thickness for positions along fracture dip indicated by red rectangles in A. (C) Calculated number of fracture opening increments for positions along fracture dip indicated by red rectangles in A.

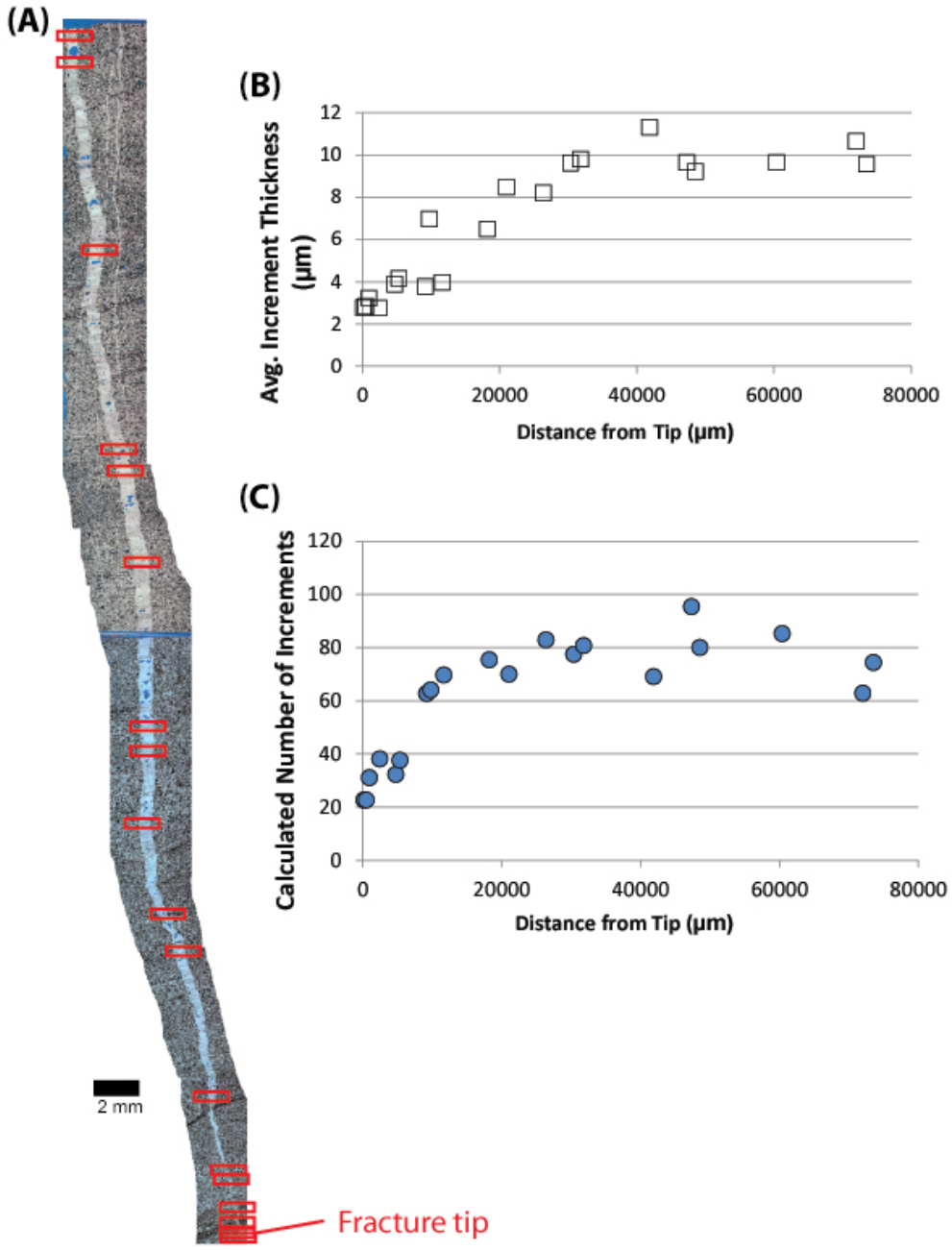

Figure 4.5: (A) Photomicrograph of a partially cemented fracture imaged parallel to the fracture dip (parallel to the core axis) (SFOT-1 well, depth of 10,107'). Red rectangles indicate analyzed crack-seal cement bridges. (B) Average crack-seal increment thickness for positions along fracture dip indicated by red rectangles in A. (C) Calculated number of fracture opening increments for positions along fracture dip indicated by red rectangles in A.

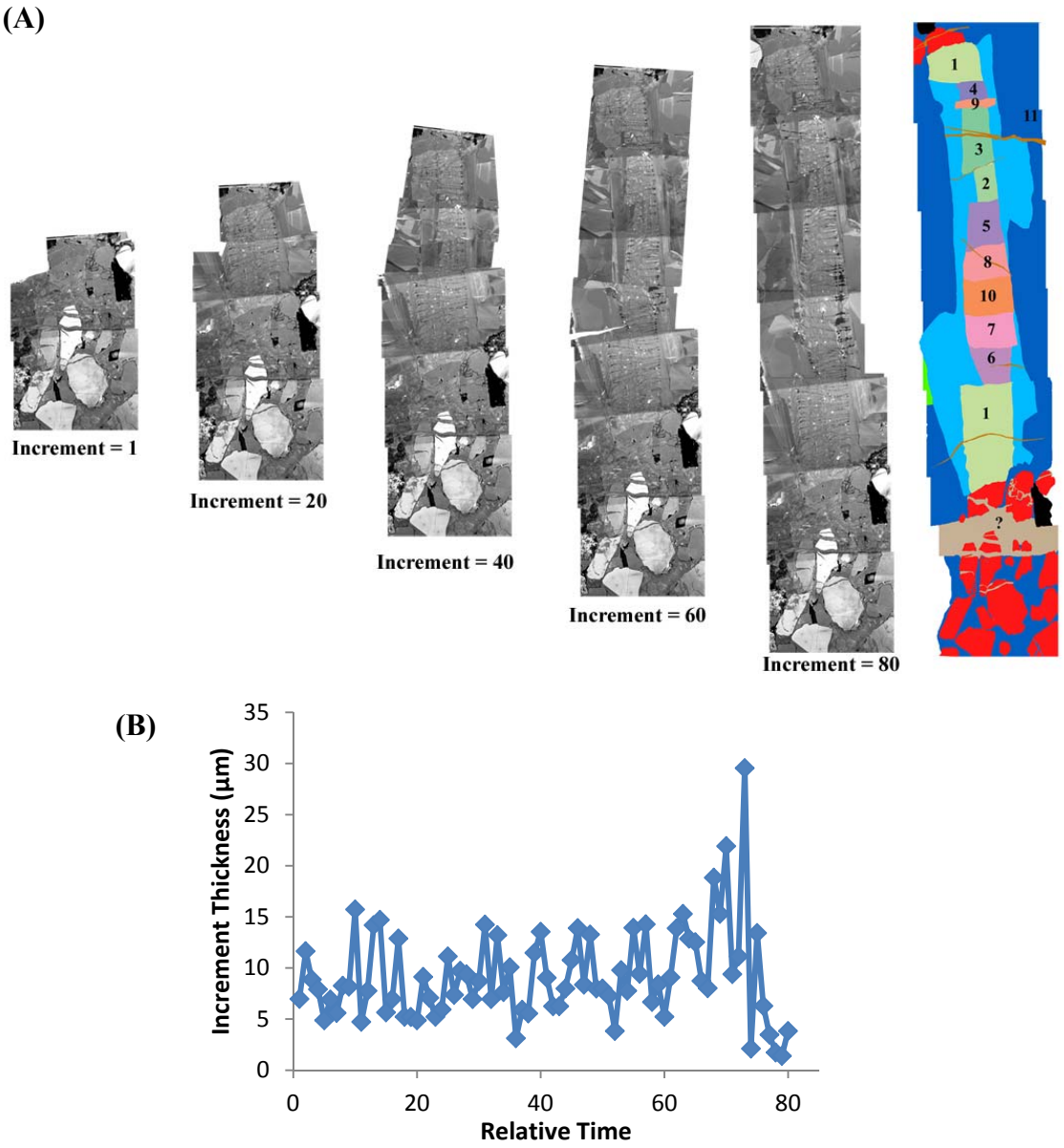

Figure 4.6: (A) Selected stages of a bridge reconstruction labeled by number of increments. (B) Crack-seal cement increment thicknesses plotted in order of relative time of formation.

(A)

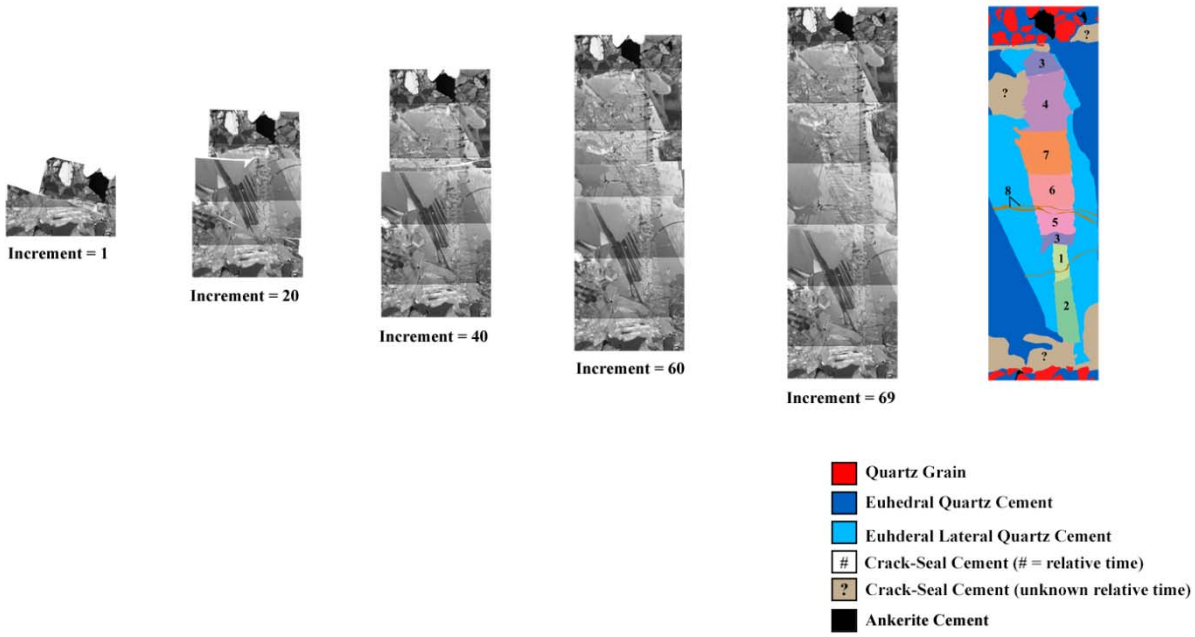

(B)

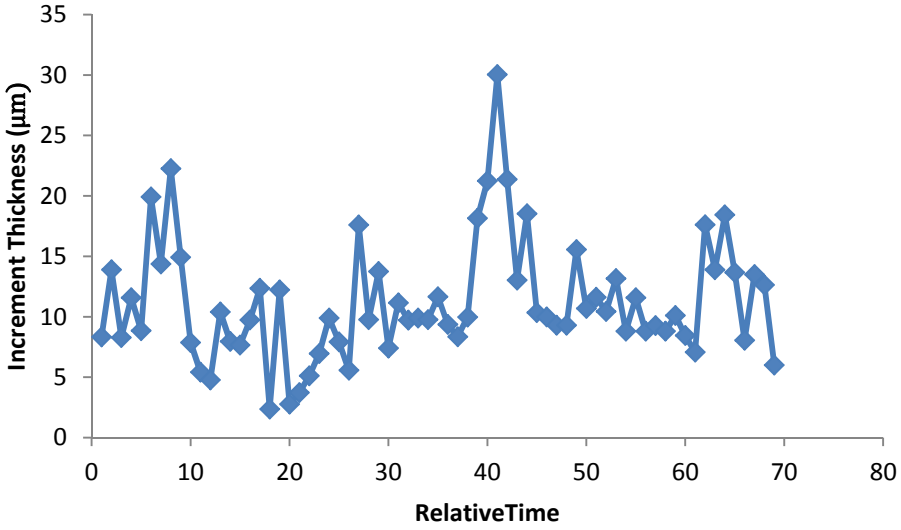

Figure 4.7: (A) Selected stages of a second bridge reconstruction labeled by number of increments. (B) Crack-seal cement increment thicknesses plotted in order of relative time of formation.

DISCUSSION

Geometric Analysis of Fracture Aperture Growth

Four geometric growth models for opening-mode fractures were tested against the fracture opening displacement data obtained from the SFOT-1 crack-seal cement bridges (Figure 4.8). (1) Fracture length and height growth occurred by tip propagation with concurrent aperture growth as expected for fracture growth in an elastic material (Figure 4.8A). In this case, the number of crack-seal increments is expected to decrease linearly toward the fracture tip while the average thickness of increments increases toward the tip (Figure 4.9A). Crack-seal increment thickness within a cement bridge is expected to decrease over time. (2) Fracture growth occurs by initial tip propagation and concurrent aperture growth to a finite fracture length and height, followed by a second stage of aperture growth without further propagation (Figure 4.8B). If the stage of initial fracture propagation resulted in only few aperture growth increments, with the majority of aperture growth occurring during the second stage, this type of fracture would result in a roughly constant number of opening increments along the length and height of the fracture, with thinner opening increments near the tip and thicker increments near the center of the fracture (Figure 4.9B). Aperture growth without propagation would imply change in elastic material properties or accommodation of fracture opening displacement by non-elastic deformation mechanisms such as solution-precipitation creep. (3) The third model, a variant of model 2, includes initial rapid length and height propagation with concurrent aperture growth, followed by a stage of slow propagation with relatively faster aperture growth (Figure 4.8C). As in model 2, the number of opening increments along the fracture would be roughly constant along the fracture length and height.

Opening increments would be thinner at the fracture tip compared to the fracture center (Figure 4.9C). (4) The fourth model assumes fracture propagation to a finite fracture height and continued growth in length. This model reflects fracture growth in layered sedimentary rock where bedding interfaces limit height growth (Figure 4.8D) (Corbett et al., 1987; Helgeson and Aydin, 1991; Underwood et al., 2003; Laubach et al., 2009). Because the short fracture dimension controls the fracture aperture (Gudmundsson, 2000), the aperture at the fracture center will stop growing once the final fracture height has been reached provided the elastic rock properties remain constant. For such a blade- or tunnel-shaped fracture, the number of fracture-opening increments would be constant along the fracture length or strike direction with exception of the near-tip region.

Observed trends in number of fracture-opening increments in the SFOT-1 fractures (Figure 4.4, 4.5), decreasing toward the fracture tips, are compatible with fracture propagation and thus with the first and third fracture growth models but inconsistent with the second model (Figure 4.8). The lack of a trend toward decreasing fracture-opening increments with time for any position along the fracture transect as observed in the bridge reconstructions (Figure 4.6B, 4.7B) is inconsistent with the first model which invokes thicker fracture-opening increments in the tip region than in the fracture interior, and thus in opening increments at any position along the fracture that decrease in size over time. The observed decrease in both the number of fracture opening increments and in average opening increment size at fracture tips is consistent with slow propagation and enhanced aperture growth as predicted in model 3. Model 4 of height-limited fracture growth fails to account for the observed decrease in the average opening increment size toward the fracture tip in the vertical fracture transect which I consider evidence of aperture growth with no or only slow vertical fracture propagation. However, height-limited fracture growth may be invoked for the second fracture growth phase in

model 3. The presence of both tall narrow fractures and short wide ones in the Travis Peak Formation (Laubach, 1989) can be explained by model 3; the narrow fractures growth history is dominated by fast propagation with concurrent widening while the wide fractures growth history is dominated by slow propagation relative to the rate of aperture growth. The presence of both fracture shapes concurrently indicates that fractures initiated at different times or underwent variable amount of the second phase of aperture growth. I thus consider the two-stage fracture growth model 3 to account for the observed fracture opening displacement data.

The apparently random and fluctuating increment thickness in the reconstructed crack-seal bridge (Figure 4.6B, 4.7B) may be evidence for the role of changing pore pressure over time in fracture growth. A similar fluctuating crack-seal increment thickness was also reported in the Travis Peak and other formations (Laubach et al., 2004a). Variation in pore pressure has been interpreted previously to have caused cyclic fracture growth (Bahat and Engelder, 1984; Lacazette and Engelder, 1992), and records of cyclically variable pore fluid pressure have been obtained through fluid inclusion analyses in crack-seal fracture cements (Fall et al., 2012, 2014).

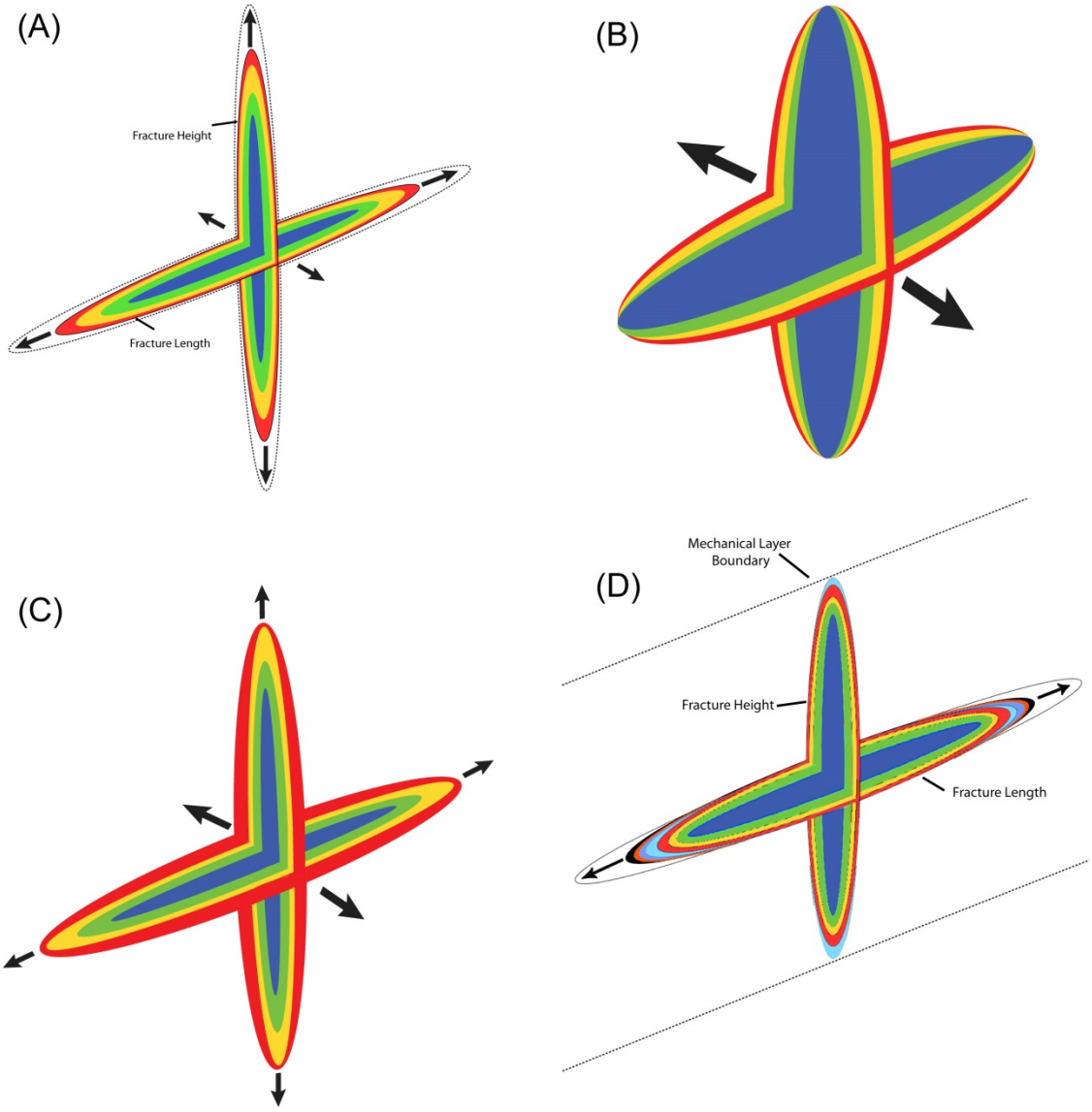

Figure 4.8: Models for fracture growth by propagation and aperture increase. (A) Fracture propagates both in height and length with concurrent aperture growth. (B) Stationary fracture model with aperture growth without propagation. (C) Two-phase fracture growth with initially fast propagation with concurrent aperture growth followed by slow propagation and pronounced aperture increase. (D) Fracture height growth limited by mechanical layer boundaries while horizontal propagation continues; aperture growth in center of fracture is limited by limited height growth. Opening kinematics of Travis Peak fractures resemble model C most closely.

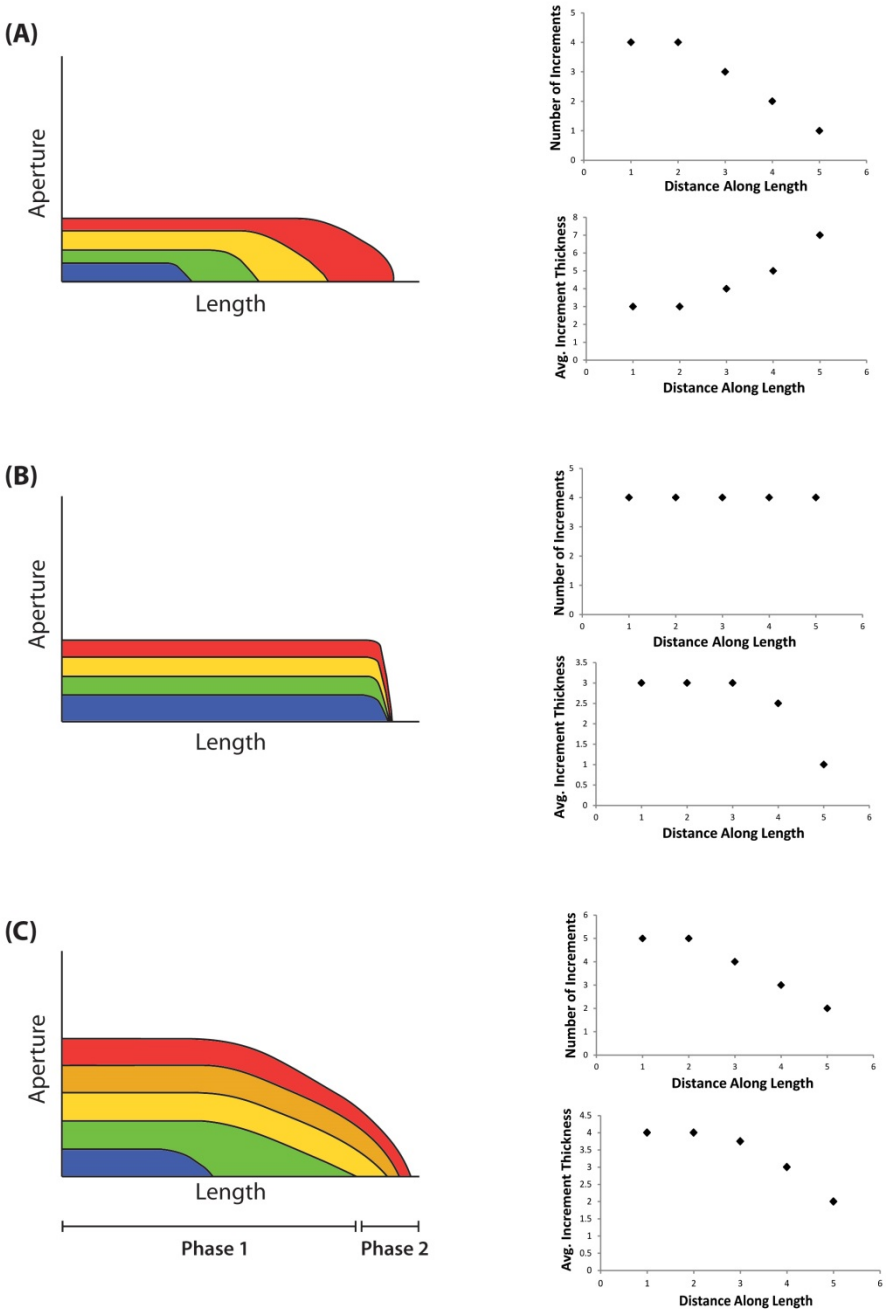

Figure 4.9: Predicted trends in thickness and number of fracture opening displacement increments for fracture kinematic models. (A) Proportional tip propagation and aperture growth, (B) aperture opening with no propagation (stationary fracture), (C) fast initial propagation with proportional aperture growth followed by slow propagation and sustained aperture growth.

Comparison to Linear Elastic Fracture Mechanics Predictions

For a quantitative analysis of the SFOT-1 fracture opening displacement results I compared measured cumulative fracture opening displacement for the two reconstructed bridges against theoretical predictions based on linear elastic fracture mechanics (LEFM) (Figure 4.10). Assuming constant elastic material properties, two scenarios of aperture growth can be distinguished: (1) Fracture growth by tip propagation with concurrent aperture opening (propagating fracture), here assumed to propagate at critical loading conditions with $K_I = K_{Ic}$ where K_I is the mode I stress concentration at the fracture tip, and K_{Ic} the mode I fracture toughness, a material property that quantifies the material resistance to fracture propagation; (2) Fracture aperture opening without tip propagation (stationary fracture). In this case, the fracture is assumed to have initially propagated to its finite length by either subcritical growth, or by critical growth followed by elastic unloading of the fracture. Any further loading that results in aperture growth remains below the critical loading stress for propagation.

The maximum opening displacement u_{max}, equivalent to half the maximum aperture, of a stationary penny-shaped mode-I fracture is given by

$$u_{max} = \frac{4(1-\nu^2)\sigma c}{\pi E} \quad \text{(Eq. 4-1)}$$

where σ is the loading stress (tension positive), υ is Poisson's ratio, c is the fracture half-length, and E is Young's modulus (Gudmundsson, 2011, p. 266-267).

For an opening-mode fracture that is critically loaded,

$$\sigma = \sigma_{Ic} = \frac{K_{Ic}}{Y\sqrt{\pi c}} \quad \text{(Eq. 4-2)}$$

where σ_{Ic} is the critical loading stress for mode I fracture propagation, K_{Ic} is the mode-I fracture toughness, and Y is a shape factor ($2/\pi$ for a penny-shaped fracture).

The opening displacement profile can be obtained through

$$u_x = u_{max}\sqrt{1-\left(\frac{x}{c}\right)^2} \quad \text{(Eq. 4-3)}$$

where u_x is the opening displacement at position x from the center of the fracture, i.e. from the location of maximum aperture.

From Eq. 4-2 it follows that, for fracture aperture growth concurrent with critical but stable tip propagation, the fracture driving stress required for propagation decreases with increasing fracture length. Increments in fracture opening displacement per unit length growth at any position x along the fracture thus decrease in size with increasing fracture length. Consequently, the slope of the cumulative opening displacement at any position x decreases with time (Figure 4.10, curved labeled propagating fracture). In contrast, for the stationary fracture, the fracture opening displacement scales linearly with the loading stress. At any position x, the slope in cumulative opening displacement over time is constant (Figure 4.10, curve labeled stationary fracture).

The observed cumulative fracture opening displacement for the two reconstructed cement bridges, showing a near-linear increase in fracture opening displacement with time, follows the trend predicted by the stationary fracture model but is inconsistent with the propagating fracture (Figure 4.10). This suggests that the initial phase of critical fracture propagation is either not recorded in crack-seal cement, or in too few crack-seal increments to be recognized in the cumulative fracture opening displacement plot. This result is consistent with the two-stage geometric fracture growth model 3 of fast initial propagation relative to the rate of aperture growth, followed by a stage of pronounced aperture growth and slow propagation.

Alternatively, or in addition, the linear slope of the cumulative fracture opening displacement curve may reflect subcritical fracture propagation under constant loading stress. Subcritical propagation is consistent with the slow rate of fracture opening of about 23 μm/m.y. based on the duration of fracture opening of 48 m.y. for a 1.1 mm wide bridged fracture in the Travis Peak Formation in the SFE-2 well (Becker et al., 2010).

The distinction between slow subcritical fracture growth and aperture growth in a near-stationary fracture cannot be made based on the curves in Figure 4.10. However, slow propagation is again consistent with the second growth stage of the two-stage geometric fracture opening model outlined above and found most consistent with the fracture opening displacement data.

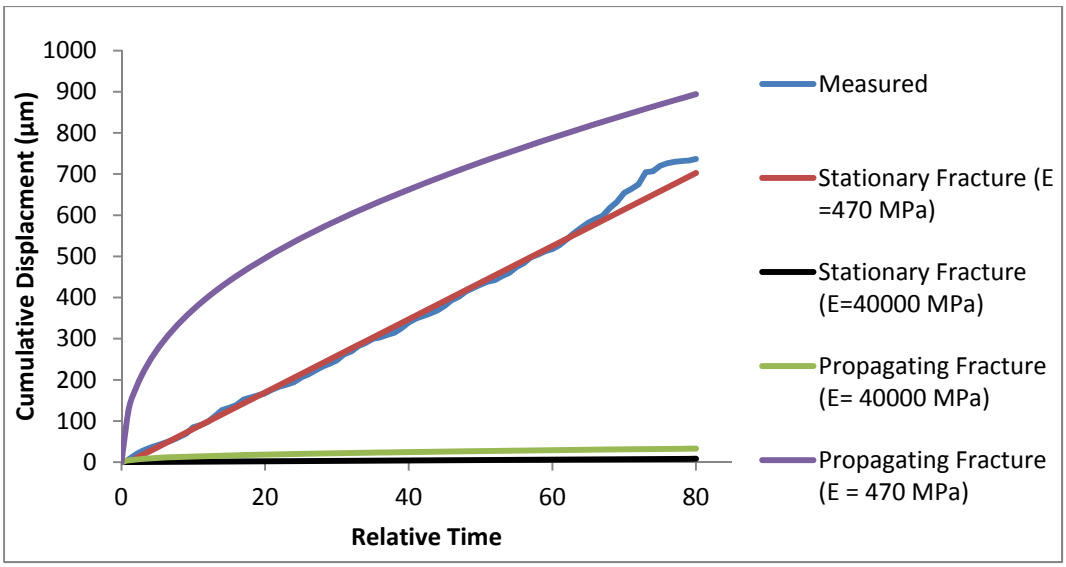

Figure 4.10: Cumulative fracture opening displacement for the reconstructed bridge in Figure 4.6. Shown for comparison are predicted cumulative opening displacements for propagating and stationary fractures calculated using material properties in Table 4.1.

Distance from location of maximum aperture [x] (m)	0.0064
Fracture half-length [c] (m)	0.0417
Young's modulus [E] (MPa)*	40000
Fracture toughness [K_{Ic}] (MPa/sqrt(m))	1.5
Shape factor [Y]	0.637
Poisson's ratio [υ] *	0.18

Table 4.1. Fracture and material properties used for calculation of cumulative fracture opening displacement (Figure 4.10). *Measured elastic rock properties from Jizba (1991). (c = 0 – 0.0417 m for propagating fracture).

Cumulative opening displacement curves in Figure 4.10 are shown for elastic properties of E = 40,000 MPa and υ = 0.18, elastic properties that were reported by Jizba (1991) for the Travis Peak Formation in the SFOT-1 core. To match the observed fracture apertures, a second set of curves was calculated with an "effective" best-fit Young's modulus E_{eff} = 470 MPa (Table 4.1). The low "effective" Young's modulus needed to account for the observed fracture opening displacement, two orders of magnitude lower than the measured value in core plugs, rule out a stationary linear elastic fracture opening process. Instead, I attribute the differences in lab-measured and "effective" Young's moduli to fracture strain accommodated by inelastic deformation processes such as solution-precipitation creep as proposed by Eichhubl and Aydin (2003) and Eichhubl (2004) for fracture growth in chemically reactive subsurface environments. The slow fracture opening rates proposed by Becker et al. (2010) in the Travis Peak Formation, and by Fall et al. (2012, 2014) in similar burial-diagenetic environments elsewhere, and synkinematic quartz precipitation resulting in bridge formation are consistent with fracture opening accommodated by solution-precipitation creep. While inelastic

deformation processes account for the finite fracture opening displacement, individual fracture opening increments likely represent episodic elastic strain events that alternate with periods of dissolution-precipitation creep converting elastic strain into permanent fracture strain.

CONCLUSIONS

Fracture opening displacement history is recorded in crack-seal cement textures of three opening-mode fractures in the Travis Peak Formation. Trends along fracture length and height in the number of fracture opening increments and in average increment thickness suggest that fractures grew by initial fast propagation relative to the rate in aperture growth, followed by a stage of slow propagation and pronounced aperture growth. Based on the cumulative opening increment distribution obtained through palinspastic reconstruction of two cement bridges that span the entire fracture aperture, I find that the crack-seal record reflects largely the second fracture growth phase of dominant aperture growth and subcritical fracture propagation under constant loading stress. These findings are consistent with earlier fluid inclusion microthermometric studies indicating that fracture cement bridges track fracture opening in the Travis Peak Formation spanning up to 48 m. y. In combination, these results support models of slow fracture growth in diagenetically reactive environments where fracture opening resulted from repeated episodes of elastic fracture opening, with the finite fracture opening accommodated by solution-precipitation creep.

Chapter 5: Evolution of Crack-Seal Fracture Shape

In this chapter I present observations on fracture shape from petrographic and SEM-CL images of the SFOT-1 fractures. Cement textures at sub-millimetric scale are best viewed using SEM-CL imaging. Similarly, measurements of kinematic aperture along fractures are most accurate when performed on SEM-CL images of the entire fractures. Owing to the optical continuity of quartz cement and quartz grains or grain fragments, microfractures, dislodged grains, and the exact fracture-to-grain boundary or fracture wall cannot be discerned easily for cemented or partially cemented fractures using standard transmitted light petrography. I compare these observations to fracture mechanics predictions of fracture tip geometry.

OBSERVATIONS IN FRACTURE KINEMATIC APERTURE

Systematic measurements of kinematic aperture every 200-500 μm were performed on SEM-CL images of two Travis Peak fracture traces to capture the fracture shape and aperture variation along fracture length and height. The objective was to test whether fractures in the Travis Peak have an elliptical shape as predicted by linear elastic fracture mechanics, and to what extent they deviate from the idealized shape (refer to chapter 2).

Measurements of kinematic aperture were taken for one fracture along its length (fracture 1), and for the second fracture along its height (fracture 2). Tables 5.1 and 5.2 present measured parameters for the two fractures including their dimensions. Kinematic aperture measurements for the two fractures range between zero at the tip and up to 329 and 920 μm respectively at the center (Figure 5.1, 5.2). The increase of kinematic aperture toward the fracture center is irregular and varies between evenly spaced measurements; amount of increase between neighboring measurements range from less

than 10 micron up to ~250 micron. Aperture profile of fracture 1 is approximately symmetrical across a vertical axis through the fracture center (Figure 5.1). The decrease in kinematic aperture near the fracture tip is gradual.

Fracture tips observed in SEM-CL images (Figure 5.1, 5.4) do not terminate in a single tip but dissipate into many smaller microfractures. The left fracture tip in Figure 5.1 overlaps an adjacent fracture (see Figure 5.3); the overlap does not correspond with a change in macrofracture tip geometry when observed under standard petrography. However, SEM-CL images of the overlap area shows that microfractures at the tip are in close proximity (<500 micron) to the adjacent fracture (Figure 5.4). The tip and associated microfractures are in an intersecting path with the adjacent fracture.

Fractures in Figure 5.3 appear to display different stages of linkage. While some appear not to be hard linked under transmitted light petrography, SEM-CL images reveal that all but the rightmost fracture are hard linked. Linkage is observed to occur between a fracture tip and a point near the other fracture tip, leaving host rock wedged between the linking tip and the other fracture tip. Further aperture growth may continue on the main fracture and abandon one tip. While further aperture growth may merge the two fracture segments beyond recognition, the abandoned tip (relict tip) may remain as a small branch and serve as evidence for a linkage zone (Laubach and Ward, 2006). Fracture 2 (Figure 5.2) has few minor branches that resemble abandoned fracture tips observed in Figure 5.3. All abandoned tips correspond to local minima in kinematic apertures. However, there are local minima in kinematic apertures that do not correspond to abandoned tips.

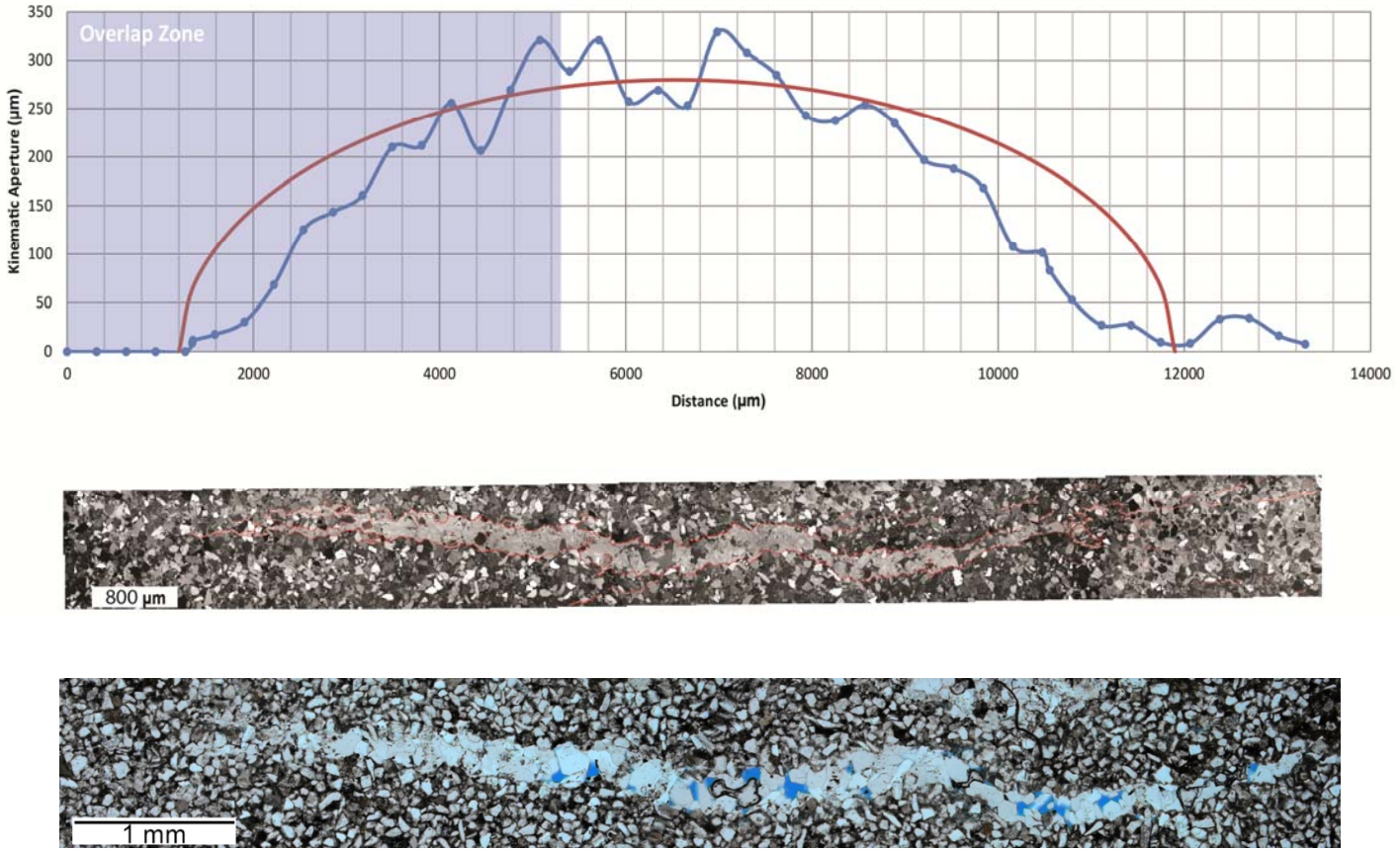

Figure 5.1: **Top**: Kinematic aperture profile from SEM-CL images (blue curve) for fracture 1. The red curve is the visual best elliptical fit. Purple shade indicates zone where fracture is overlapping with another one. **Middle**: Blue filter SEM-CL images of a length transect of fracture 1-SFOT-1 (10,106'), fracture walls are marked with red. **Bottom:** Petrographic image of the same fracture where fewer details are visible, but better view of fracture porosity (blue).

Length (μm)	12,030
Maximum Kinematic Aperture (μm)	329
Aspect Ratio	1:36.6
Visual Porosity (estimated %)*	10
Cement	Euhedral quartz with few crack-seal quartz bridges

Table 5.1: Fracture properties for Travis Peak fracture 1 in SFOT-1- 10,106' (refer to Figure 5.1) * Fracture porosity is the percentage of fracture volume not filled with cement.

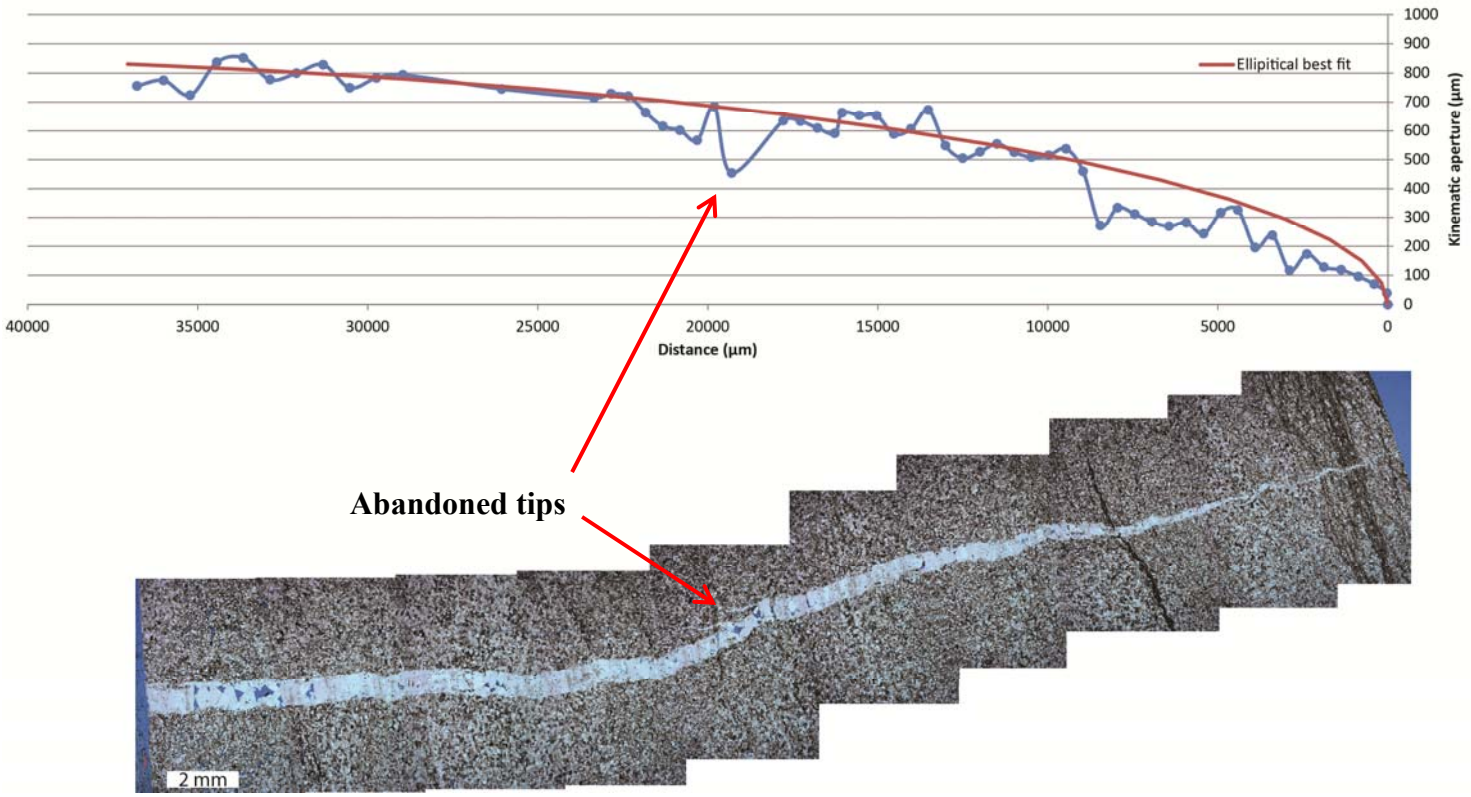

Figure 5.2: **Top:** Kinematic aperture profile from measurements on SEM-CL images of part of fracture 2 sampled along its height. **Bottom:** Petrographic image of the fracture corresponding to the graph from SFOT-1-10,107 ft. Abandoned tips indicate zones where linkage may have occurred.

Minimum Height (μm)	116,368
Maximum Kinematic Aperture (μm)	920
Minimum Aspect Ratio	1:126.5
Visual Porosity (estimated %)	5
Cement	Dominantly quartz cement (Crack-seal and euhedral), minute amount of ankerite

Table 5. 2 : Fracture properties for Travis Peak fracture 2 in SFOT-1 samples 10,106.7-10,107 ft (refer to Figure 5.2). Note that data in the table represents the entire fracture and not only the partial sample shown in figure 5.2. True height and aspect ratio could not be obtained because the other fracture tip was not sampled in the core.

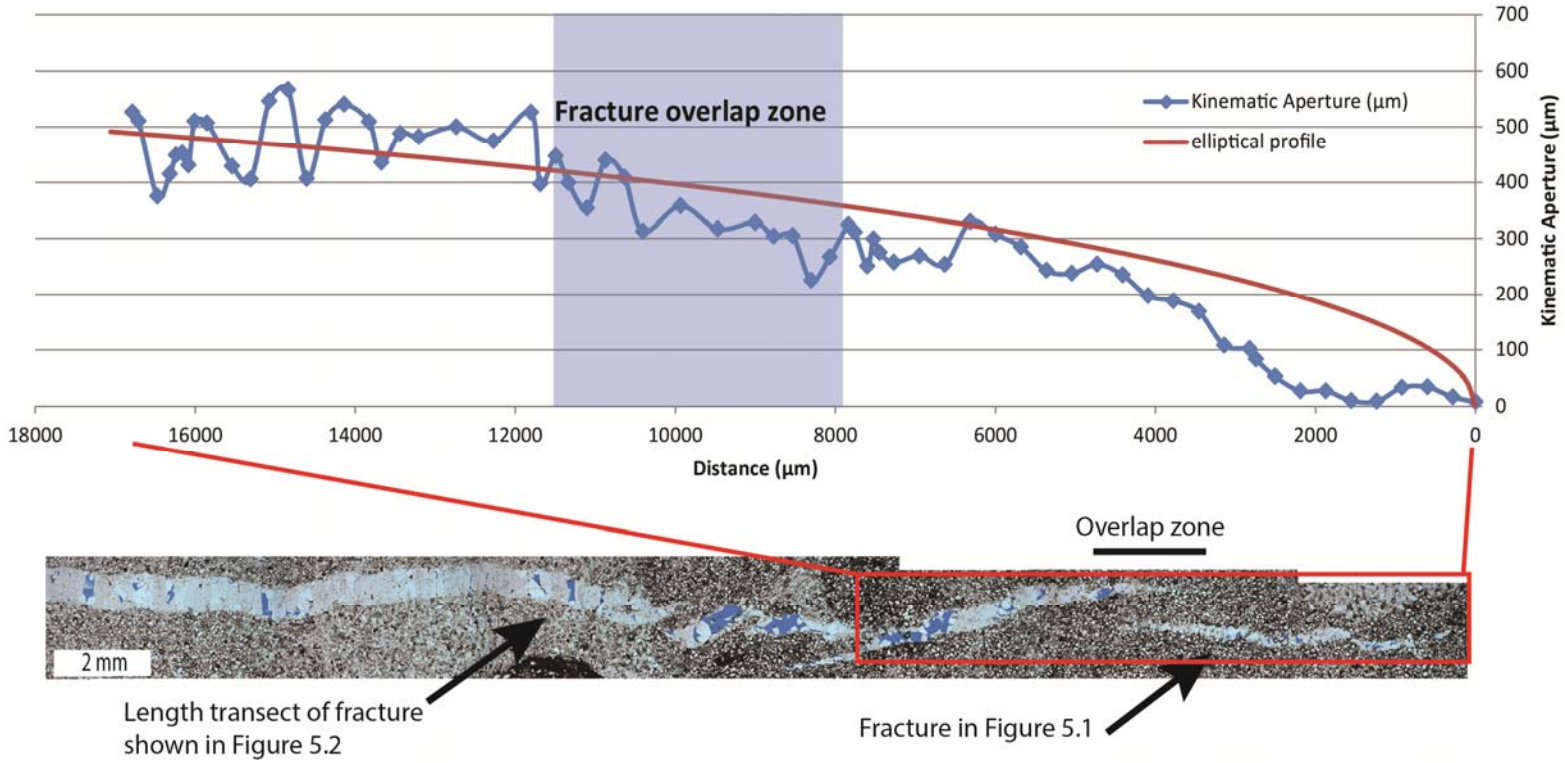

Figure 5.3: **Top:** Combined kinematic aperture profile measured from SEM-CL images for two fractures, up to 100 micron deficit from elliptical profile is present in the fracture overlap zone. **Bottom:** petrographic image of fractures from SFOT-1-10,106 ft, the four fractures to the left are hard linked whereas the one to the right is soft linked.

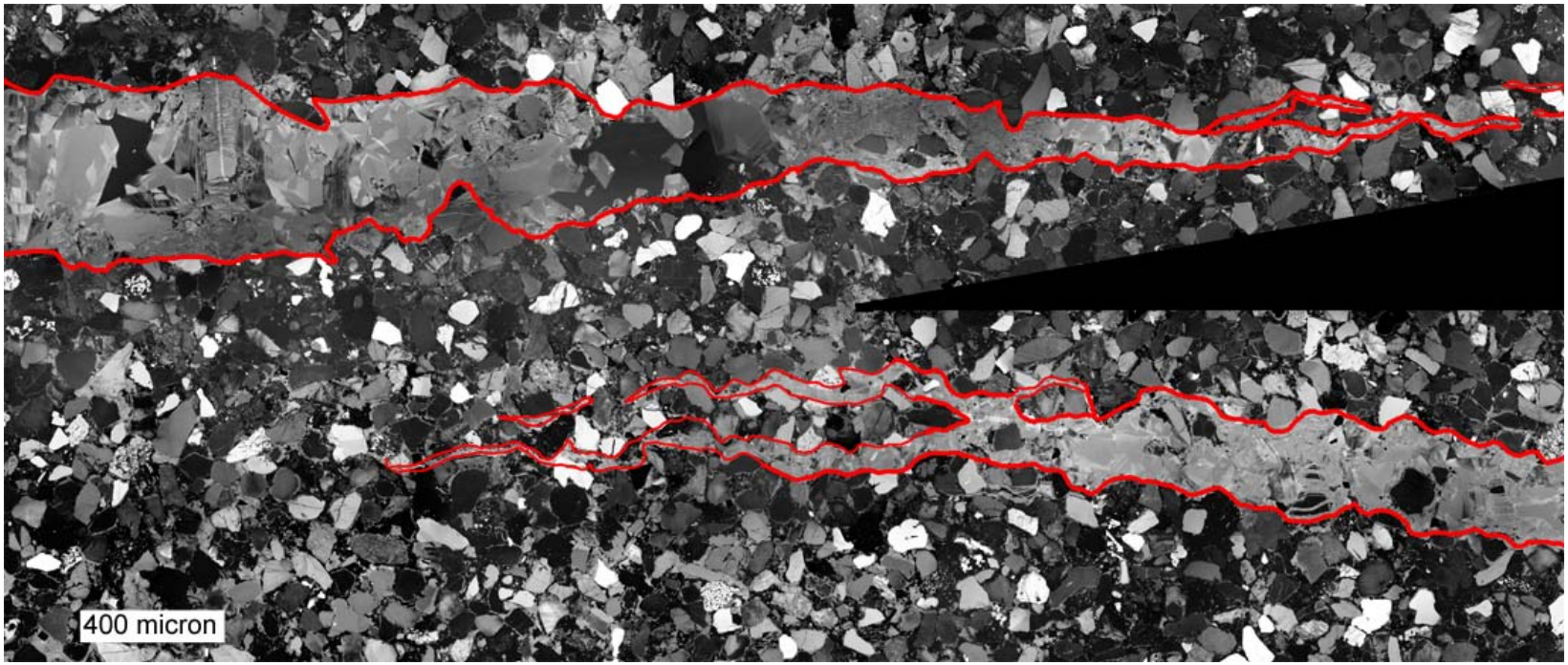

Figure 5.4: Blue-filter SEM-CL image of the overlap zone marked in figure 5.3 between two fractures. Red line marks the fracture walls and some of the microfractures associated with the macrofracture tip.

DISCUSSION:

Fracture Mechanics Approach to Fracture Geometry

Linear elastic fracture mechanics predicts that loading stress ahead of the fracture tip is inversely proportional to the square root of the distance from a fracture tip resulting in a stress singularity at the fracture tip. Dugdale (1960) proposed a simple model to account for the non-physical nature of the stress singularity by introducing a plastic zone ahead of the crack tip and a smooth closure of the crack faces. Barenblatt (1959, 1961) also presented a similar model applicable to pure brittle fractures where cohesive forces result in a smooth joining of the fracture walls toward the fracture tip. Both models postulate that growth of cracks is associated with the formation of a narrow band (process zone) near the tips where nonlinear deformation occurs. Based on these two models the bridged-crack and cohesive-crack models have emerged to explain non-linear deformation at the crack tip of quasi brittle material (e.g., concrete, rocks, ceramics…etc) (Massabo, 1999). In these models, the process zone consists of a micro-cracking zone, bridging zone, and a traction-free zone (Figure 5.5). In high-strength materials, the micro-cracking zone may be much smaller than the bridging zone (Figure 5.5B). The microcracks are formed ahead of the crack tip and initiate from nearby flaws. In the bridging zone, second phase particles such as grains, fracture cement, or, in fiber-reinforced ceramics, fibers restrain the macrocrack from opening. The process zone in these models is envisioned as a fictitious crack ahead of the existing macrocrack, where the non-linear mechanism is represented as distribution of closing tractions (σ_0) acting on a fictitious crack (Figure 5.5-II). The difference between a cohesive and bridged-crack is that the stress field for a cohesive crack is finite and $K_I = 0$ while a bridged-crack stress field is singular and $K_I \neq 0$. This dictates that the shape of a cohesive crack tip to be tapered and a bridged-crack tip to be somewhat rounded (Figure 5.6).

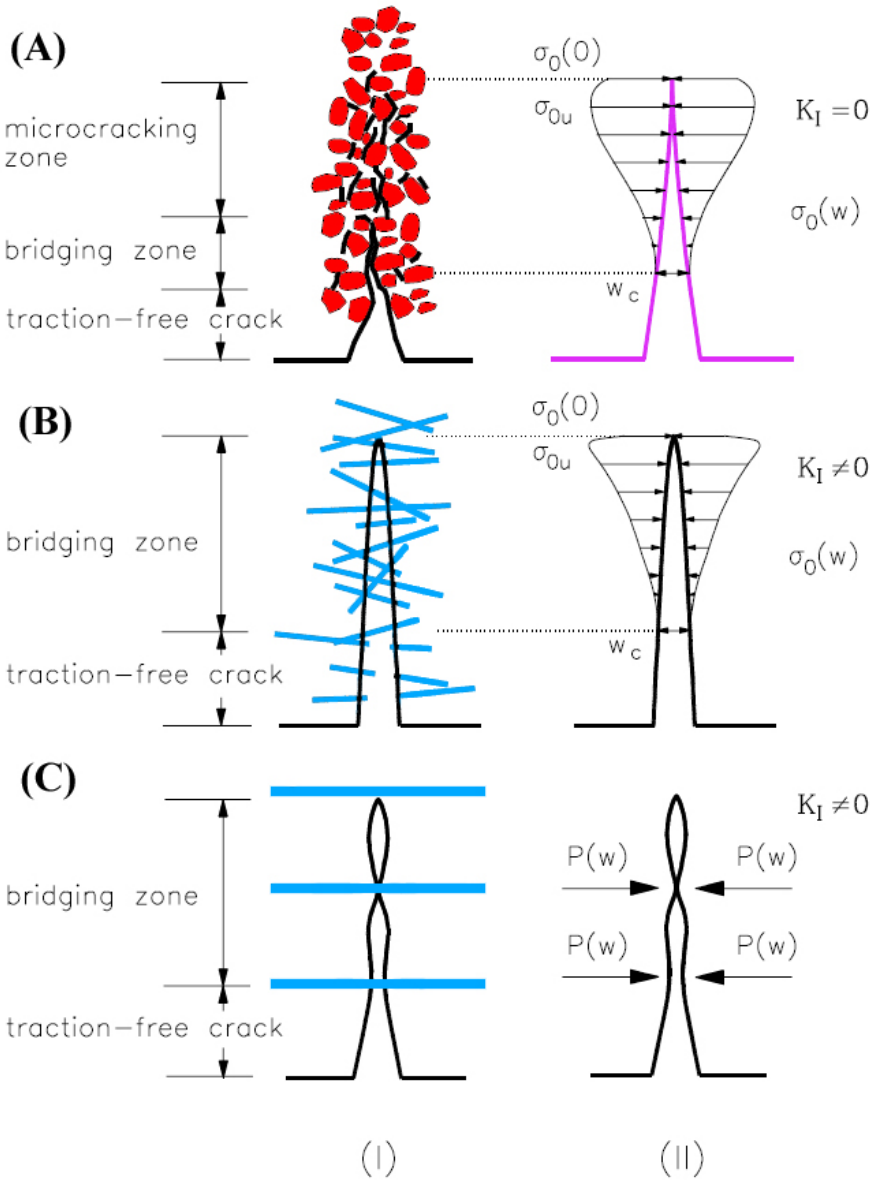

Figure 5.5: (A) Schematic of a cohesive-crack with micro-cracks in the process zone (e.g., concrete and rocks). (B) Schematic of uniformly bridged-crack (e.g., fiber-reinforced high-strength concrete. (C) Schematic of bridged-crack with discontinuous reinforcements (e.g., reinforced concrete) (Modified from Massabo, 1999).

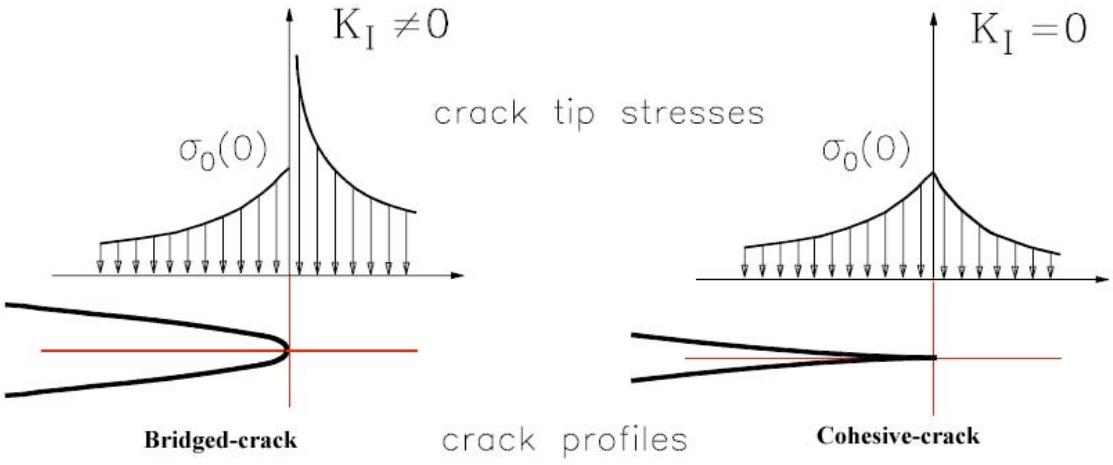

Figure 5.6: Comparison between cohesive-crack and bridged-crack tip profile and associated stresses (Modified from Massabo, 1999).

Since linear elastic fracture mechanics predicts an elliptical fracture shape (See chapter 2), an elliptical profile (red curve, Figure 5.1, 5.2) was visually fitted to the data for comparison. Near the tips, the measured fracture opening displacements display a distinct deficit in opening displacement compared to the elliptical profile especially. In fracture 1 (Figure 5.1), the deficit is up to 100 mm in kinematic aperture near the tips of the fracture compared to the visually fitted elliptical profile. Instead of a rapid decrease in kinematic aperture near the tips, the profile decreases gradually in opening displacement before terminating. The deviation from an elliptical profile is observed both in the length transect (Figure 5.1, 5.3) and the height transect (Figure 5.2).

Microfractures are observed ahead of fracture tips (e.g. Figure 5.1), which is consistent with the concept of a damage zone composed of microcracks ahead of the macroscopic fracture tip. The presence of synkinematic quartz cement within the fractures may have contributed cohesive forces restraining fracture growth in the bridging zone. Also, macrofractures kinematic aperture profiles near the tips are smooth and

tapering. These observations in the SFOT-1 fractures (Figures 5.1, 5.2, 5.3) are consistent with the cohesive-crack model. To the best of my knowledge, this is the first time cohesive zone features have been recognized in brittle rocks. Both the microfractures and tapering tip profile are only visible in SEM-CL images. Further investigation is needed to determine how much control synkinematic crack-seal bridges impose on fracture tip profile.

Fracture Linkage Control on Geometry

Observations in the SFOT-1 fracture aperture profiles suggest that local sharp decrease in kinematic aperture is related to past linkage zones. Evidence of linkage zones such as abandoned fracture tips always correspond to a local minimum in kinematic aperture. Some local minima in the fracture profile do not correspond to clear past linkage zones. However, these are possibly related to linkage zones that have matured and coalesced beyond recognition of individual segments. When combining the kinematic apertures of two overlapping fractures a deficit is observed in the fracture overlap zone when compared to the geometry of an elliptical fracture profile (Figure 5.3). In addition, Figure 5.3 displays varying degrees of hard linkage. The least mature stages of hard linkage appear to correspond with the greatest decrease in kinematic aperture. Some fractures appear to have rotated in response to linkage, resulting in a sigmoidal fracture shape Sigmoidal shapes of en-echelon fracture arrays have been attributed to mechanical interaction between fractures (Nicholson and Pollard, 1985; Pollard et al., 1982). Olson and Pollard (1991) numerically modeled the growth of en-echelon arrays of opening mode fractures and reproduced the sigmoidal fracture traces observed for natural fractures (Figure 5.7). Fractures that are not observed to be hard linked in thin section

may actually be hard linked in the third dimension, out-of-plane relative to the thin section.

These observations are contrary to predictions of linear elastic fracture mechanics, where the coalescence of two fractures is expected to immediately cause an adjustment of fracture aperture to maintain an approximately elliptical fracture geometry (Kishimoto et. al., 1989). I speculate that the deficit in fracture opening displacement around hard links results from inelastic deformation processes.

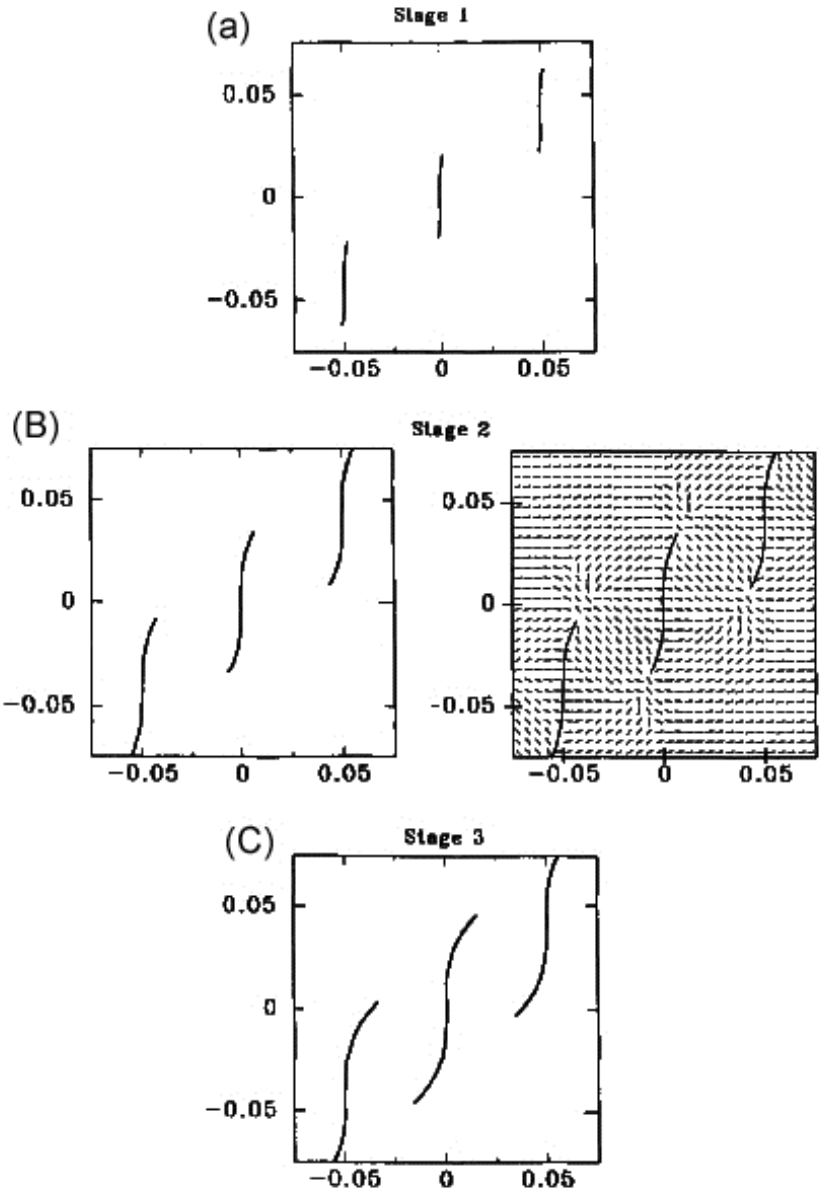

Figure 5.7: Three progressive stages of sigmoidal fracture evolution in response to uniaxial stress along the x-axis. (A) Planar traces with fracture propagation perpendicular to extension. (B) **Left**: the initiation of mechanical interaction where fracture tips start to curve; **Right:** maximum principle strain trajectories. (C) Final state resulting in sigmoidal shaped fractures. (Olson and Pollard, 1991).

Chapter 6: Conclusions

Textures of crack-seal fracture cement bridging fractures in the Travis Peak Formation were imaged using SEM-based cathodoluminescence for a kinematic analysis of fracture opening. Plots of the number of fracture opening increments and of average increment size against distance from the center of the fracture revealed constant values for both in the center of these fractures, and decreasing values for both size and number of increments toward the tip in the tip region. In addition, I reconstructed two cement bridges with complete crack-seal records across the fracture kinematic aperture. Crack-seal opening increment thickness derived from these reconstructions reveal variability in increment thickness but no trend toward thinner or thicker increments over time.

I compared these results against four kinematic models of three-dimensional fracture length and aperture growth. The first model assumes that fracture opening was concurrent with tip propagation with decreasing opening increments toward the center of the fracture. The model predicts proportional growth in both length and height. The second model assumes fracture propagation to a finite length with subsequent aperture growth. The third model predicts an initial phase of concurrent propagation and opening followed by a phase were aperture opening is dominant with relatively slow propagation. The fourth model predicts that fracture opening is restricted to a finite aperture at the center as a result of restricted fracture height growth at mechanical layer boundaries whereas length growth by tip propagation is unrestricted. The observed trends in fracture opening increment number and average size are consistent with model 3 but inconsistent with model 1, 2, and 4. Height-limited growth (model 4) in combination with slow propagation (model 3) is possible but cannot be confirmed with the available data. The variability in crack-seal increment size observed by bridge reconstruction may indicate

fluctuations in fracture-driving pore fluid pressure as suggested previously in other studies of fractures in gas reservoirs. Comparison of my results with linear elastic fracture mechanics models of stationary and propagating fractures are consistent with an initial phase of concurrent propagation and opening followed by a phase were aperture opening is dominant with relatively slow propagation (model 3) and are suggestive of subcritical fracture growth. Observed fracture apertures are indicative of fracture strain accommodated by non-elastic permanent strain such as solution-precipitation creep.

Contrary to expectations from LEFM, fracture linkage imposes control on the kinematic aperture profile of fractures even when linkage is in a mature stage. Local minima in kinematic aperture profiles correspond to past linkage zones. This suggests inelastic deformation behavior or a temporal change in the rock elastic properties. In agreement with previous studies, fracture tip interaction was observed to have influence on fracture trace geometry when fractures are close to each other.

One unexpected finding of this study is the documentation of a cohesive fracture tip in brittle sandstone where microfractures are present ahead of the fracture tip and synkinematic quartz cement may have played a role in restraining fracture opening at the tip resulting in tapering tip geometry. These observations are consistent with published fracture mechanics theoretical models and confirm their validity in brittle rocks. Such findings were only possible because of high resolution SEM-CL imaging of entire fractures.

In conclusion, fracture growth inferred from crack-seal cement textures can provide valuable information about the behavior and history of fracture. The results reveal processes of fracture propagation and opening that are significantly more complex than models based on linear elastic fracture mechanics. While linear elastic fracture mechanics models provide useful predictions for many aspects of fracture growth in

geologic systems, non-LEFM behavior of fractures may significantly affect the size of fractures and thus fracture network and flow properties in otherwise tight reservoirs.

Appendix A: Observations in Crack-seal Increments

The majority of crack-seal increments are roughly parallel to the fracture walls. However, few increments cutting other increments obliquely is a common observation in cement bridges (e.g., Figure B. 201). There are few exceptions where most increments in a bridge are oriented 45-60 degrees from the fracture walls (e.g., Figures B.8, B.9). This is observed in bridges located within or near linkage zones.

Crack-seal increment thickness varies within a quartz bridge and between different bridges as well. Observed increment thickness ranges between ~1 and ~30 μm. Increments ≤ 1 μm may be present but cannot be readily observed and measured. The average increment thickness is used to compare change in thicknesses between bridges. Fractures sampled along their height and length alike, show a decreasing increment average thickness toward fracture tips. The estimated number of increments at crack-seal bridges also decreases toward fracture tips.

Often crack-seal bridges are observed to have somewhat chaotic texture, where individual increments are not readily distinguishable. The apparently chaotic texture may be the result of one or several factors including actual complex crack-seal textures, thin section cutting orientation relative to the bridge, or image resolution limitations.

Increments arrangement and shape varies among examined bridges. Individual increments can be easily distinguished when they have a tabular shape and a regular stacking on top of each other. Often crack-seal increments are coated on the sides by layers of lateral euhedral quartz cement. Another feature that aids in distinguishing individual increments is the dark luminescent triangles frequently lining increment edges (e.g., Figure B.20). These features were not described before in the literature and there is no current explanation for their presence. The triangles point toward the crack-seal

cement growth direction. Hence, I suggest the term growth triangles. The growth triangles can also be used to distinguish half increments from a full increment (Figure A.1). A full increment has two set of triangles pointing toward each other. While half an increment would have one set of triangles. The size, number, and quality of growth triangles vary from bridge to another and among increments of the same bridge. The best growth triangles are observed in the largest crack-seal increments.

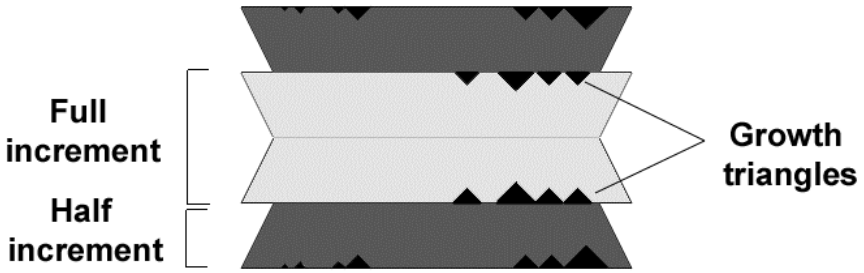

Figure A.1: A schematic drawing showing growth triangles in crack-seal increments and their use in distinguishing between full increments and half increments.

Grain fragments or entire grains are often observed to be dislodged from fracture walls and embedded in crack-seal bridges. The degree of grain fragmentations vary with grain size relative to the bridge and the amount of displacement at the bridge. Entire grains can be found intact within fracture fill, but when a grain is embedded in a cement bridge it is often fragmented by crack-seal increments. Most cases grain fragments can be visually pieced back together. The degree of grain fragmentation in crack-seal bridges vary from splitting the grain into two halves (e.g.: Figure B. 16) to distributing the grain over the entirety of the bridge (e.g.:Figure B. 17). Grain fragmentation by crack-seal

increments dominates the texture of bridges near fracture tips with less prominence near the center of fractures.

Appendix B: Fractures and Bridges Data

Sample Depth: 10,108.3’

Formation: Travis Peak

Fracture sampling orientation: Length (i.e.: perpendicular to core)

Figure B. 1: Petrographic image of SFOT-1-1,108.3’. **Fracture 1** (bottom left) contains remnant tips of previously isolated fractures; fracture visual porosity (blue) is estimated to be 30%. **Fracture 2** (top right) is in close proximity to the tip of fracture 1; fracture visual porosity is around 23%. The dominant type of cement is quartz and small amounts of ankerite. Labeled quartz bridges (B#) were imaged using SEM-Cl.

SFOT-1-10,108.3- FRACTURE 1

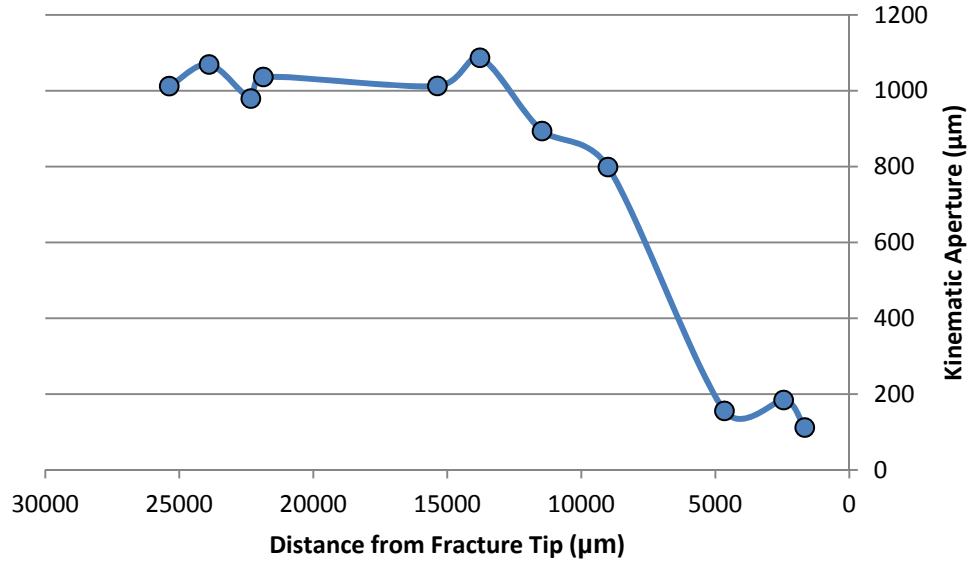

Figure B. 2: Kinematic aperture of Fracture 1 at the location of examined bridges.

Bridge Measurements Summary

Relative Distance	Bridge#	Distance From Tip (µm)	Kinematic Aperture (µm)	Average Increment Thickness (µm)	Standard Error in Avg. Thickness (+/-)	Estimated Number of increments
1	7	1661.6	111.89	3.82	0.37	29
2	8	2450.8	184.35	5.89	0.49	31
3	9	4657.4	155.92	10.67	1.37	42
4	10-11	9005.2	798.79	11.87	1.19	67
5	F	11463.2	893.65	12.73	1.27	70
6	G	13782.6	1086.89	11.38	0.91	95
7	H	15369.6	1012.70	13.04	0.94	78
8	D	21862.7	1036.19	13.60	0.74	76
9	1	22327.4	979.24	13.79	1.21	71
10	C	23888.6	1069.18	11.46	0.87	93
11	E	25374.1	1012.33	11.15	0.81	91

Table B. 1: Summary of cement bridge measurements in Fracture 1- SFOT-1-10,108.3'.

SFOT-1-10,108.3- Fracture 1 Bridge Images and Measurements

Note: Bridges images and measurements are in ascending order according to their distance from the fracture tip. Measurement angles are in degrees (0 = horizontal).

Bridge 7

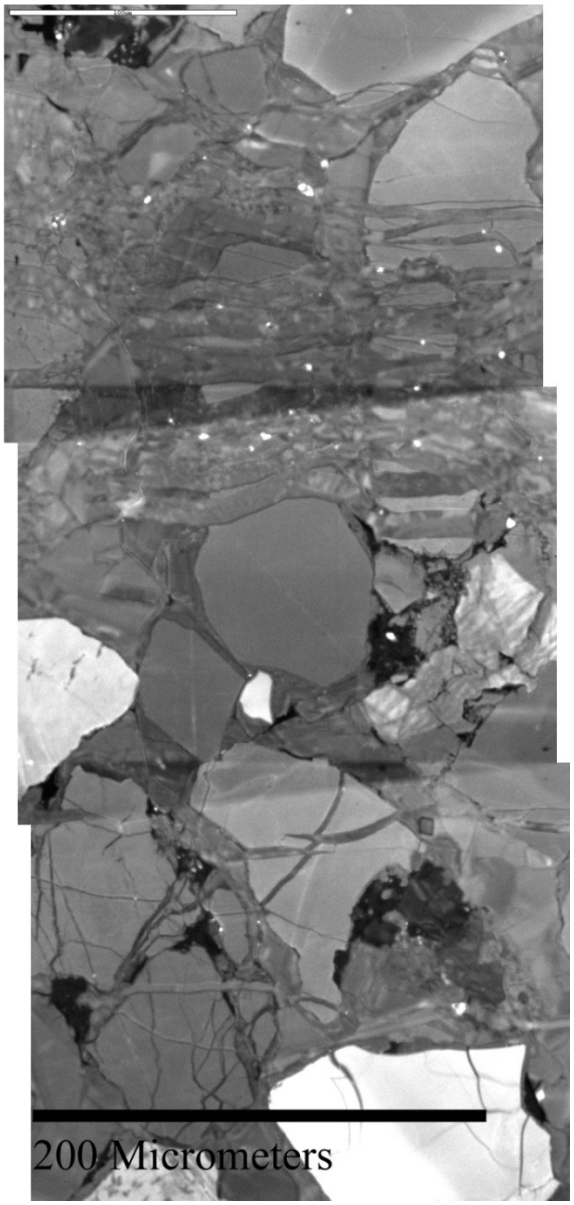

Figure B. 3: Panchromatic SEM-CL image of Bridge 7. Embedded grain fragments are embedded through the quartz bridge.

Increment #	Measured Thickness (μm)	Measurement Angle (degrees)
1	2.3	90
2	3.2	73
3	4.2	81
4	4.2	90
5	3.7	90
6	4.5	55
7	5.0	101
8	4.0	80
9	1.6	90
10	5.5	102

Table B. 2: A list of crack-seal increment thickness measurements for bridge 7 with measurement angle relative to the SEM-CL image.

Bridge 8

Figure B. 4: Panchromatic SEM-CL image of bridge 8. Some crack-seal increments in the middle of the bridge are inclined relative to the fracture walls.

Increment #	Measured Thickness (μm)	Measurement Angle (degrees)
1	6.2	103
2	4.6	90
3	4.2	96
4	5.6	90
5	7.5	97
6	6.3	107
7	9.6	104
8	4.8	107
9	7.1	113
10	7.0	90
11	5.7	76
12	2.5	68
13	4.0	69
14	4.6	90
15	8.9	81

Table B. 3: A list of crack-seal increment thickness measurements for bridge 8 with measurement angle relative to the SEM-CL image.

Bridge 9

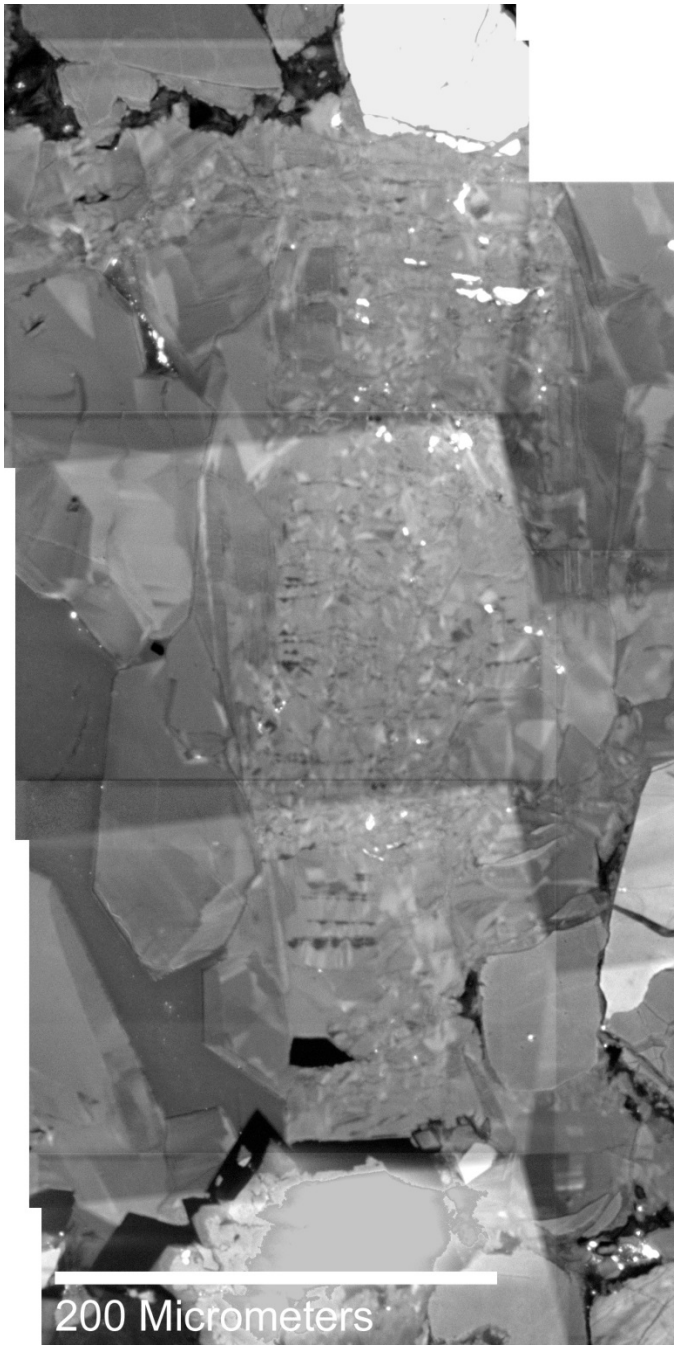

Figure B. 5: Panchromatic SEM-CL image of bridge 9. Fragments from the white quartz grain at the upper fracture wall are observed to be displaced within the crack-seal cement bridge.

Increment #	Measured Thickness (µm)	Measurement Angle (degrees)
1	12.9	92
2	9.8	98
3	17.1	85
4	8.8	81
5	9.7	92
6	13.9	93
7	16.3	89
8	4.7	117
9	4.5	94
10	9.0	90

Table B. 4: Bridge 9 crack-seal measurements.

Bridge 10-11

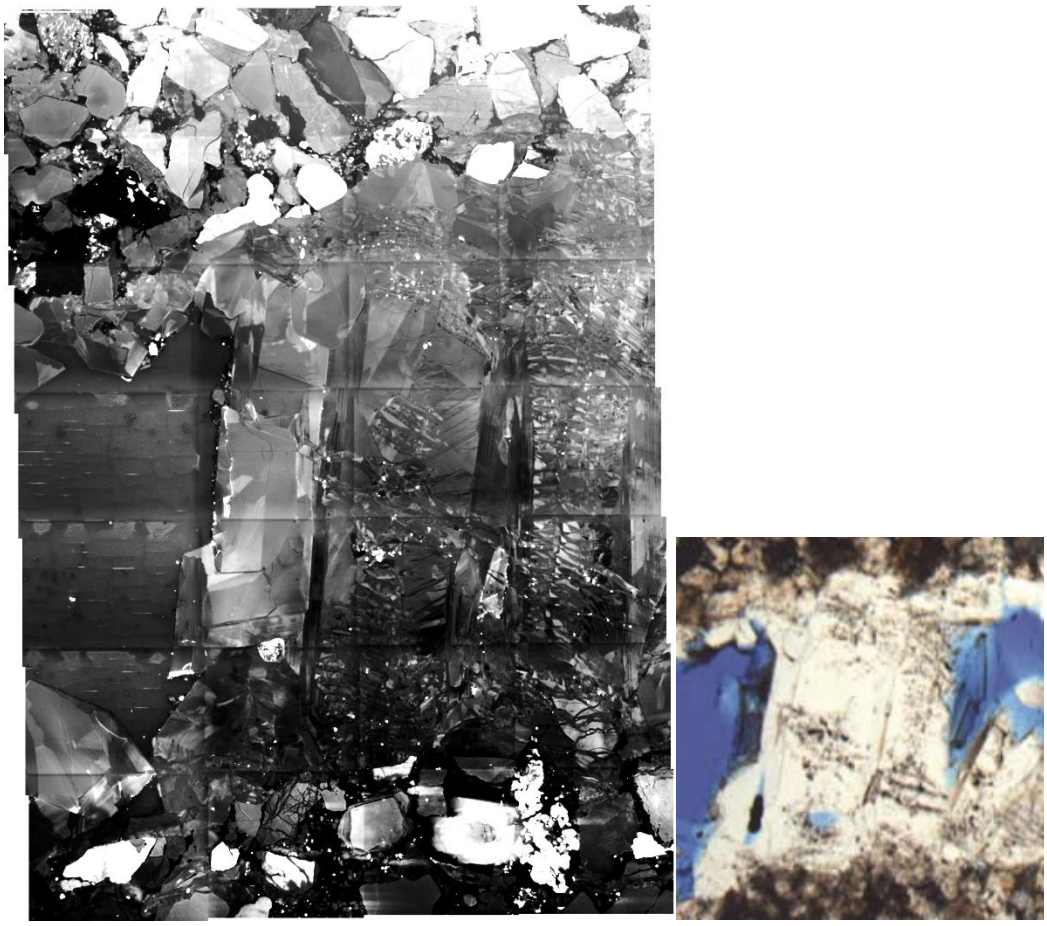

Figure B. 6: **Left**: panchromatic SEM-CL image of bridges 10 and 11 which are separated by euhedral lateral quartz cement. Crack-seal increments have complex texture and in some increments defining increment thickness can be challengaing. The apparent complexity can be original or a cutting angle effect. **Right:** Plane-polarized light image of the same bridges. Fluid inclusions trails are not very well organized. Euhedral quartz cement is observed to be inclusion-free.

Increment #	Measured Thickness (μm)	Measurement Angle (degrees)
1	4.2	90
2	9.3	87
3	13.2	80
4	6.4	111
5	6.0	90
6	18.2	105
7	12.3	101
8	13.6	98
9	20.0	86
10	10.6	105
11	11.3	102
12	16.2	90
13	14.4	92
14	20.4	90
15	7.7	115
16	11.8	101
17	6.4	69

Table B. 5: Bridge 10-11 crack-seal measurements.

Bridge F

Figure B. 7: Panchromatic SEM-CL image of bridge F.

Increment #	Measured Thickness (µm)	Measurement Angle (Degrees)
1	8.5	106
2	10.0	111
3	28.0	126
4	21.4	107
5	13.9	147
6	16.4	94
7	15.9	107
8	8.9	113
9	9.6	104
10	15.7	105
11	8.7	110
12	8.9	113
13	18.3	107
14	11.0	122
15	18.9	68
16	9.9	118
17	6.8	121
18	9.8	73
19	7.8	103
20	6.3	112

Table B. 6: Bridge F crack-seal measurements.

Bridge G

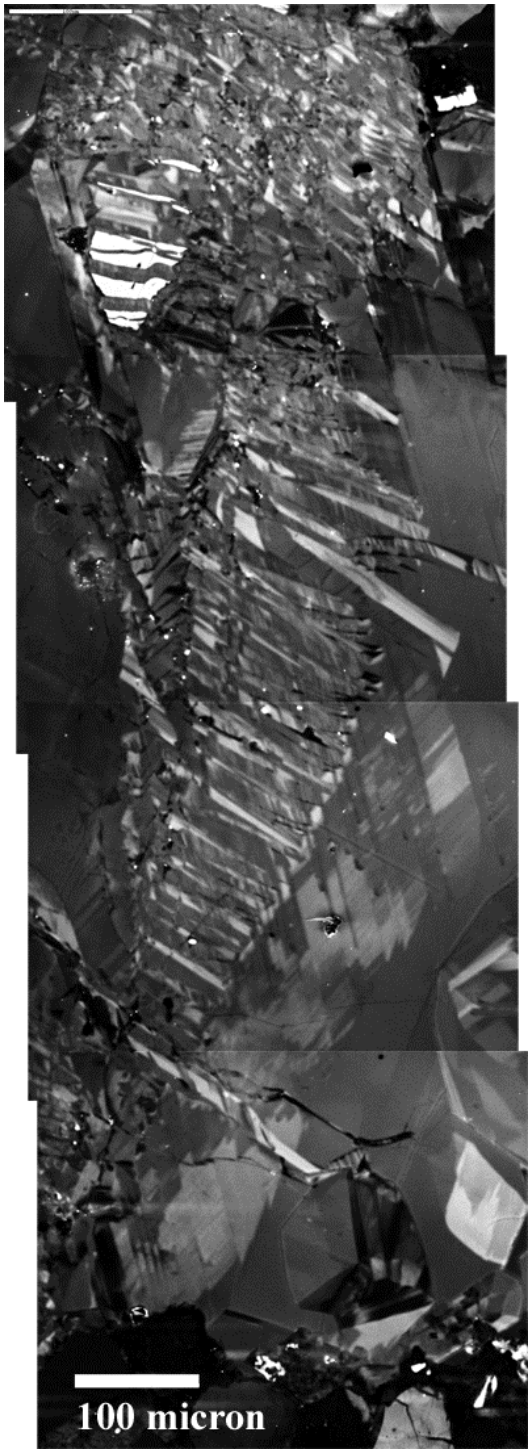

Figure B. 8: Panchromatic SEM-CL image of bridge G.

Increment #	Measured Thickness (µm)	Measurement Angle (Degrees)
1	10.4	81
2	7.5	117
3	8.1	111
4	7.4	107
5	6.6	87
6	3.5	90
7	12.4	90
8	10.8	103
9	20.2	103
10	14.8	89
11	13.3	88
12	12.1	111
13	21.1	94
14	8.6	94
15	13.6	85
16	12.2	93
17	19.1	99
18	9.6	73
19	10.8	111
20	17.2	116
21	15.8	62
22	10.4	118
23	5.1	63
24	12.5	81
25	7.4	95
26	5.3	108

Table B. 7: Bridge G crack-seal measurements.

Bridge H

Figure B. 9: Panchromatic SEM-CL image of bridge H.

Increment #	Measured Thickness (µm)	Measurement Angle (Degrees)
1	6.2	108
2	17.1	107
3	14.2	99
4	12.5	76
5	25.4	94
6	22.6	114
7	10.1	90
8	12.7	101
9	13.2	104
10	14.2	99
11	10.3	79
12	7.4	108
13	19.8	74
14	21.8	106
15	11.9	67
16	8.2	93
17	23.7	115
18	7.1	99
19	10.6	82
20	11.3	92
21	12.5	83
22	16.9	98
23	13.4	98
24	17.4	110
25	20.7	56
26	9.7	130
27	9.6	47
28	6.3	83
29	6.0	105
30	10.7	100
31	7.4	96
32	8.9	75
33	10.5	94

Table B. 8: Bridge H crack-seal measurements.

Bridge D

Figure B. 10: Panchromatic SEM-CL image of bridge D.

Increment #	Measured Thickness (µm)	Measurement Angle (Degrees)
1	7.9	103
2	14.3	89
3	7.3	107
4	10.8	115
5	14.1	110
6	10.8	119
7	18.1	62
8	12.7	98
9	10.8	94
10	13.1	112
11	13.5	107
12	17.3	56
13	9.5	126
14	13.4	105
15	8.3	112
16	15.4	108
17	15.5	113
18	14.3	112
19	24.0	106
20	14.0	76
21	15.5	104
22	13.8	74
23	13.3	96
24	9.2	79
25	22.3	104
26	10.1	104
27	10.6	73
28	8.4	107
29	20.5	76
30	16.9	112
31	21.9	115
32	10.1	104
33	11.4	117

Table B. 9: Bridge D crack-seal measurements.

Bridge 1

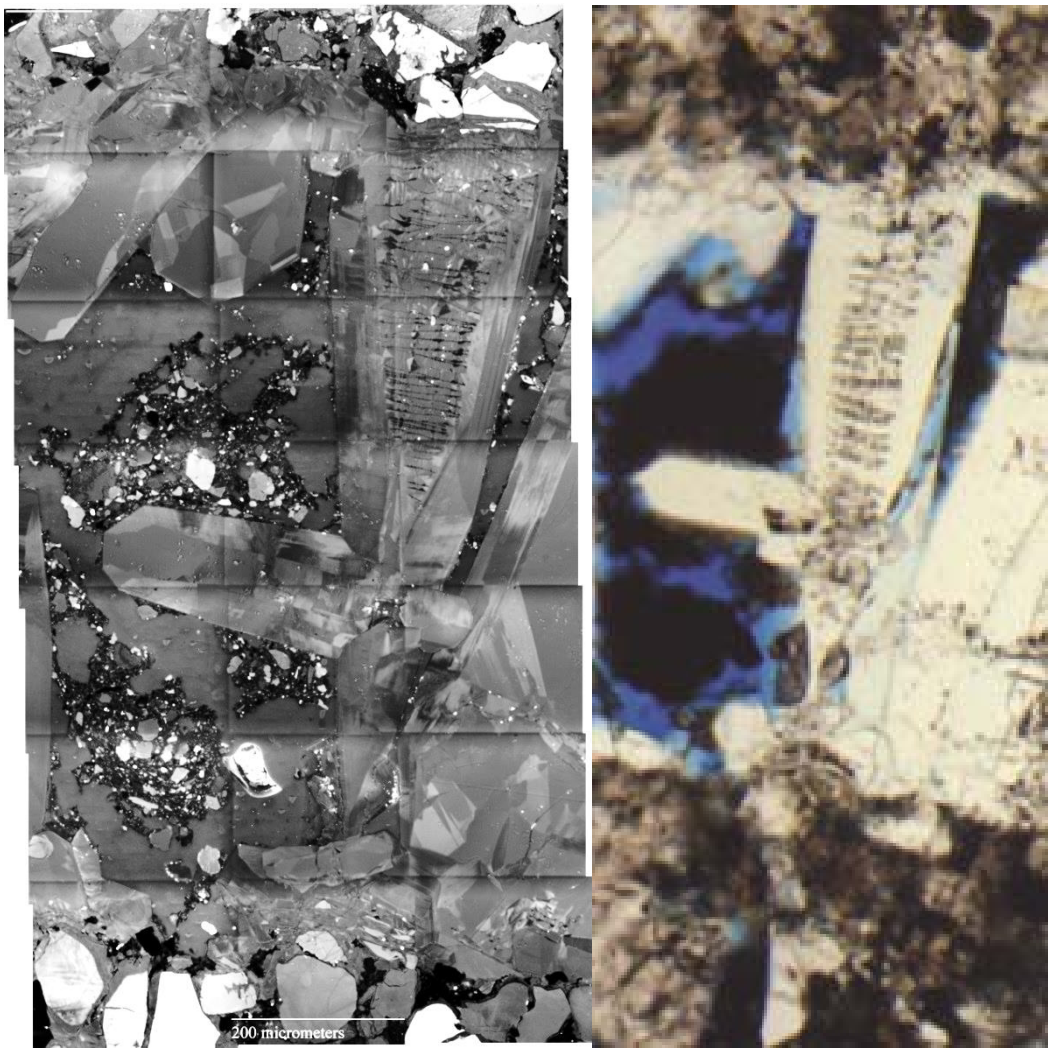

Figure B. 11: **Left**: panchromatic SEM-CL image of bridge 1, crack-seal increments are surrounded with euhedral lateral quartz cement. Note that only half of the bridge contains crack-seal texture most likely because the thin section cuts this bridge at an oblique angle. **Right:** Plane-polorized light image of the same bridge with linear fluid inclusion trails along crack-seal increments. Fracture porosity can be seen in blue. The dark black patches within the fracture are artifacts produced by the thin section grinding mud.

Increment #	Measured Thickness (µm)	Measurement Angle (degrees)
1	9.7	111
2	3.8	90
3	12.5	104
4	15.9	70
5	15.5	106
6	13.0	98
7	15.6	102
8	17.0	86
9	18.6	114
10	22.0	97
11	11.5	93
12	9.8	96
13	21.5	81
14	9.3	103
15	11.0	103
16	8.3	90
17	19.2	97

Table B. 10: Bridge 1 crack-seal measurements.

Bridge C

Figure B. 12: Panchromatic SEM-CL image of bridge C.

Increment #	Measured Thickness (µm)	Measurement Angle (Degrees)
1	11.0	126
2	7.9	90
3	10.9	100
4	11.5	104
5	20.6	118
6	7.7	115
7	7.5	83
8	5.6	85
9	16.5	106
10	12.4	110
11	22.9	108
12	19.4	107
13	17.0	99
14	13.7	100
15	13.1	94
16	10.9	110
17	21.5	85
18	8.4	87
19	15.2	113
20	10.9	78
21	11.2	85
22	19.1	89
23	12.8	80
24	11.7	95
25	11.8	81
26	3.5	113
27	9.2	114
28	10.9	80
29	13.0	111
30	9.4	81
31	6.1	81
32	5.2	100
33	4.2	63
34	5.3	105
35	3.4	124

Table B. 11: Bridge C crack-seal measurements.

Bridge E

Figure B. 13: Panchromatic SEM-CL image of bridge E.

Increment #	Measured Thickness (μm)	Measurement Angle (Degrees)
1	15.7	102
2	13.8	100
3	10.7	109
4	13.7	105
5	11.0	127
6	11.7	73
7	10.5	90
8	10.3	72
9	6.4	81
10	7.4	71
11	8.8	72
12	8.6	69
13	12.3	75
14	5.2	94
15	12.2	114
16	9.1	90
17	10.9	84
18	10.9	107
19	8.6	76
20	20.9	116
21	18.4	117
22	14.8	75
23	4.7	63

Table B. 12: Bridge E crack-seal measurements.

SFOT-1-10,108.3- FRACTURE 2

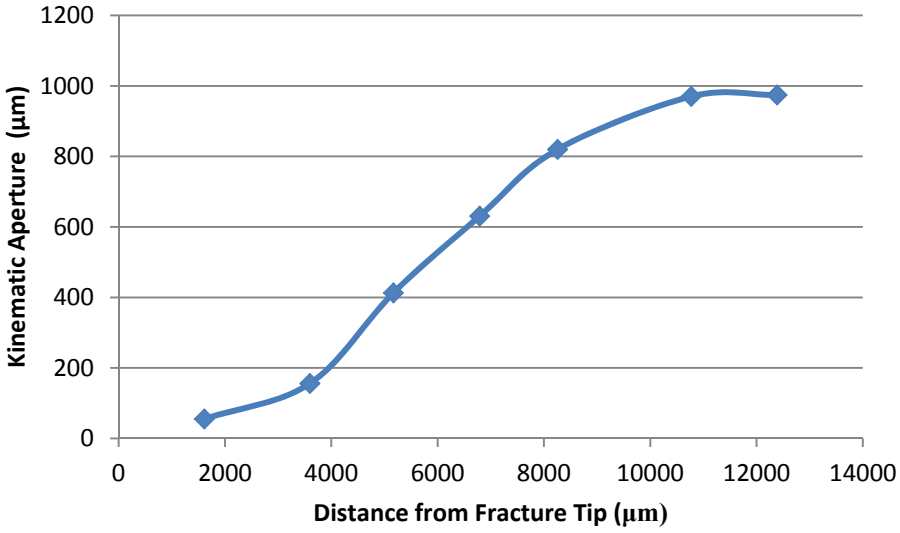

Figure B. 14: Fracture 2 kinematic aperture profile from examined bridges.

Summary of Bridge Measurements

Relative Distance	Bridge #	Distance From Tip (µm)	Kinematic Aperture (µm)	Average Increment Thickness (µm)	Standard Error in Increment Thickness (+/-)	Estimated Number of increments
1	5	1610.1	55.19	3.39	0.85	16
2	3	3597.7	155.92	5.43	0.35	29
3	2	5169.4	412.98	6.50	0.71	64
4	6	6790.9	630.58	6.48	0.70	97
5	B	8257.1	819.97	7.85	0.55	105
6	J	10771.4	970.00	11.71	0.97	83
7	I	12386.1	974.28	10.36	0.66	91

Table B. 13: Summary of cement bridge measurements in Fracture 2- SFOT-1-10,108.3'.

SFOT-1-10,108.5- Fracture 2 Bridge Images and Measurements

Note: Bridges images and measurements are in ascending order according to their distance from the fracture. Measurement angles are in degrees (0 = horizontal).

Bridge 5

Figure B. 15: Panchromatic SEM-CL image of bridge 5. The blurriness around the white quartz grain at the bottom is an imaging artifact caused by high luminescence.

Increment #	Measured Thickness (μm)	Measurement Angle (degrees)
1	2.6	75
2	1.3	80
3	1.4	90
4	1.5	90
5	2.1	107
6	2.7	103
7	1.6	101
8	5.3	66
9	3.9	113
10	9.3	118
11	10.2	87
12	1.2	90
13	0.9	90

Table B. 14: Bridge 5 crack-seal measurements.

Bridge 3

Figure B. 16: Panchromatic SEM-CL image of bridge 3. A quartz grain is split in half by two crack-seal increments with clear cross-cutting relationship with older intragranular fractures.

Increment #	Measured Thickness (µm)	Measurement Angle (degrees)
1	4.4	90
2	5.0	78
3	6.6	87
4	3.5	84
5	4.9	82
6	7.4	82
7	6.1	77
8	5.9	90
9	5.0	102
10	4.4	135
11	6.4	151

Table B. 15: Bridge 3 crack-seal measurements.

Bridge 2

Figure B. 17: Panchromatic SEM-CL image of bridge 2. Two generations of fractures have affected the embedded quartz grain: older intragranular microfractures and younger crack-seal fracture increments that are responsible for the observed fragmentation of the grain.

Increment #	Measured Thickness (µm)	Measurement Angle (degrees)
1	2.8	90
2	6.7	78
3	6.5	86
4	8.9	90
5	10.0	79
6	8.4	87
7	5.2	100
8	13.1	74
9	2.7	121
10	7.7	104
11	7.9	93
12	5.3	105
13	5.2	80
14	3.8	76
15	6.9	110
16	2.8	90

Table B. 16: Bridge 2 crack-seal measurements.

Bridge 6

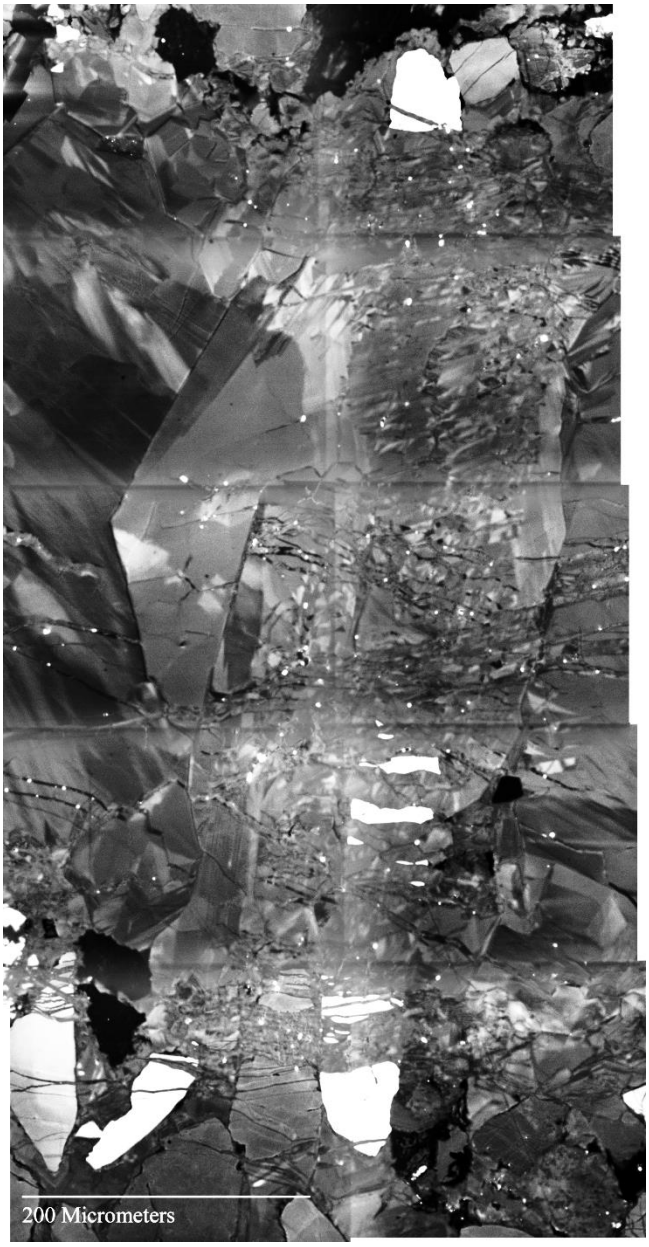

Figure B. 18: Panchromatic SEM-CL image of bridge 6. The fracture splits a white quartz grain with one half of the grain located in the upper fracture wall and the other in the lower fracture wall; some fragments are displaced within the crack-seal bridge. Late crack-seal can be observed cutting euhedral quartz cement on both sides of the bridge.

Increment #	Measured Thickness (µm)	Measurement Angle (degrees)
1	4.5	113
2	6.6	108
3	3.5	96
4	9.1	92
5	2.1	90
6	5.7	101
7	5.9	87
8	4.7	117
9	5.3	101
10	6.7	69
11	3.2	103
12	6.1	114
13	5.6	112
14	15.9	123
15	7.2	119
16	8.9	79
17	9.1	92

Table B. 17: Bridge 6 crack-seal measurements.

Bridge B

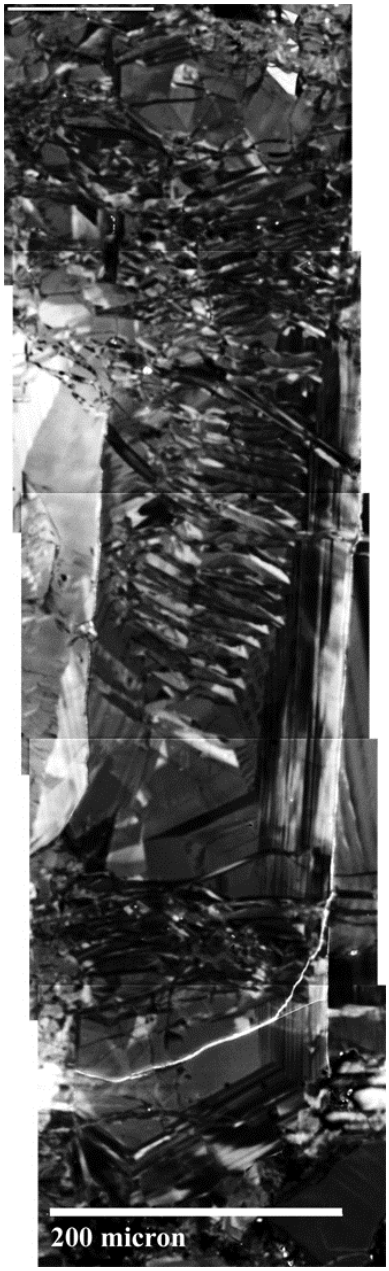

Figure B. 19: Panchromatic SEM-CL image of bridge B.

Increment #	Measured Thickness (µm)	Measurement Angle (Degrees)
1	5.8	73
2	4.1	70
3	6.6	65
4	10.3	62
5	11.6	111
6	12.8	73
7	10.2	112
8	10.8	69
9	5.9	90
10	8.7	95
11	8.1	133
12	9.6	109
13	5.8	107
14	7.7	85
15	8.7	127
16	8.1	83
17	5.4	75
18	6.6	72
19	5.4	75
20	4.5	90

Table B. 18: Bridge B crack-seal measurements.

Bridge J

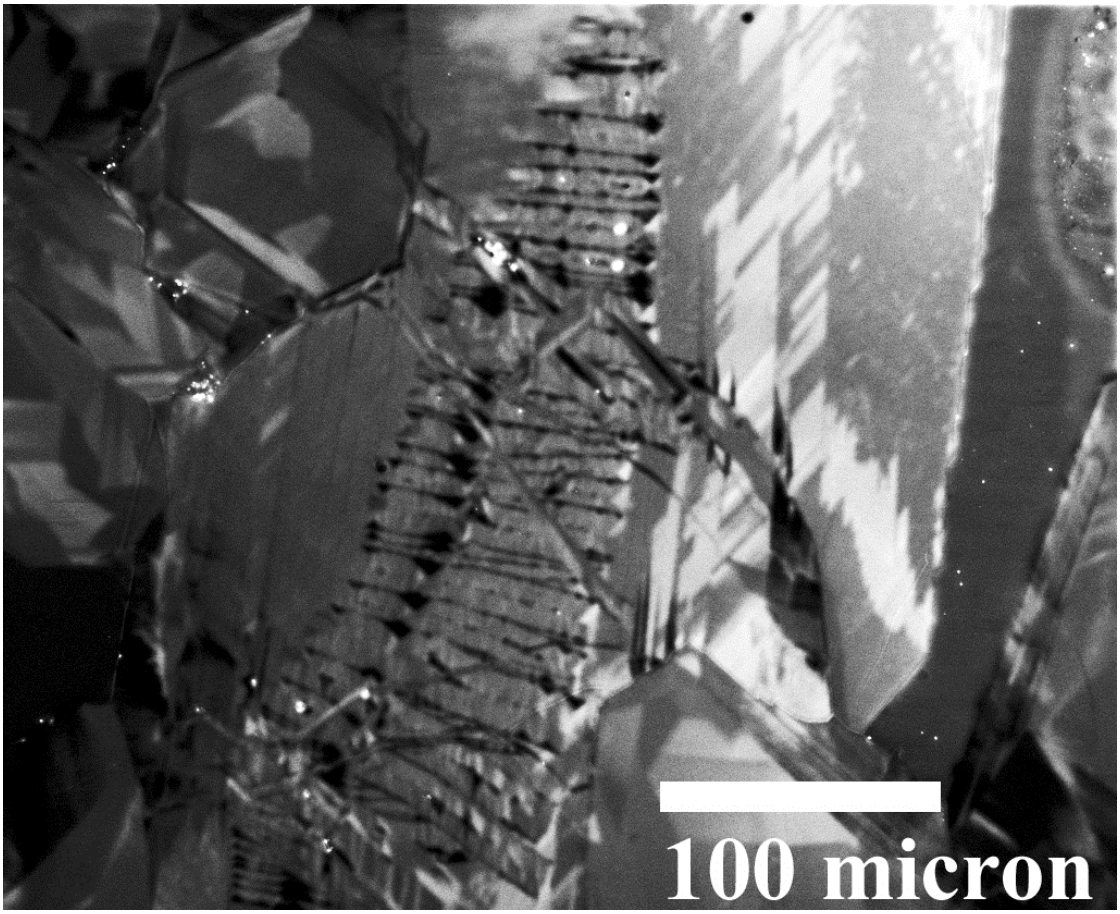

Figure B. 20: Panchromatic SEM-CL image of bridge J. Youngest crack-seal increments cut older crack-seal obliquely.

Increment #	Measured Thickness (µm)	Measurement Angle (Degrees)
1	9.7	90
2	18.3	89
3	12.6	99
4	9.0	97
5	14.8	90
6	9.5	99
7	13.1	120
8	12.5	94
9	15.8	100
10	13.8	106
11	11.8	107
12	19.3	-65
13	15.1	125
14	14.8	120
15	6.6	130
16	7.1	61
17	3.5	117
18	7.0	124
19	8.2	90

Table B. 19: Bridge J crack-seal measurements.

Bridge I

Figure B. 21: Panchromatic SEM-CL image of bridge I.

Increment #	Measured Thickness (μm)	Measurement Angle (Degrees)
1	7.1	119
2	5.3	73
3	6.9	106
4	9.1	70
5	9.2	68
6	9.3	92
7	5.1	113
8	15.1	116
9	9.6	-63
10	9.9	116
11	18.3	-63
12	13.6	117
13	7.0	93
14	15.5	108
15	9.6	111
16	14.8	120
17	13.3	105
18	13.4	107
19	12.5	-76
20	6.2	108
21	7.0	109
22	8.1	107
23	9.5	102
24	9.5	99
25	20.2	113
26	11.3	112
27	9.3	90
28	5.4	90
29	6.6	87
30	11.0	58
31	11.7	105
32	10.8	103

Table B. 20: Bridge I crack-seal measurements.

Sample Depth: 10,106’

Formation: Travis Peak

Fracture sampling orientation: Length (i.e.: perpendicular to core)

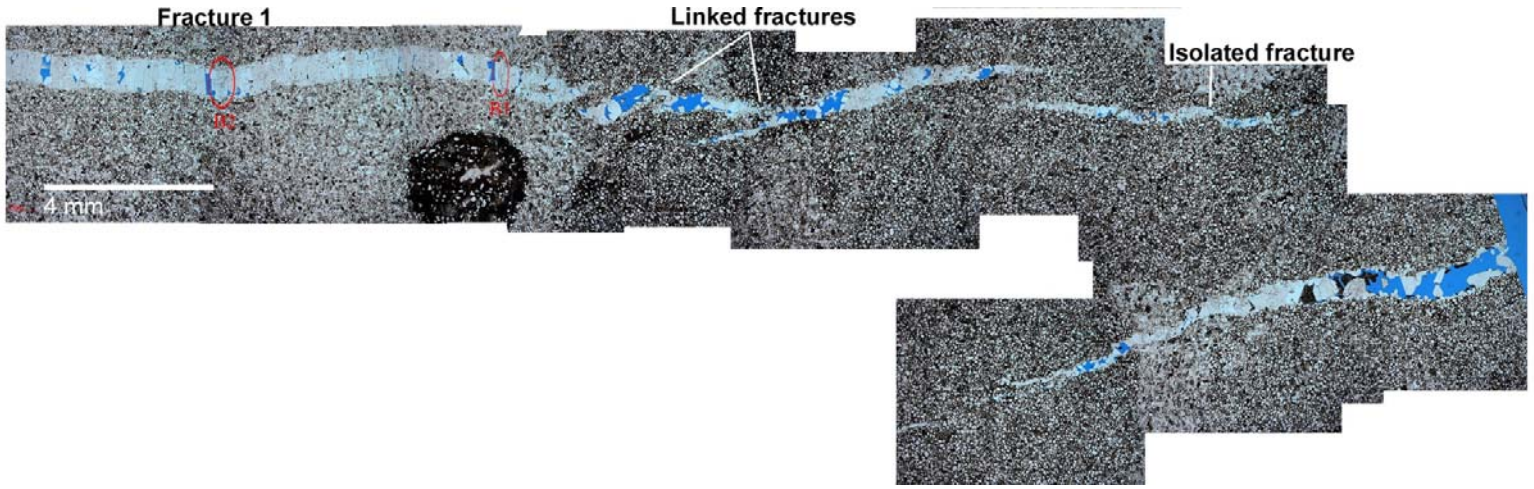

Figure B. 22: A thin section view under plane polarized light microscope of en-echelon fractures. Fracture 1 appears to be affected by its proximity to the three linked fractures but has not linked with them. Fracture 1 and the isolated fracture have very low porosity while the linked fractures have good porosity. Almost all the fracture fill is quartz with minute amount of bitumen. Labeled quartz bridges (B#) were imaged using SEM-Cl.

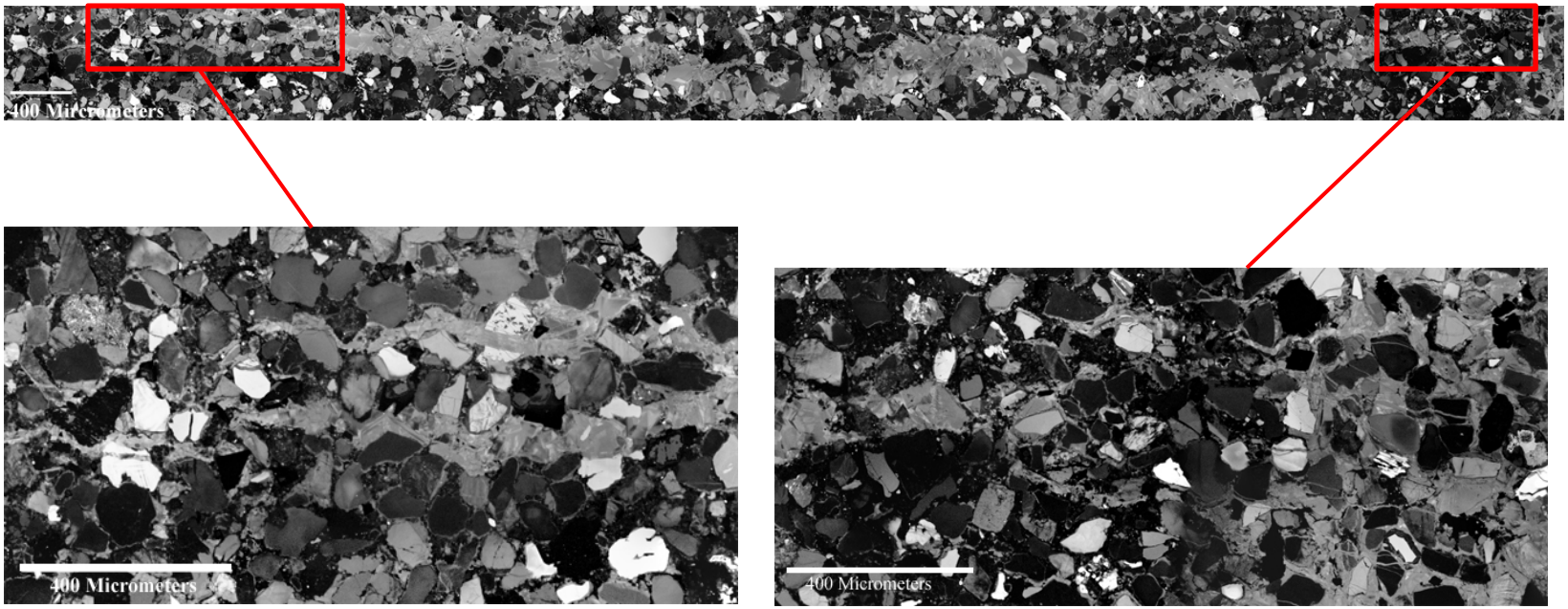

Figure B. 23: SEM-Cl image (blue filter) of the isolated fracture at 10,106'. At the fracture tips, it branches and dissipates into many smaller microfractures before terminating. The dominant type of cement in the middle of the fracture is euhedral quartz cement with few crack-seal bridges present. However, crack-seal quartz is more dominant near the tips of the fracture.

10,106'-FRACTURE 1- BRIDGE IMAGES AND MEASUREMENTS

Bridge 1

Figure B. 24: Panchromatic SEM-CL image of bridge 1 of fracture 1. A smaller partially crack-seal bridge can be observed to the right of bridge 1. The crack-seal texture covers most of the bridge but euhedral cement is present at the upper side; thin section cutting effect is suspected to be the reason.

Increment #	Measured Thickness (μm)	Measurement Angle (degrees)
1	4.4	95
2	4.5	61
3	5.8	86
4	9.4	106
5	5.5	82
6	5.1	90
7	7.2	93
8	7.6	85
9	7.2	90
10	8.0	90
11	9.9	82
12	5.5	79
13	7.3	81
14	5.8	83
15	9.8	92
16	11.2	90
17	9.0	90
18	7.2	90
19	8.0	90

Table B. 21: Bridge 1 crack-seal measurements.

Increment Average Thickness (μm)	Measured Kinematic Aperture (μm)	Estimated Number of Increments
8.3	729.8	88

Table B. 22: Key calculated parameters for Bridge 1.

Increment #	Measured Thickness (µm)	Measurement Angle
1	7.6	92.7
2	7.2	90.0
3	13.8	94.5
4	9.5	96.6
5	7.2	92.9
6	10.1	92.0
7	10.5	88.0
8	5.1	85.9
9	8.5	102.3
10	4.8	81.3

Table B. 23: Thickness measurements for the partial crack-seal bridge to the right of bridge 1.

Increment Average Thickness (µm)	Measured Kinematic Aperture (µm)	Estimated Number of Increments
8.4	729.8	88

Table B. 24: Key parameters for the partial crack-seal bridge to the right of bridge 1. Note that the estimated number of increments is similar to that of bridge one validating the increment estimating method.

Sample Depth: 10,106.7-10,107’

Formation: Travis Peak
Fracture sampling orientation: Height (i.e.: parallel to core)

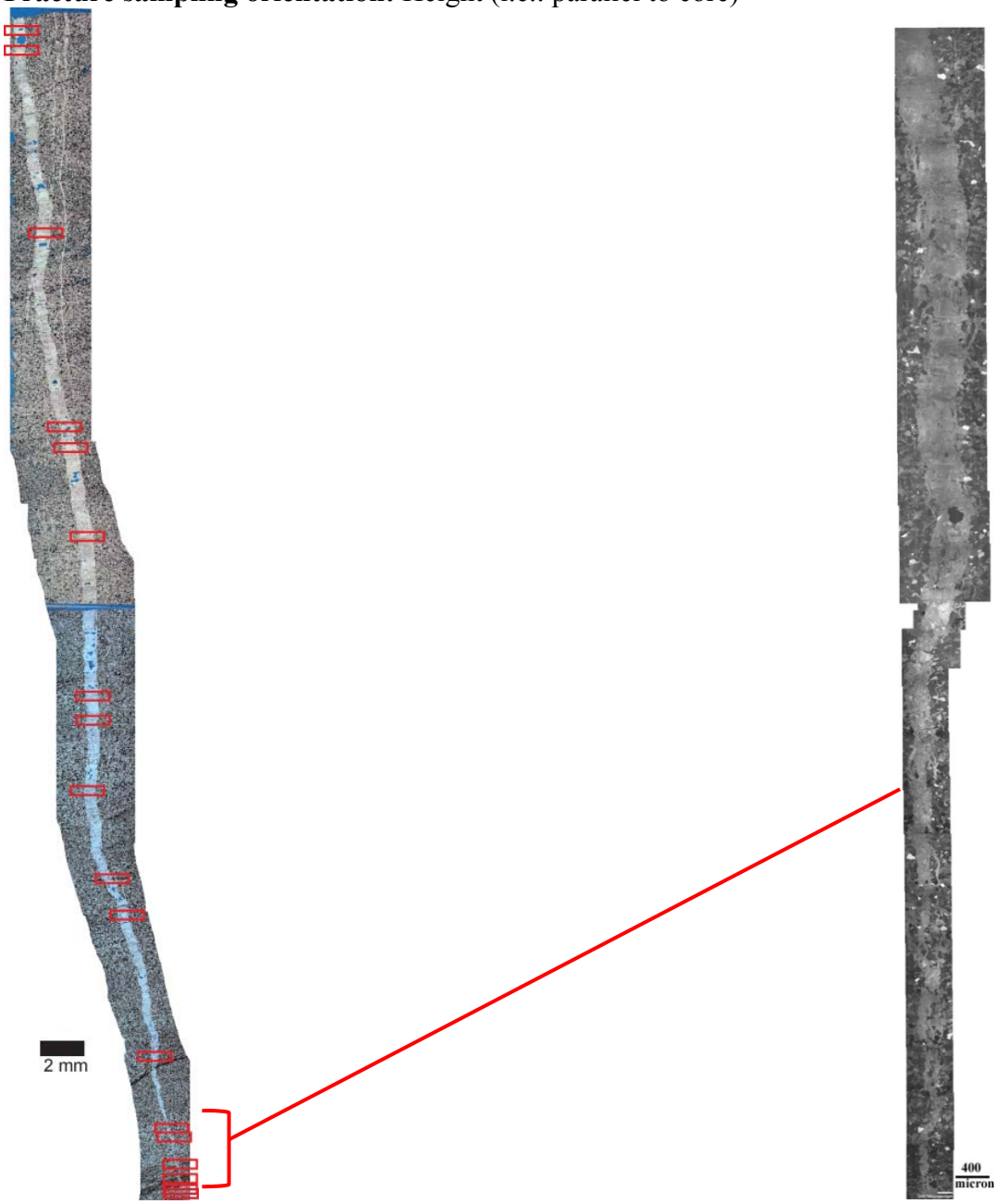

Figure B. 25: **Left:** Plane polarized images of a continuous fracture sample (SFOT-1-10106.7-10107). Fracture porosity is almost entirely occluded by quartz cement. **Right:** Blue filter SEM-CL image of the fracture tip showing segmentation increases near the tip.

SFOT-1-10,106.7-10107

Summary of Bridge Measurements

Relative Distance	Bridge	Distance From Tip (μm)	Kinematic Aperture (μm)	Average Increment Thickness (μm)	Standard Error in Increment Thickness (+/-)	Estimated Number of increments
1	10107-b7	146.7	62.67	2.77	0.10	23
2	10107-b6	481.2	63.99	2.82	0.79	23
3	10107-b2	961.2	99.79	3.21	0.38	31
4	10107-b1	2433.8	105.36	2.76	0.31	38
5	10107-tip bridge 3	4748.9	124.90	3.87	0.32	32
6	10107-b3	5327.2	156.19	4.16	0.31	38
7	10107-b4	9175.1	236.15	3.77	0.35	63
8	10107-tip bridge1	9760.2	445.85	6.97	0.59	64
9	10107-b5	11656.9	276.13	3.96	0.34	70
10	10107-b8	18211.4	488.93	6.49	0.62	75
11	10107-b9	21036.2	592.77	8.48	0.78	70
12	10107-b10	26359.9	679.10	8.20	0.73	83
13	10107 tip bridge 2	30369.5	745.09	9.62	0.70	77
14	10107-b11	31784.8	790.45	9.80	0.62	81
15	10106.85 b6	41865.5	779.7	11.30	0.59	69
16	10106.85 b5	47321.0	919.71	9.64	0.43	95
17	10106.85 b1	48546.7	806.47	9.21	0.51	80
18	10106.85 b4	60375.1	822.07	9.64	0.98	85
19	10106.85 b3	71994.0	668.58	10.64	0.87	63
20	10106.85 b2	73511.0	710.73	9.57	1.29	74

Table B. 25: Summary of cement bridge measurements in Fracture SFOT-1-10,106.7-10,107'.

SFOT-1-10,106.7-10107' Bridge Images and Measurements

Note: Bridges images and measurements are in ascending order according to their distance from the fracture. Measurement angles are in degrees (0 = vertical).

10107'-Bridge 7

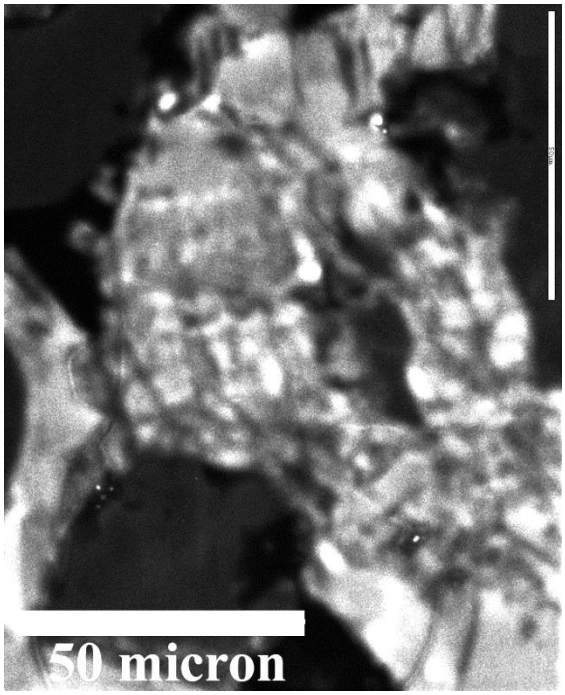

Figure B. 26: Panchromatic SEM-CL image of 10107-Bridge 7.

Increment #	Measured Thickness (µm)	Measurement Angle
1	2.7	80
2	2.6	49
3	3.0	79

Table B. 26: 10107-Bridge 7 crack-seal measurements.

10107'-Bridge 6

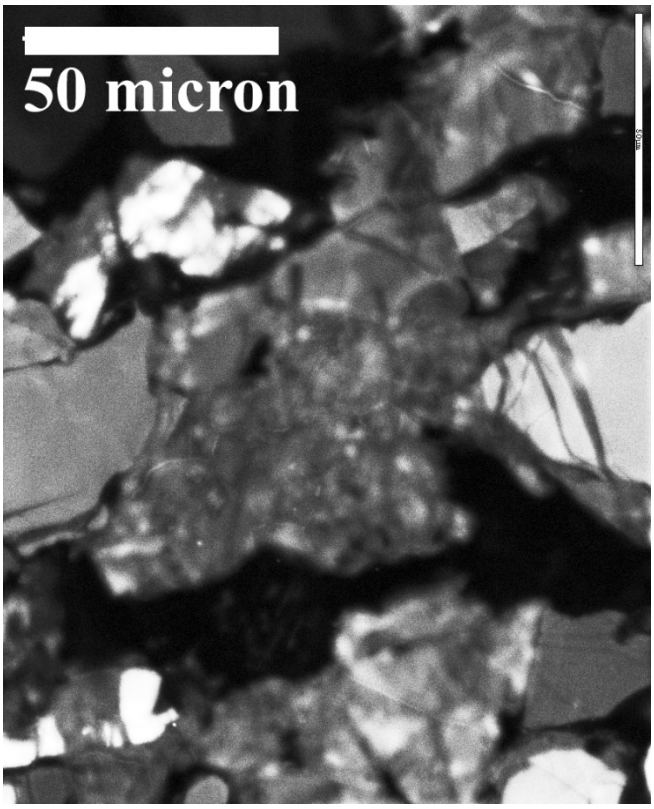

Figure B. 27 Panchromatic SEM-CL image of 10107-Bridge 6.

Increment #	Measured Thickness (µm)	Measurement Angle
1	3.3	65
2	1.4	90
3	1.8	75
4	4.9	107

Table B. 27: 10107-Bridge 6 crack-seal measurements.

10107'-Bridge 2

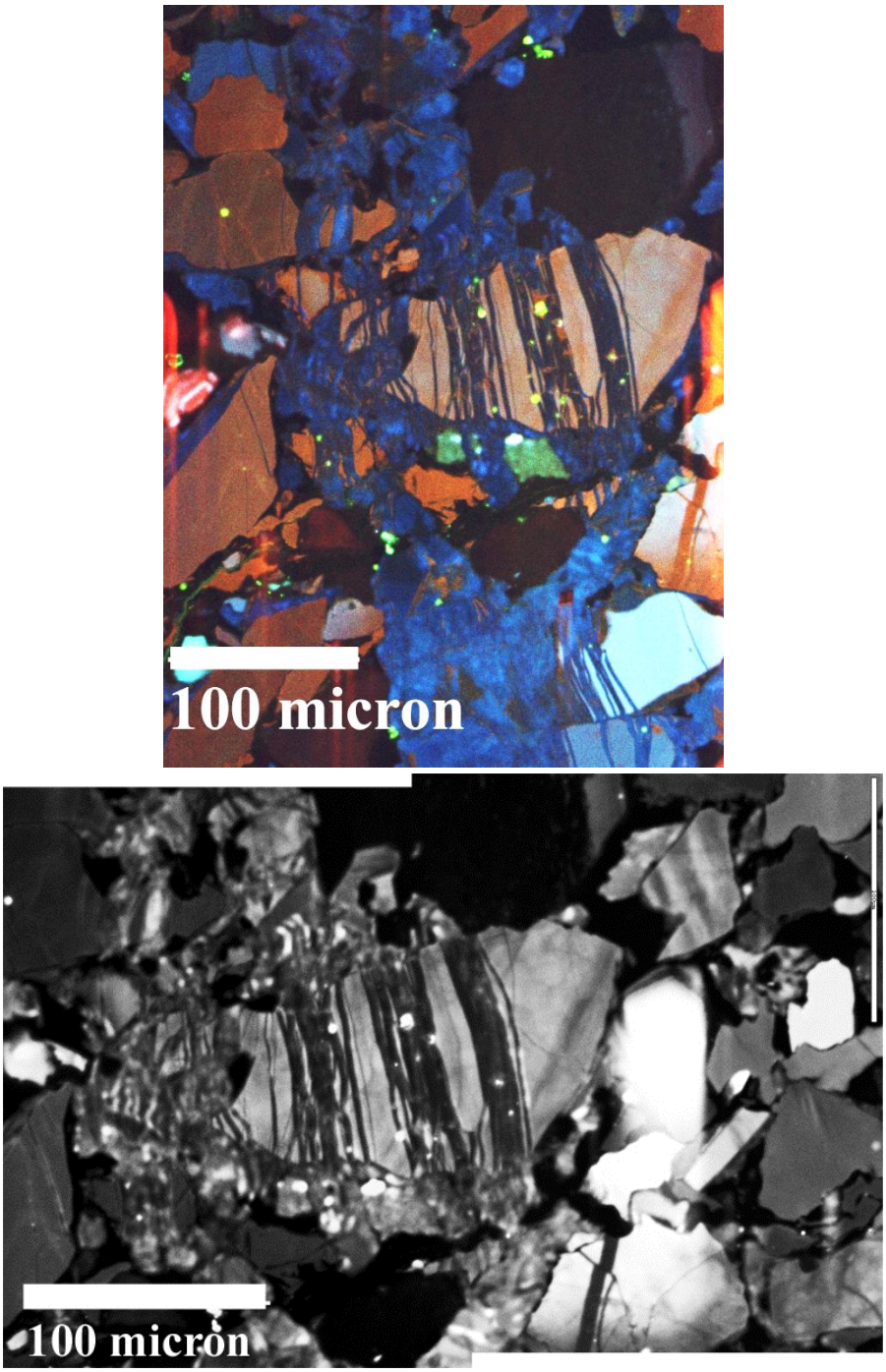

Figure B. 28: **Top:** Color Mosiac SEM-CL image of 10107-Bridge 2. **Bottom:** Panchromatic SEM-CL image of the same bridge.

Increment #	Measured Thickness (μm)	Measurement Angle
1	1.9	83
2	6.1	81
3	4.2	81
4	3.5	98
5	2.8	85
6	3.0	90
7	2.8	85
8	2.3	90
9	2.6	63
10	2.8	81

Table B. 28: 10107-Bridge 2 crack-seal measurements.

10107'-Bridge 1

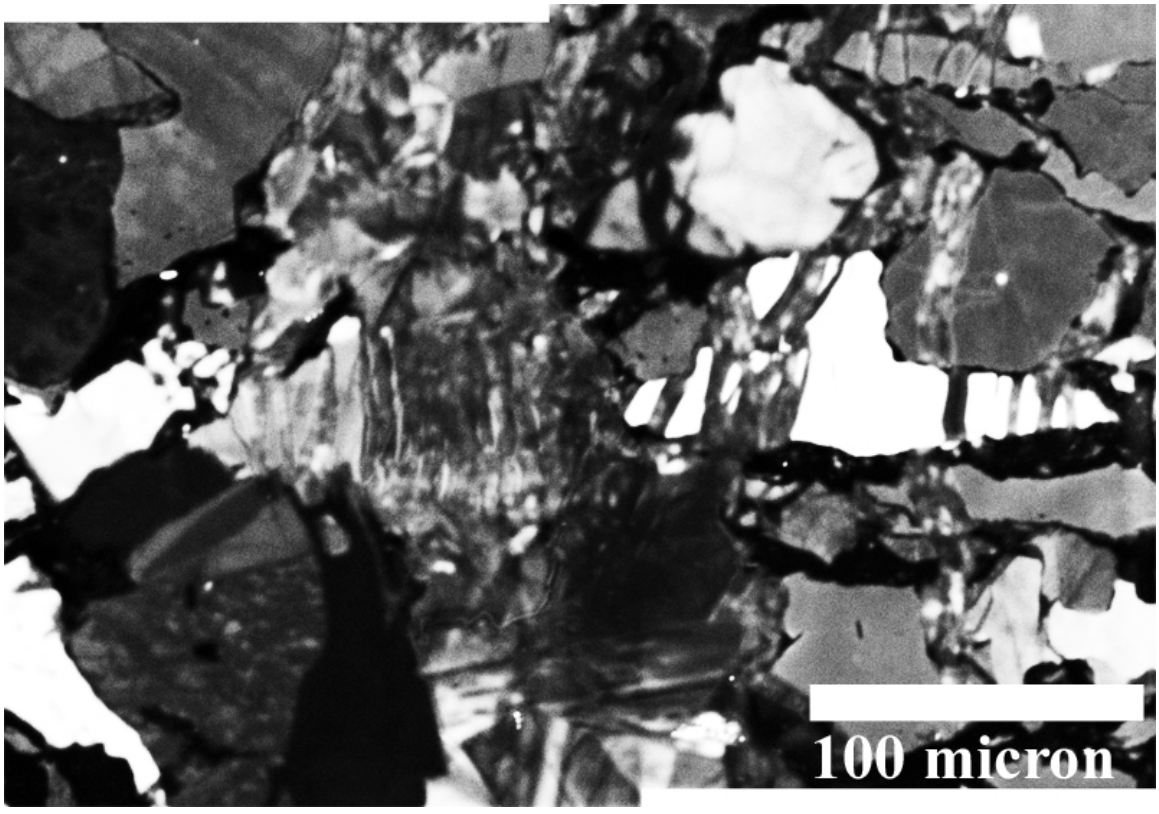

Figure B. 29: Panchromatic SEM-CL image of 10107-Bridge 1.

Increment #	Measured Thickness (µm)	Measurement Angle
1	3.8	112
2	1.4	104
3	2.4	90
4	5.6	112
5	3.8	90
6	3.1	90
7	2.3	63
8	2.8	90
9	2.4	90
10	3.9	117
11	3.1	90
12	2.5	82
13	1.2	79
14	1.7	74
15	1.3	68

Table B. 29: 10107-Bridge 1 crack-seal measurements.

10107'-Tip Bridge 3

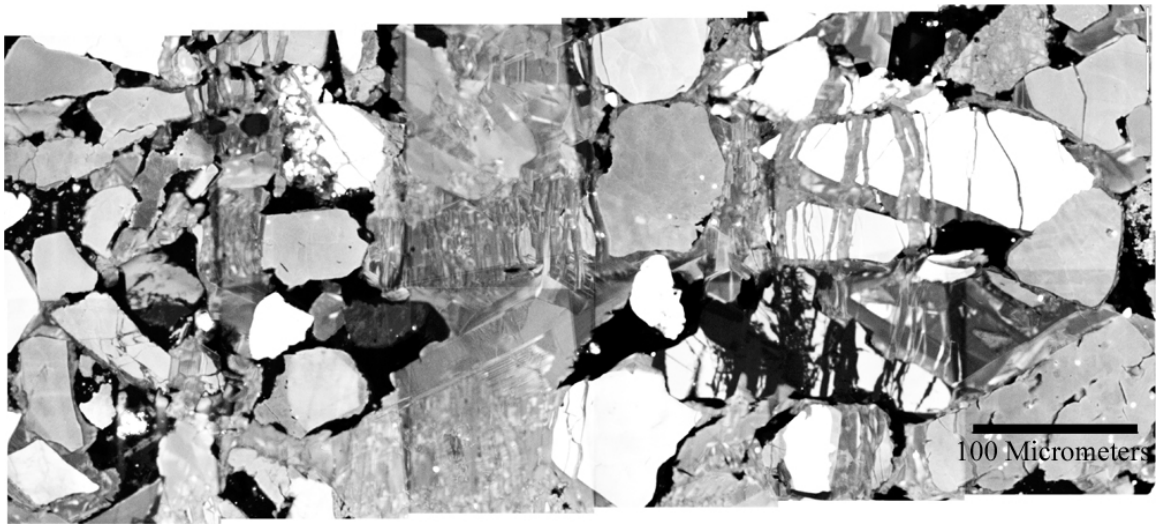

Figure B. 30: Panchromatic SEM-CL image of 10107-Tip bridge 3.

Increment #	Measured Thickness (µm)	Measurement Angle
1	3.0	32
2	3.7	145
3	4.7	20
4	3.2	159
5	3.1	42
6	5.1	108
7	5.1	90
8	3.5	90
9	3.0	90
10	6.5	84
11	3.3	90
12	2.6	90
13	3.5	94

Table B. 30: 10107-Tip Bridge 3 crack-seal measurements.

10107'-Bridge 3

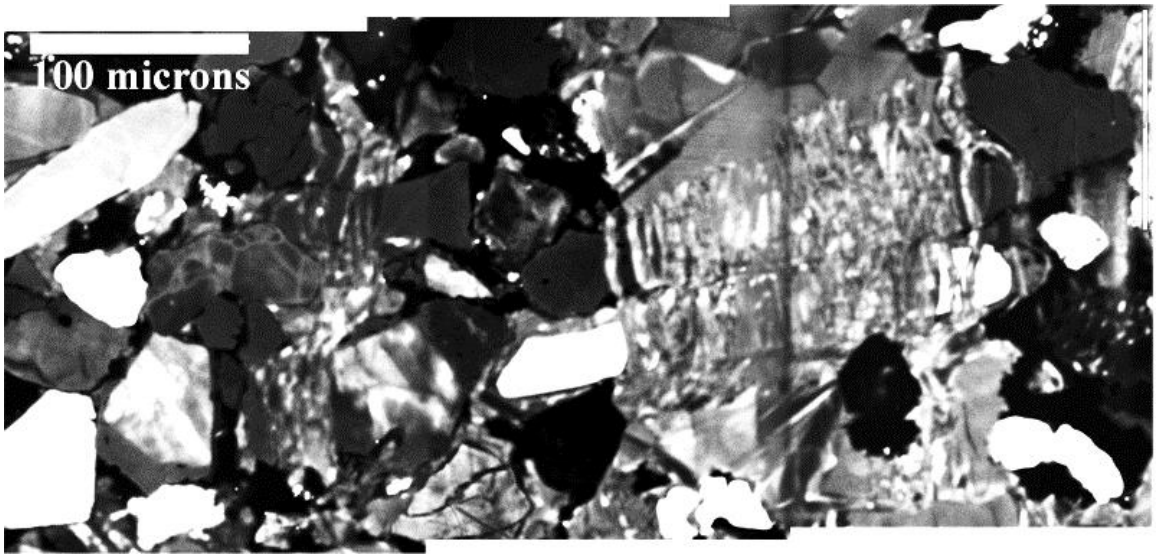

Figure B. 31: Panchromatic SEM-CL image of 10107- Bridge 3.

Increment #	Measured Thickness (μm)	Measurement Angle
1	4.5	99
2	4.5	81
3	3.7	83
4	3.8	79
5	5.9	83
6	5.2	77
7	3.1	81
8	3.6	79
9	4.7	84
10	2.7	59

Table B. 31: 10107- Bridge 3 crack-seal measurements.

10107'-Bridge 4

Figure B. 32: Panchromatic SEM-CL image of 10107-Bridge 4.

Increment #	Measured Thickness (µm)	Measurement Angle
1	3.6	75
2	3.4	74
3	5.2	80
4	2.3	90
5	1.9	76
6	2.6	90
7	3.3	90
8	4.9	82
9	2.8	95
10	2.1	90
11	4.5	78
12	3.7	120
13	4.9	90
14	6.7	92

Table B. 32: 10107- Bridge 4 crack-seal measurements.

10107'-Tip Bridge

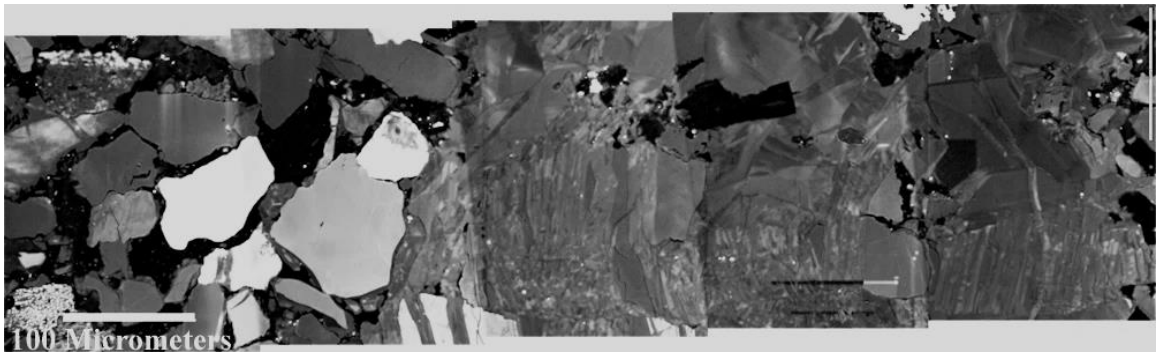

Figure B. 33: Panchromatic SEM-CL image of 10107-Tip bridge.

Increment #	Measured Thickness (µm)	Measurement Angle
1	6.6	80
2	11.2	84
3	11.7	82
4	5.2	100
5	6.3	107
6	10.3	106
7	7.3	79
8	6.4	103
9	5.4	102
10	3.4	74
11	9.1	96
12	5.7	117
13	7.7	65
14	4.2	81
15	3.7	97
16	6.9	90
17	7.4	88

Table B. 33: 10107-Tip bridge crack-seal measurements.

10107'-Bridge 5

Figure B. 34: Panchromatic SEM-CL image of 10107-Bridge 5.

Increment #	Measured Thickness (µm)	Measurement Angle
1	2.4	79
2	2.6	100
3	3.1	81
4	3.1	81
5	1.7	74
6	3.6	101
7	2.3	84
8	3.3	78
9	3.2	73
10	4.2	90
11	2.2	72
12	5.0	78
13	4.9	82
14	3.6	73
15	4.3	76
16	3.5	90
17	8.9	99
18	5.6	83
19	5.8	104
20	4.7	70
21	3.6	105
22	5.6	83

Table B. 34: 10107-Bridge 5 crack-seal measurements.

10107'-Bridge 8

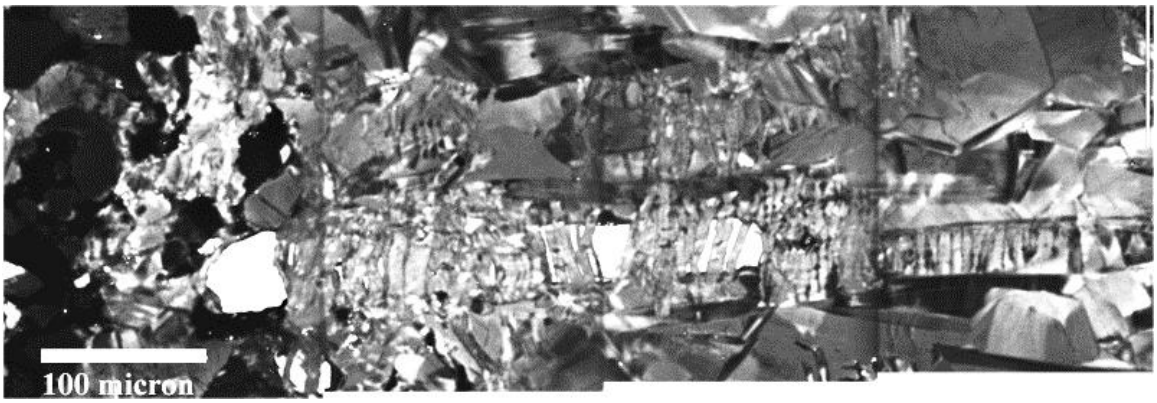

Figure B. 35: Panchromatic SEM-CL image of 10107-Bridge 8.

Increment #	Measured Thickness (µm)	Measurement Angle
1	5.4	88
2	7.0	84
3	4.4	90
4	6.3	92
5	8.1	90
6	6.3	86
7	5.2	82
8	6.0	90
9	4.4	90
10	3.3	78
11	8.0	83
12	7.0	84
13	12.6	93
14	10.9	89
15	4.3	103
16	4.6	108

Table B. 35: 10107-Bridge 8 crack-seal measurements.

10107'-Bridge 9

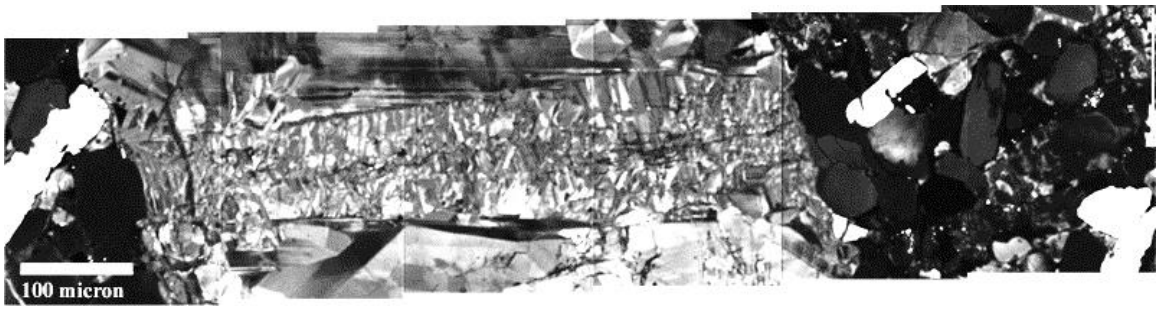

Figure B. 36: Panchromatic SEM-CL image of 10107-Bridge 9.

Increment #	Measured Thickness (µm)	Measurement Angle
1	5.4	88
2	7.0	84
3	4.4	90
4	6.3	92
5	8.1	90
6	6.3	86
7	5.2	82
8	6.0	90
9	4.4	90
10	3.3	78
11	8.0	83
12	7.0	84
13	12.6	93
14	10.9	89
15	4.3	103
16	4.6	108

Table B. 36: 10107-Bridge 9 crack-seal measurements.

10107'-Bridge 10

Figure B. 37: Panchromatic SEM-CL image of 10107-Bridge 10.

Increment #	Measured Thickness (μm)	Measurement Angle
1	5.6	85
2	2.6	90
3	8.1	103
4	9.3	87
5	10.9	80
6	9.7	73
7	7.7	104
8	8.2	74
9	7.0	98
10	13.5	74
11	4.7	90
12	9.1	75
13	10.2	74
14	8.2	47

Table B. 37: 10107-Bridge 10 crack-seal measurements.

10107'-Tip Bridge 2

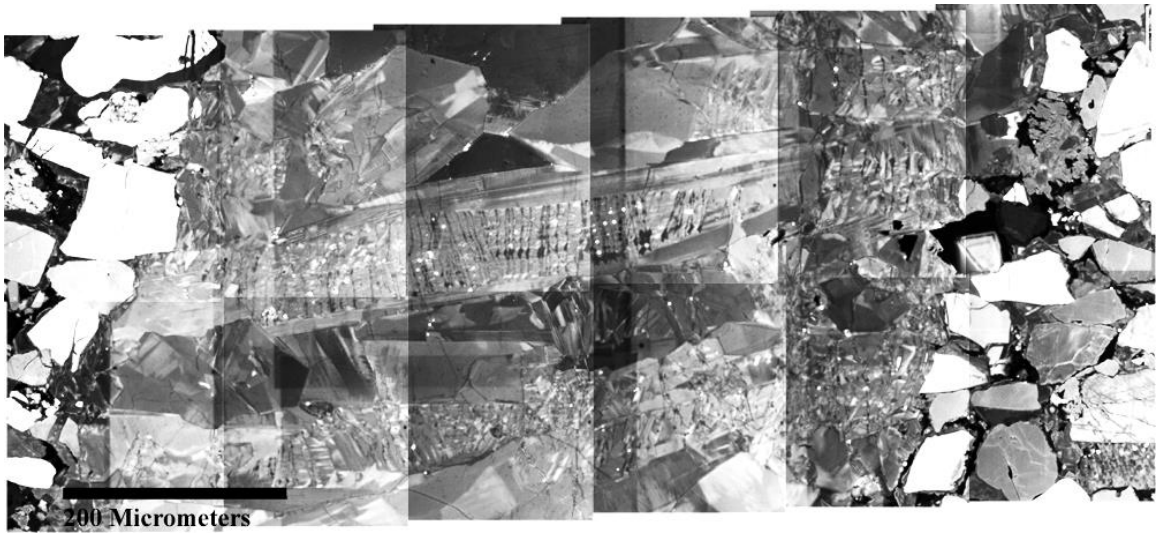

Figure B. 38: Panchromatic SEM-CL image of 10,107-Tip bridge 2.

Increment #	Measured Thickness (µm)	Measurement Angle
1	3.7	90
2	7.0	94
3	12.1	83
4	15.8	85
5	6.0	90
6	6.9	90
7	12.0	92
8	19.5	93
9	12.0	88
10	9.9	101
11	7.9	93
12	5.3	105
13	5.6	81
14	5.7	76
15	11.7	81
16	7.9	90
17	6.1	81

Table B.38: continued.

18	9.4	81
19	9.4	81
20	8.8	90
21	11.6	88
22	8.8	90
23	7.4	90
24	4.2	90
25	8.8	87
26	10.7	88
27	6.2	77
28	7.2	75
29	10.6	75
30	9.5	76
31	8.5	77
32	12.7	80
33	7.9	83
34	9.3	93
35	16.8	82
36	13.6	80
37	8.0	80
38	10.3	82
39	13.0	84
40	15.4	83
41	7.4	86
42	13.4	90
43	13.1	113
44	6.2	103

Table B. 38: 10107-Tip bridge 2 crack-seal measurements.

10107'-Bridge 11

Figure B. 39: Panchromatic SEM-CL image of 10107-Bridge 11.

Increment #	Measured Thickness (µm)	Measurement Angle
1	4.9	61
2	5.1	90
3	7.4	87
4	8.6	82
5	12.1	84
6	13.3	83
7	10.6	82
8	14.3	79
9	15.3	75
10	10.5	75
11	9.0	88
12	15.5	72
13	7.9	81
14	10.1	86
15	11.0	84
16	11.0	84
17	7.4	84
18	6.2	86
19	12.9	95
20	10.1	94
21	9.7	74
22	8.5	74
23	7.5	99
24	6.2	94

Table B. 39: 10107-Bridge 11 crack-seal measurements.

10106.85'-Bridge 6

Figure B. 40: Panchromatic SEM-CL image of 10106.85-Bridge 6.

Increment #	Measured Thickness (µm)	Measurement Angle (degrees)
1	9.9	79
2	17.7	97
3	9.8	85
4	12.5	92
5	8.4	84
6	10.7	72
7	12.5	86
8	11.6	92
9	8.8	87
10	14.3	90
11	9.7	93
12	13.4	90
13	14.8	94
14	8.9	99
15	16.1	102
16	18.4	102
17	13.2	72
18	8.8	108
19	13.2	108
20	8.4	99
21	12.6	107
22	29.6	115
23	17.4	99
24	17.9	111
25	6.1	99
26	14.9	97
27	13.5	94
28	8.8	90
29	7.0	94
30	8.8	90

Table B. 40: 10106.85-Bridge 6 crack-seal measurements.

10106.85'-Bridge 5

Figure B. 41: Panchromatic SEM-CL image of 10106.85-Bridge 5.

Increment #	Measured Thickness (µm)	Measurement Angle
1	5.9	97
2	5.8	107
3	7.0	87
4	7.0	87
5	10.5	96
6	10.4	90
7	10.5	98
8	7.7	98
9	9.7	94
10	11.5	88
11	6.2	90
12	8.2	102
13	12.1	78
14	7.0	99
15	8.4	99
16	5.2	86
17	7.0	87
18	6.9	90
19	5.9	90
20	13.6	84
21	10.8	88
22	12.5	87

Table B. 41: continued.

23	9.8	96
24	10.2	80
25	11.1	88
26	13.6	93
27	11.6	99
28	9.1	83
29	8.3	88
30	9.3	121
31	8.4	66
32	14.6	94
33	14.3	87
34	11.9	111
35	8.1	100
36	11.9	75
37	10.5	107
38	13.9	71

Table B. 41: 10106.85-Bridge 5 crack-seal measurements.

10106.85'-Bridge 1

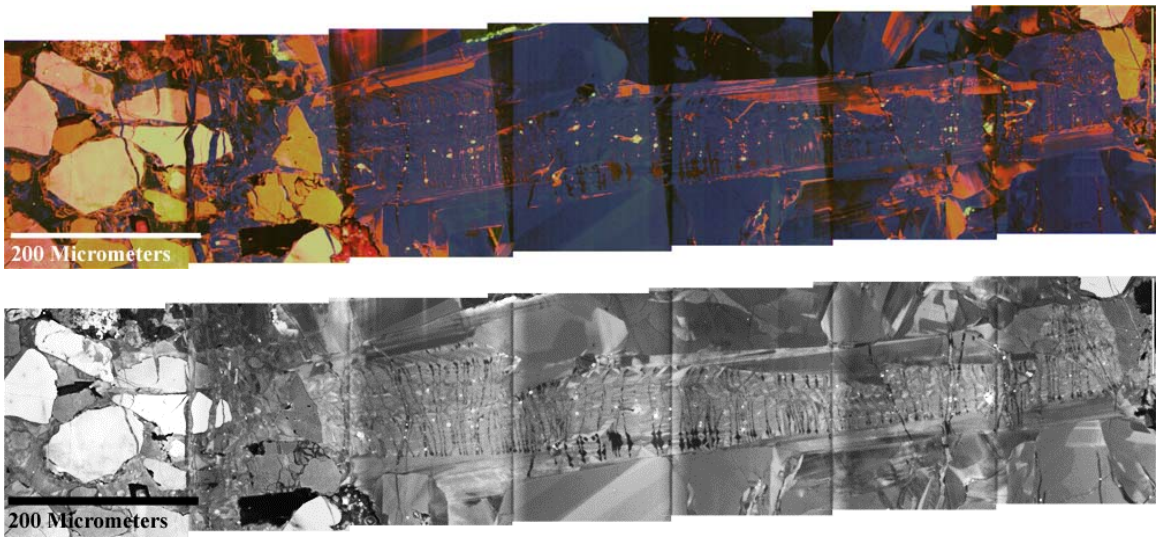

Figure B. 42: **Top**:Color SEM-CL image of 10106.85-Bridge 1. **Bottom**: Panchromatic SEM-CL image of the same bridge.

Increment #	Measured Thickness (µm)	Measurement Angle
1	7.0	73
2	11.6	97
3	8.9	94
4	7.9	95
5	4.9	90
6	6.9	90
7	5.6	90
8	8.3	81
9	8.2	82
10	15.7	90
11	4.7	94
12	7.8	90
13	14.2	86
14	14.7	92
15	5.7	89
16	7.0	90
17	12.9	86

Table B. 42: continued.

18	5.2	89
19	5.2	85
20	4.9	84
21	9.1	90
22	7.1	86
23	5.2	85
24	5.9	96
25	11.1	89
26	7.4	88
27	9.7	87
28	9.4	83
29	7.0	93
30	8.7	109
31	14.2	80
32	7.0	73
33	13.2	72
34	7.6	87
35	10.1	92
36	3.1	90
37	5.9	90
38	5.6	90
39	11.5	87
40	13.5	90
41	9.0	88
42	6.3	87
43	6.3	87
44	8.0	92
45	10.8	88
46	13.9	93
47	8.4	85
48	13.3	84
49	8.0	90
50	8.0	92
51	7.3	90
52	3.8	85
53	9.8	84
54	7.8	100

Table B. 42: continued.

55	13.9	86
56	9.4	84
57	14.3	86
58	6.7	81
59	8.4	83
60	5.2	94
61	9.1	83
62	13.9	90
63	15.3	87
64	12.9	87
65	12.5	87
66	8.7	83
67	8.0	85
68	18.8	85
69	15.3	87
70	21.9	86
71	9.4	86
72	11.1	86
73	29.5	87
74	2.1	81
75	13.4	90
76	6.3	96
77	3.5	90
78	1.7	90
79	1.4	90
80	3.8	85

Table B. 42: 10106.85-Bridge 1 crack-seal measurements.

Increment Average Thickness (µm)	Measured Kinematic Aperture (µm)	Estimated Number of Increments	Number of Increments (counted)
9.2	806.5	88	81

Table B. 43: 10106.85-Bridge 1 key calculated parameters with comparison of counted versus estimated number of increments.

10106.85'-Bridge 4

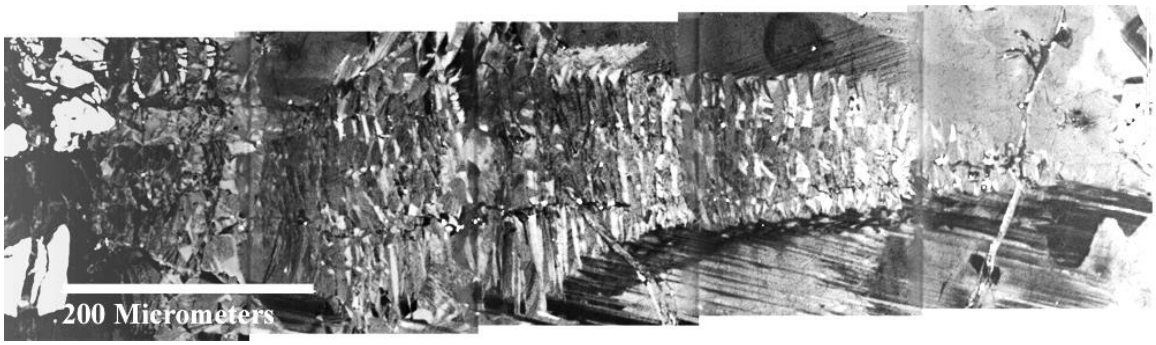

Figure B. 43: Panchromatic SEM-CL image of 10106.85- Bridge 4.

Increment #	Measured Thickness (µm)	Measurement Angle
1	7.9	90
2	3.0	129
3	3.7	90
4	5.4	110
5	10.4	77
6	13.4	90
7	15.3	88
8	16.4	82
9	9.5	129
10	7.9	83
11	11.1	95
12	10.6	90
13	8.8	108
14	9.4	99
15	14.5	97
16	6.9	127

Table B. 44: 10106.85-Bridge 4 crack-seal measurements.

10106.85'-Bridge 3

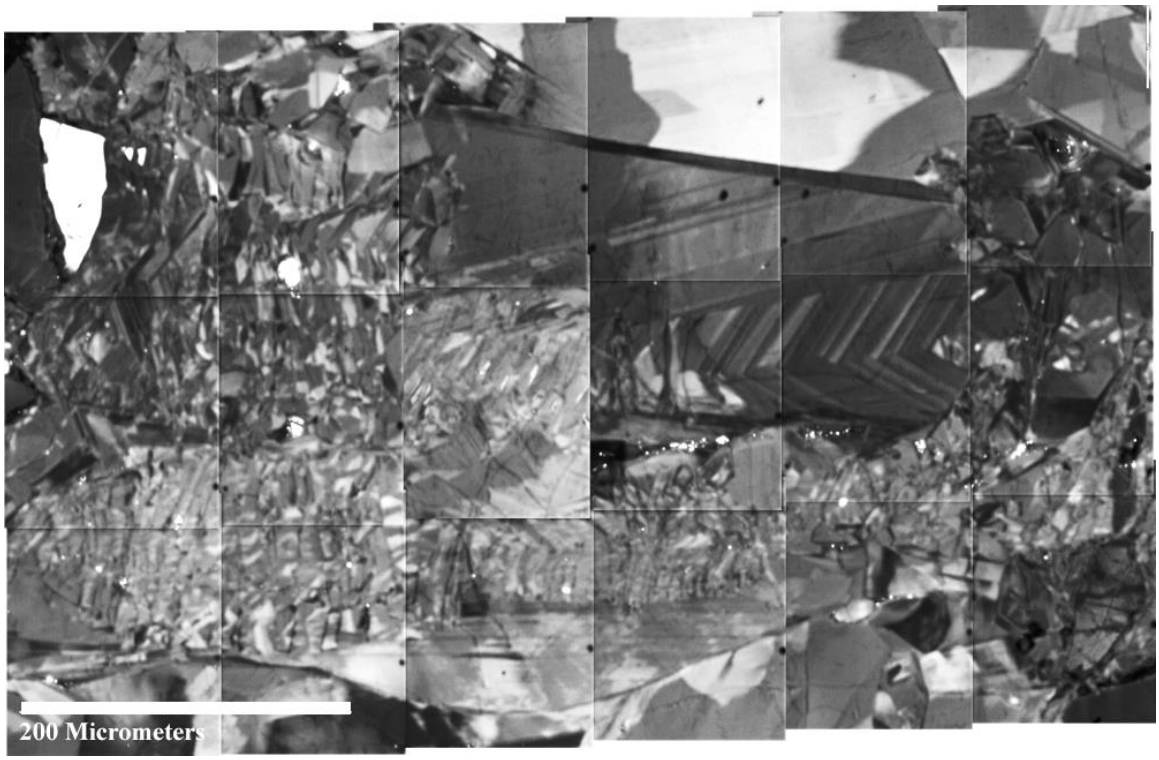

Figure B. 44: Panchromatic SEM-CL image of 10106.85'-Bridge 3.

.

Increment #	Measured Thickness (μm)	Measurement Angle
1	9.9	82
2	10.7	108
3	15.8	76
4	17.8	97
5	15.9	95
6	12.1	90
7	8.8	93
8	8.4	90
9	5.7	104
10	13.5	96
11	12.5	90
12	11.6	95
13	12.1	88
14	7.9	97
15	9.3	90
16	7.0	86
17	9.3	93
18	3.3	90

Table B. 45: 10106.85'-Bridge 3 crack-seal measurements.

10106.85'-Bridge 2

Figure B. 45: Panchromatic SEM-CL image of 10106.85-Bridge 2.

Increment #	Measured Thickness (µm)	Measurement Angle
1	9.6	76
2	21.7	80
3	17.4	110
4	7.9	90
5	11.9	101
6	6.2	103
7	6.9	110
8	13.7	108
9	9.7	107
10	8.4	90
11	9.9	109
12	7.6	101
13	3.7	90
14	3.3	82
15	5.6	90

Table B. 46: 10106.85-Bridge 2 crack-seal measurements.

Appendix C: Bridge Reconstruction

SFOT-1-10106.85- BRIDGE 6 RECONSTRUCTION

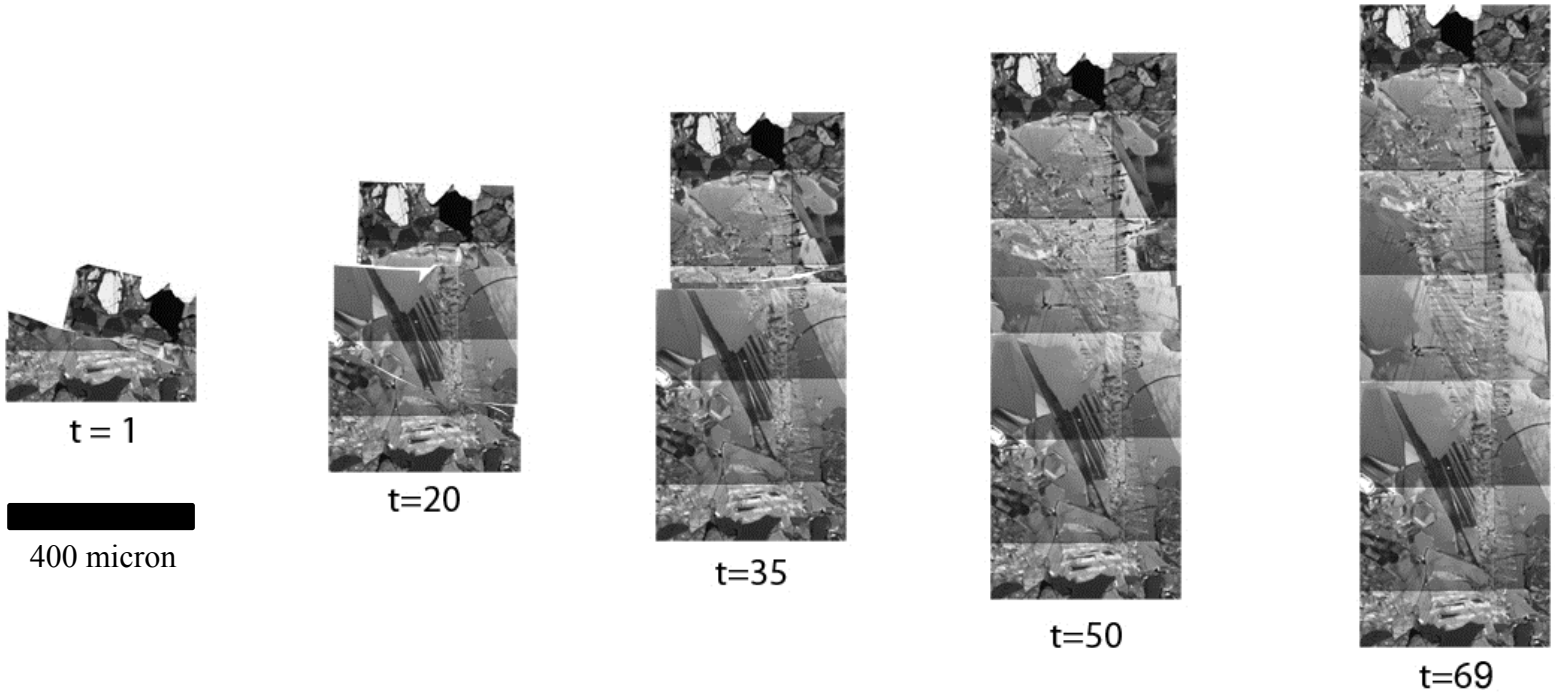

Figure C. 1: Stages of SFOT-1-10106.85- bridge 6 reconstruction (t = relative time).

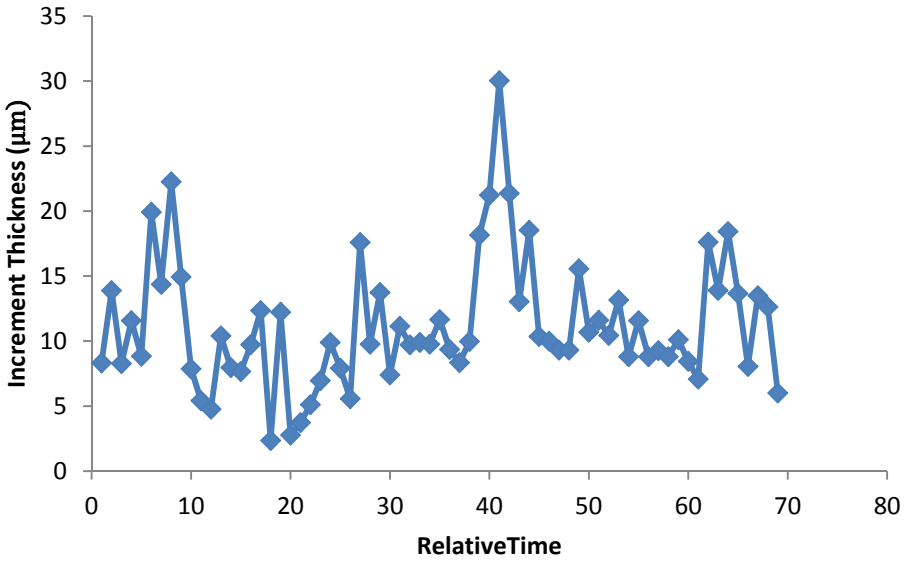

Figure C. 2: Change in increment thickness over time as recorded by crack-seal cement in the reconstructed bridge (SFOT1-10106.85-Bridge6).

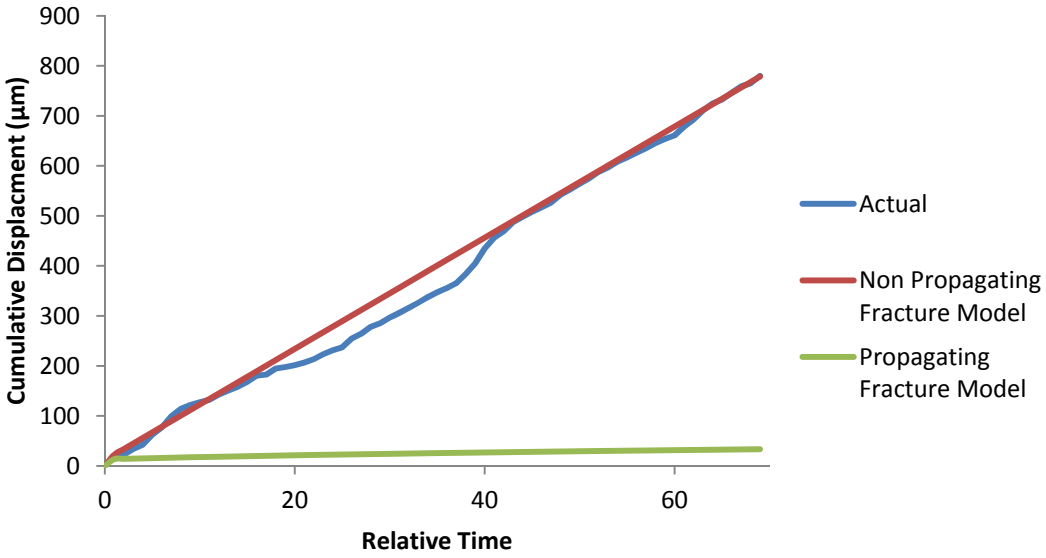

Figure C. 3: Comparison between cumulative displacement in the reconstructed bridge (SFOT-1-10106.85-Bridge-6) and linear elastic fracture mechanics models.

Stationary Model Parameters				Propagating Model Parameters			
x (m)	0.0001	K_{Ic} (MPa/sqrt(m))	1.5	x (m)	0.0001	K_{Ic} (MPa/sqrt(m))	1.5
c (m)	0.0417	Y	0.637	c (m)	0-0.04166	Y	0.637
E (MPa)	1380	υ	0.1	E (MPa)	40000	υ	0.18

Table C. 1: Linear elastic fracture models parameter used in Figure C.3.

References

Abé, H., L. M. Keer, and T. Mura, 1976, Growth rate of a penny-shaped crack in hydraulic fracturing of rocks, 2: Journal of Geophysical Research, v. 81, p. 6292-6298.

Acocella, V., A. Gudmundsson, and R. Funiciello, 2000, Interaction and linkage of extension fractures and normal faults: examples from the rift zone of Iceland: Journal of Structural Geology, v. 22, p. 1233-1246.

Anders, M. H., S. E. Laubach, and C. H. Scholz, 2014, Microfractures: A review: Journal of Structural Geology, v. In press.

Anderson, O. L., and P. C. Grew, 1977, Stress corrosion theory of crack propagation with applications to geophysics: Reviews of Geophysics, v. 15, p. 77-104.

ASTM, 2010, Standard Test Method for Young's Modulus, Tangent Modulus, and Chord Modulus, E111 – 04, West Conshohocken, PA, ASTM.

Atkinson, B. K., 1982, Subcritical crack propagation in rocks: theory, experimental results and applications: Journal of Structural Geology, v. 4, p. 41-56.

Atkinson, B. K., 1984, Subcritical crack growth in geological materials: Journal of Geophysical Research: Solid Earth (1978–2012), v. 89, p. 4077-4114.

Atkinson, B. K., 1987a, Introduction to fracture mechanics and its geophysical applications, *in* B. K. Atkinson, ed., Fracture mechanics of rock: London, Academic Press, p. 1-26.

Atkinson, B. K., 1987b, Introduction to fracture mechanics and its geophysical applications, *in* B. K. Atkinson, ed., Fracture Mechanics of Rock: London, Academic Press, p. 1–26

Atkinson, B. K., and P. G. Meredith, 1981, Stress corrosion cracking of quartz: a note on the influence of chemical environment: Tectonophysics, v. 77, p. T1-T11.

Atkinson, B. K., and P. G. Meredith, 1987, The theory of subcritical crack growth with applications to minerals and rocks: Fracture mechanics of rock, v. 2, p. 111-166.

Aydin, A., 2000, Fractures, faults, and hydrocarbon entrapment, migration and flow: Marine and Petroleum Geology, v. 17, p. 797-814.

Bahat, D., and T. Engelder, 1984, Surface-Morphology on Cross-Fold Joints of the Appalachian Plateau, New-York and Pennsylvania: Tectonophysics, v. 104, p. 299-313.

Bai, T., D. D. Pollard, and M. R. Gross, 2000, Mechanical prediction of fracture aperture in layered rocks: Journal of Geophysical Research: Solid Earth, v. 105, p. 707-721.

Barenblatt, G. I., 1959, The formation of equilibrium cracks during brittle fracture. General ideas and hypotheses. Axially-symmetric cracks: Journal of Applied Mathematics and Mechanics, v. 23, p. 622-636.

Barenblatt, G. I., 1961, The mathematical theory of equilibrium crack formed in brittle fracture: Zhurnal Prikladnoy Mekhaniki i Teknicheskoy, v. 4, p. 3-56.

Batzle, M. L., and G. Simmons, 1976, Microfractures in rocks from two geothermal areas: Earth and Planetary Science Letters, v. 30, p. 71-93.
Batzle, M. L., and G. Simmons, 1977, Geothermal Systems: Rocks, Fluids, Fractures, *in* J. G. Heacock, G. V. Keller, J. E. Oliver, and G. Simmons, eds., The Earth's Crust: Washington, D. C., American Geophysical Union, p. 233-242.
Batzle, M. L., and G. Simmons, 2013, Geothermal Systems: Rocks, Fluids, Fractures, The Earth's Crust, American Geophysical Union, p. 233-242.
Becker, S. P., P. Eichhubl, S. E. Laubach, R. M. Reed, R. H. Lander, and R. J. Bodnar, 2010, A 48 m.y. history of fracture opening, temperature, and fluid pressure: Cretaceous Travis Peak Formation, East Texas basin: Geological Society of America Bulletin, v. 122, p. 1081-1093.
Belayneh, M., 2004, Palaeostress orientation inferred from surface morphology of joints on the southern margin of the Bristol Channel Basin, UK: Geological Society, London, Special Publications, v. 231, p. 243-255.
Bellahsen, N., P. Fiore, and D. D. Pollard, 2006, The role of fractures in the structural interpretation of Sheep Mountain Anticline, Wyoming: Journal of Structural Geology, v. 28, p. 850-867.
Bergerat, F., C. Bouroz-Weil, and J. Angelier, 1992, Palaeostresses inferred from macrofractures, Colorado Plateau, western U.S.A: Tectonophysics, v. 206, p. 219-243.
Bieniawski, Z., 1967a, Mechanism of brittle fracture of rock: Part III—fracture in tension and under long-term loading: International Journal of Rock Mechanics and Mining Sciences & Geomechanics Abstracts, p. 425-430.
Bieniawski, Z. T., 1967b, Mechanism of brittle fracture of rock: Part II—experimental studies: International Journal of Rock Mechanics and Mining Sciences & Geomechanics Abstracts, v. 4, p. 407-423.
Bjorlykke, K., and P. Egeberg, 1993, Quartz cementation in sedimentary basins: AAPG bulletin, v. 77, p. 1538-1548.
Bobet, A., and H. H. Einstein, 1998a, Fracture coalescence in rock-type materials under uniaxial and biaxial compression: International Journal of Rock Mechanics and Mining Sciences, v. 35, p. 863-888.
Bobet, A., and H. H. Einstein, 1998b, Numerical modeling of fracture coalescence in a model rock material: International Journal of Fracture, v. 92, p. 221-252.
Boggs, S., and D. Krinsley, 2006, Application of cathodoluminescence imaging to the study of sedimentary rocks, Cambridge University Press.
Bons, P. D., M. A. Elburg, and E. Gomez-Rivas, 2012, A review of the formation of tectonic veins and their microstructures: Journal of Structural Geology, v. 43, p. 33-62.
Brace, W. F., 1960, An extension of the Griffith theory of fracture to rocks: Journal of Geophysical Research, v. 65, p. 3477.
Brace, W. F., and E. G. Bombolakis, 1963, A note on brittle crack growth in compression: Journal of Geophysical Research, v. 68, p. 3709-3713.

Burley, S. D., J. Mullis, and A. Matter, 1989, Timing diagenesis in the Tartan Reservoir (UK North Sea): constraints from combined cathodoluminescence microscopy and fluid inclusion studies: Marine and Petroleum Geology, v. 6, p. 98-120.

CER, 1985, Coring and logging operations summary, Ashland Exploration Soil Fertility of Texas No. 1, Nacogdoches County, Tx, Las Vegas, NV, Gas Research Institute, p. 103.

Cervantes, P., and D. V. Wiltschko, 2010, Tip to midpoint observations on syntectonic veins, Ouachita orogen, Arkansas: Trading space for time: Journal of Structural Geology, v. 32, p. 1085-1100.

Chan, H., V. Li, and H. Einstein, 1990, A hybridized displacement discontinuity and indirect boundary element method to model fracture propagation: international Journal of Fracture, v. 45, p. 263-282.

Chen, G., J. Kemeny, and S. Harpalani, 1995, Fracture propagation and coalescence in marble plates with pre-cut notches under compression: Proceedings of the Symposium on Fractured and Jointed Rock Masses, Lake Tahoe, CA, p. 435-439.

Cooke, M. L., and D. D. Pollard, 1996, Fracture propagation paths under mixed mode loading within rectangular blocks of polymethyl methacrylate: Journal of Geophysical Research-Solid Earth, v. 101, p. 3387-3400.

Corbett, K., M. Friedman, and J. Spang, 1987, Fracture development and mechanical stratigraphy of Austin Chalk, Texas: AAPG Bulletin, v. 71, p. 17-28.

Correns, C. W., 1949, Growth and dissolution of crystals under linear pressure: Discussions of the Faraday Society, v. 5, p. 267-271.

Corte, A., and A. Higashi, 1964, Experimental research on desiccation cracks in soil.

Cox, S. F., 1987, Antitaxial crack-seal vein microstructures and their relationship to displacement paths: Journal of Structural Geology, v. 9, p. 779-787.

Cox, S. F., and M. A. Etheridge, 1983, Crack-Seal Fiber Growth Mechanisms and Their Significance in the Development of Oriented Layer Silicate Microstructures: Tectonophysics, v. 92, p. 147-170.

Cruse, T. A., and W. Vanburen, 1971, Three-dimensional elastic stress analysis of a fracture specimen with an edge crack: International Journal of Fracture Mechanics, v. 7, p. 1-15.

Datta-Gupta, A., L. Lake, and G. Pope, 1995, Characterizing heterogeneous permeable media with spatial statistics and tracer data using sequential simulated annealing: Mathematical Geology, v. 27, p. 763-787.

DeGraff, J. M., and A. Aydin, 1987, Surface morphology of columnar joints and its significance to mechanics and direction of joint growth: Geological Society of America Bulletin, v. 99, p. 605-617.

Delaney, P. T., and D. D. Pollard, 1981, Deformation of host rocks and flow of magma during growth of minette dikes and breccia-bearing intrusions near Ship Rock, New Mexico, *in* USGS, ed., Washington D.C., U.S. G.P.O.

Den Brok, S., and C. Spiers, 1991, Experimental evidence for water weakening of quartzite by microcracking plus solution-precipitation creep: J. Geol. Soc. London, v. 148, p. 541-548.

Dietrich, D., and P. R. Grant, 1985, Cathodoluminescence petrography of syntectonic quartz fibres: Journal of Structural Geology, v. 7, p. 541-553.
Dugdale, D., 1960, Yielding of steel sheets containing slits: Journal of the Mechanics and Physics of Solids, v. 8, p. 100-104.
Duncan, A., C. Hanks, W. K. Wallace, P. B. O'Sullivan, and T. M. Parris, 2012, An integrated model of the structural evolution of the central Brooks Range foothills, Alaska, using structural geometry, fracture distribution, geochronology, and microthermometry: AAPG bulletin, v. 96, p. 2245-2274.
Durney, D., and J. Ramsay, 1973, Incremental strains measured by syntectonic crystal growths, *in* K. A. De Jong, and R. Scholten, eds., Gravity and tectonics: New York, Wiley, p. 67-96.
Dutton, S. P., 1986, Diagenesis and burial history of the Lower Cretaceous Travis Peak Formation, East Texas, University of Texas at Austin, Ann Arbor, MI.
Dutton, S. P., and T. N. Diggs, 1990, History of Quartz Cementation in the Lower Cretaceous Travis Peak Formation, East Texas: SEPM Journal of Sedimentary Research, v. 60, p. 191-202.
Dutton, S. P., and L. S. Land, 1988, Cementation and burial history of a low-permeability quartzarenite, Lower Cretaceous Travis Peak Formation, East Texas: Geological Society of America Bulletin, v. 100, p. 1271-1282.
Dyer, R., 1988, Using joint interactions to estimate paleostress ratios: Journal of Structural Geology, v. 10, p. 685-699.
Eichhubl, P., 2004, Growth of ductile opening-mode fractures in geomaterials: Geological Society, London, Special Publications, v. 231, p. 11-24.
Eichhubl, P., and A. Aydin, 2003, Ductile opening-mode fracture by pore growth and coalescence during combustion alteration of siliceous mudstone: Journal of Structural Geology, v. 25, p. 121-134.
Eichhubl, P., and J. R. Boles, 2000, Rates of fluid flow in fault systems; evidence for episodic rapid fluid flow in the Miocene Monterey Formation, coastal California: American Journal of Science, v. 300, p. 571-600.
Einstein, H. H., R. Hirschfeld, R. Nelson, and R. Bruhn, 1969, Model studies of jointed-rock behavior: The 11th US Symposium on Rock Mechanics (USRMS).
Einstein, H. H., and R. C. Hirschfeld, 1973, Model studies on mechanics of jointed rock: Journal of the Soil Mechanics and Foundations Division, v. 99, p. 229-248.
Einstein, H. H., and O. Stephansson, 2000, Fracture Systems Fracture Propagation And Coalescence: ISRM International Symposium.
Ellis, M. A., S. E. Laubach, P. Eichhubl, J. E. Olson, and P. Hargrove, 2012, Fracture development and diagenesis of Torridon Group Applecross Formation, near An Teallach, NW Scotland: millennia of brittle deformation resilience?: Journal of the Geological Society, v. 169, p. 297-310.
Engelder, T., 1985, Loading paths to joint propagation during a tectonic cycle: an example from the Appalachian Plateau, U.S.A: Journal of Structural Geology, v. 7, p. 459-476.

Engelder, T., 2007, Propagation Velocity of Joints: A Debate over Stable vs. Unstable Growth of Cracks in the Earth, *in* J. R. Varner, G. D. Quinn, and M. Wightman, eds., Fractography of Glasses and Ceramics V: Ceramic Transactions, v. 199, John Wiley & Sons, Inc., p. 455-482.

Engelder, T., M. Fischer, and M. R. Gross, 1993, Geological Aspects of Fracture Mechanics: GSA Short Course: Boston, Ma.

Engelder, T., and P. Geiser, 1980, On the use of regional joint sets as trajectories of paleostress fields during the development of the Appalachian Plateau, New York: Journal of Geophysical Research: Solid Earth, v. 85, p. 6319-6341.

Engelder, T., and G. Oertel, 1985, Correlation between abnormal pore pressure and tectonic jointing in the Devonian Catskill Delta: Geology, v. 13, p. 863-866.

Fall, A., P. Eichhubl, R. J. Bodnar, S. E. Laubach, and J. S. Davis, 2014, Natural hydraulic fracturing of tight-gas sandstone reservoirs, Piceance Basin, Colorado: Geological Society of America Bulletin, v. In press.

Fall, A., P. Eichhubl, S. P. Cumella, R. J. Bodnar, S. E. Laubach, and S. P. Becker, 2012, Testing the basin-centered gas accumulation model using fluid inclusion observations: Southern Piceance Basin, Colorado: AAPG Bulletin, v. 96, p. 2297-2318.

Flodin, E. A., and A. Aydin, 2004, Evolution of a strike-slip fault network, Valley of Fire State Park, southern Nevada: Geological Society of America Bulletin, v. 116, p. 42-59.

Gale, J. F. W., R. H. Lander, R. M. Reed, and S. E. Laubach, 2010, Modeling fracture porosity evolution in dolostone: Journal of Structural Geology, v. 32, p. 1201-1211.

Gale, J. F. W., R. M. Reed, and J. Holder, 2007, Natural fractures in the Barnett Shale and their importance for hydraulic fracture treatments: AAPG Bulletin, v. 91, p. 603-622.

Gaviglio, P., 1986, Crack-seal mechanism in a limestone: A factor of deformation in strike-slip faulting: Tectonophysics, v. 131, p. 247-255.

Gomez, L. A., and S. E. Laubach, 2006, Rapid digital quantification of microfracture populations: Journal of Structural Geology, v. 28, p. 408-420.

Götze, J., and W. Zimmerle, 2000, Quartz and silica as guide to provenance in sediments and sedimentary rocks: Contributions to Sedimentary Geology, v. 21, KG Saur Verlag Gmbh & Co.

Granier, T., 1985, Origin, damping, and pattern of development of faults in granite: Tectonics, v. 4, p. 721-737.

Griffith, A. A., 1921, The Phenomena of Rupture and Flow in Solids: Philosophical Transactions of the Royal Society A: Mathematical, Physical and Engineering Sciences, v. 221, p. 163-198.

Griffith, A. A., 1924, The theory of rupture: the first international congress on applied mechanics.

Gross, B., J. E. Srawley, and W. F. Brown Jr, 1964, Stress-intensity factors for a single-edge-notch tension specimen by boundary collocation of a stress function, DTIC Document.

Gross, M. R., 1993, The origin and spacing of cross joints: examples from the Monterey Formation, Santa Barbara Coastline, California: Journal of Structural Geology, v. 15, p. 737-751.

Gross, M. R., and T. Engelder, 1995, Strain accommodated by brittle failure in adjacent units of the Monterey Formation, U.S.A.: scale effects and evidence for uniform displacement boundary conditions: Journal of Structural Geology, v. 17, p. 1303-1318.

Gross, M. R., and Y. Eyal, 2007, Throughgoing fractures in layered carbonate rocks: Geological Society of America Bulletin, v. 119, p. 1387-1404.

Gudmundsson, A., 1983, Stress estimates from the length/width ratios of fractures: Journal of structural geology, v. 5, p. 623-626.

Gudmundsson, A., 1987, Geometry, formation and development of tectonic fractures on the Reykjanes Peninsula, southwest Iceland: Tectonophysics, v. 139, p. 295-308.

Gudmundsson, A., 2000, Fracture dimensions, displacements and fluid transport: Journal of Structural Geology, v. 22, p. 1221-1231.

Gudmundsson, A., 2011, Rock fractures in geological processes: Cambridge, United Kingdom, Cambridge University Press.

Gudmundsson, A., and S. L. Brenner, 2001, How hydrofractures become arrested: Terra Nova, v. 13, p. 456-462.

Gudmundsson, A., I. Fjeldskaar, and S. L. Brenner, 2002, Propagation pathways and fluid transport of hydrofractures in jointed and layered rocks in geothermal fields: Journal of Volcanology and Geothermal Research, v. 116, p. 257-278.

Hancock, P. L., 1985, Brittle microtectonics: principles and practice: Journal of Structural Geology, v. 7, p. 437-457.

Hanks, C. L., T. M. Parris, and W. K. Wallace, 2006, Fracture paragenesis and microthermometry in Lisburne Group detachment folds: Implications for the thermal and structural evolution of the northeastern Brooks Range, Alaska: AAPG Bulletin, v. 90, p. 1-20.

Hatzor, Y. H., and V. Palchik, 1997, The influence of grain size and porosity on crack initiation stress and critical flaw length in dolomites: International Journal of Rock Mechanics and Mining Sciences, v. 34, p. 805-816.

Helgeson, D. E., and A. Aydin, 1991, Characteristics of joint propagation across layer interfaces in sedimentary rocks: Journal of Structural Geology, v. 13, p. 897-911.

Hennings, P. H., J. E. Olson, and L. B. Thompson, 2000, Combining Outcrop Data and Three-Dimensional Structural Models to Characterize Fractured Reservoirs: An Example from Wyoming: AAPG Bulletin, v. 84, p. 830-849.

Hilgers, C., and J. L. Urai, 2002, Microstructural observations on natural syntectonic fibrous veins: implications for the growth process: Tectonophysics, v. 352, p. 257-274.

Hirata, T., 1989, Fractal dimension of fault systems in Japan: Fractal structure in rock fracture geometry at various scales, Fractals in Geophysics, Springer, p. 157-170.
Ho, S., and Z. Suo, 1993, Tunneling Cracks in Constrained Layers: Journal of Applied Mechanics, v. 60, p. 890-894.
Hodgson, R. A., 1961a, Classification of structures on joint surfaces: American Journal of Science, v. 259, p. 493-502.
Hodgson, R. A., 1961b, Regional study of jointing in Comb Ridge-Navajo mountain area, Arizona and Utah: AAPG Bulletin, v. 45, p. 1-38.
Hoek, E., and Z. T. Bieniawski, 1965, Brittle fracture propagation in rock under compression: International Journal of Fracture Mechanics, v. 1.
Holditch, S. A., B. M. Robinson, and W. S. Whitehead, 1985, Operating GRI's Mobile Testing and Control Facility, Gas Research Institute Annual Report, College Station, Texas, S. A. Holditch & Associates Inc.
Hood, S. D., C. S. Nelson, and P. J. J. Kamp, 2003, Modification of fracture porosity by multiphase vein mineralization in an Oligocene nontropical carbonate reservoir, Taranaki Basin, New Zealand: AAPG Bulletin, v. 87, p. 1575-1597.
Hooker, J. N., J. F. W. Gale, L. A. Gomez, S. E. Laubach, R. Marrett, and R. M. Reed, 2009, Aperture-size scaling variations in a low-strain opening-mode fracture set, Cozzette Sandstone, Colorado: Journal of Structural Geology, v. 31, p. 707-718.
Hubbert, M. K., 1972, Natural and induced fracture orientation.
Hudson, J. A., and J. P. Harrison, 1997, Engineering rock mechanics: an introduction to the principles: Tarrytown, NY, Pergamon.
Hulin, C. D., 1929, Structural control of ore deposition: Economic Geology, v. 24, p. 15-49.
Hutchinson, J. W., 1996, Stresses and failure modes in thin films and multilayers: Notes for a Dcamm Course. Technical University of Denmark, Lyngby, p. 1-45.
Inglis, C., 1913, Stresses in a cracked plate due to the presence of cracks and sharp corners: Transaction of Naval Architects (London), v. 60, p. 213.
Irwin, G. R., 1957, Analysis of stresses and strains near the end of a crack traversing a plate: J. appl. Mech.
Jackson, M. P. A., and S. J. Seni, 1983, Geometry and evolution of salt structures in a marginal rift basin of the Gulf of Mexico, east Texas: Geology, v. 11, p. 131-135.
Jizba, D. L., 1991, Mechanical and Acoustical Properties of Sandstones and Shales, Stanford University, Stanford, 275 p.
Kaylor, A. L., 2011, A fluid inclusion and cathodoluminescence approach to reconstruct fracture growth in the Triassic-Jurassic La Boca Formation, Northeastern Mexico, The University of Texas at Austin, Austin, Texas.
Kirby, S. H., 1984, Introduction and digest to the special issue on chemical effects of water on the deformation and strengths of rocks: Journal of Geophysical Research, v. 89, p. 3991-3995.
Kishimoto, K., W. Soboyejo, J. Knott, and R. Smith, 1989, A numerical investigation of the interaction and coalescence of twin coplanar semi-elliptical fatigue cracks: International journal of fatigue, v. 11, p. 91-96.

Knipe, R. J., 1977, The application of high voltage electron microscopy to the study of deformation mechanisms in low grade metamorphic rocks, Imperial College (University of London), London.

Kulander, B. R., C. C. Barton, and S. L. Dean, 1979, Application of fractography to core and outcrop fracture investigations, Department of Energy, Morgantown, WV (USA). Morgantown Energy Research Center.

Kulander, B. R., and S. L. Dean, 1985, Hackle Plume Geometry and Joint Propagation Dynamics: Fundamentals of rock joints: International Symposium on Fundamentals of Rock Joints Proceedings, p. 85-94.

Lacazette, A., and T. Engelder, 1992, Chapter 12 Fluid-driven Cyclic Propagation of a Joint in the Ithaca Siltstone, Appalachian Basin, New York, *in* E. Brian, and W. Teng-fong, eds., Fault Mechanics and Transport Properties of Rocks: San Diego, Academic Press, p. 297-323.

Lander, R. H., R. E. Larese, and L. M. Bonnell, 2008, Toward more accurate quartz cement models: The importance of euhedral versus noneuhedral growth rates: AAPG Bulletin, v. 92, p. 1537-1563.

Lander, R. H., and S. E. Laubach, 2014, Insights into rates of fracture growth and sealing from a model for quartz cementation in fractured sandstones: GSA Bulletin, v. In press.

Lander, R. H., and O. Walderhaug, 1999, Predicting porosity through simulating sandstone compaction and quartz cementation: Aapg Bulletin-American Association of Petroleum Geologists, v. 83, p. 433-449.

Landtwing, M. R., and T. Pettke, 2005, Relationships between SEM-cathodoluminescence response and trace-element composition of hydrothermal vein quartz: American Mineralogist, v. 90, p. 122-131.

Laubach, S. E., 1988, Subsurface fractures and their relationship to stress history in East Texas basin sandstone: Tectonophysics, v. 156, p. 37-49.

Laubach, S. E., 1989, Fracture Analysis of the Travis Peak Formation, Western Flank of the Sabine Arch, East Texas, Report of Investigations 185, Austin, TX, Bureau of Economic Geology, The University of Texas at Austin, p. 1-55.

Laubach, S. E., 1997, A method to detect natural fracture strike in sandstones: AAPG Bulletin, v. 81, p. 604-623.

Laubach, S. E., 2003, Practical approaches to identifying sealed and open fractures: AAPG Bulletin, v. 87, p. 561-579.

Laubach, S. E., and K. Diaz-Tushman, 2009, Laurentian palaeostress trajectories and ephemeral fracture permeability, Cambrian Eriboll Formation sandstones west of the Moine Thrust Zone, NW Scotland: Journal of the Geological Society, v. 166, p. 349-362.

Laubach, S. E., and J. F. W. Gale, 2006, Obtaining fracture information for low-permeability (tight) gas sandstones from sidewall cores: Journal of Petroleum Geology, v. 29, p. 147-158.

Laubach, S. E., and M. L. W. Jackson, 1990, Origin of arches in the northwestern Gulf of Mexico basin: Geology, v. 18, p. 595-598.

Laubach, S. E., R. H. Lander, L. M. Bonnell, J. E. Olson, and R. M. Reed, 2004a, Opening histories of fractures in sandstone: Geological Society, London, Special Publications, v. 231, p. 1-9.

Laubach, S. E., J. E. Olson, and M. R. Gross, 2009, Mechanical and fracture stratigraphy: AAPG Bulletin, v. 93, p. 1413-1426.

Laubach, S. E., R. M. Reed, J. E. Olson, R. H. Lander, and L. M. Bonnell, 2004b, Coevolution of crack-seal texture and fracture porosity in sedimentary rocks: cathodoluminescence observations of regional fractures: Journal of Structural Geology, v. 26, p. 967-982.

Laubach, S. E., and M. E. Ward, 2006, Diagenesis in porosity evolution of opening-mode fractures, Middle Triassic to Lower Jurassic La Boca Formation, NE Mexico: Tectonophysics, v. 419, p. 75-97.

Law, B. E., and C. Spencer, 1998, Chapter 1: Abnormal Pressure in Hydrocarbon Environments: AAPG Memoir v. 70.

Lawn, B., and R. Wilshaw, 1975, Indentation fracture: principles and applications: Journal of Materials Science, v. 10, p. 1049-1081.

Leamy, H. J., 1982, Charge collection scanning electron microscopy: Journal of Applied Physics, v. 53, p. R51-R80.

Lee, Y.-J., and D. V. Wiltschko, 2000, Fault controlled sequential vein dilation: competition between slip and precipitation rates in the Austin Chalk, Texas: Journal of Structural Geology, v. 22, p. 1247-1260.

Long, J. C. S., and P. A. Witherspoon, 1985, The relationship of the degree of interconnection to permeability in fracture networks: Journal of Geophysical Research: Solid Earth, v. 90, p. 3087-3098.

Marrett, R., O. J. Ortega, and C. M. Kelsey, 1999, Extent of power-law scaling for natural fractures in rock: Geology, v. 27, p. 799-802.

Martin, R. J., 1972, Time-dependent crack growth in quartz and its application to the creep of rocks: Journal of Geophysical Research, v. 77, p. 1406-1419.

Massabo, R., 1999, The Bridged-Crack Model, *in* A. Carpinteri, ed., Nonlinear Crack Models for Nonmetallic Material: Netherlands, Springer.

Matter, A., and K. Ramseyer, 1985, Cathodoluminescence Microscopy as a Tool for Provenance Studies of Sandstones, *in* G. G. Zuffa, ed., Provenance of Arenites: NATO ASI Series, v. 148: Netherlands, Springer p. 191-211.

Mayor, J. N., and F. S. Fisher, 1972, Middle Tertiary Replacement Ore Bodies and Associated Veins in the Northwest San Juan Mountains, Colorado: Economic Geology, v. 67, p. 214-230.

McConaughy, D. T., and T. Engelder, 2001, Joint initiation in bedded clastic rocks: Journal of Structural Geology, v. 23, p. 203-221.

McLennan, J. A., P. F. Allwardt, P. H. Hennings, and H. E. Farrell, 2009, Multivariate fracture intensity prediction: Application to Oil Mountain anticline, Wyoming: AAPG bulletin, v. 93, p. 1585-1595.

Miller, J., 1988, Cathodoluminescence microscopy, *in* M. Tucker, ed., Techniques in Sedimentology: Oxford, Blackwell, p. 174-190.

Milliken, K. L., and S. E. Laubach, 2000, Brittle Deformation in Sandstone Diagenesis as Revealed by Scanned Cathodoluminescence Imaging with Application to Characterization of Fractured Reservoirs, *in* M. Pagel, V. Barbin, P. Blanc, and D. Ohnenstetter, eds., Cathodoluminescence in Geosciences: Netherlands, Springer Berlin Heidelberg, p. 225-243.

Milodowski, A. E., M. R. Gillespie, J. Naden, N. J. Fortey, T. J. Shepherd, J. M. Pearce, and R. Metcalfe, 1998, The petrology and paragenesis of fracture mineralization in the Sellafield area, west Cumbria: Proceedings of the Yorkshire Geological Society, v. 52, p. 215-241.

Moros, J. G., 1999, Relationship between fracture aperture and length in sedimentary rocks, The University of Texas at Austin, Austin, Texas.

Narr, W., and J. B. Currie, 1982, Origin of fracture porosity--example from Altamont field, Utah: AAPG Bulletin, v. 66, p. 1231-1247.

National Research Council, 1996, Rock fractures and fluid flow: contemporary understanding and applications: Washington, D.C., National Academy Press, 551 p.

Nelson, R. A., 1985, Geologic analysis of naturally fractured reservoirs: Contributions in petroleum geology & engineering ;v. 1: Houston, Gulf Pub. Co., Book Division, 320 p.

Nicholson, R., and D. D. Pollard, 1985, Dilation and linkage of echelon cracks: Journal of Structural Geology, v. 7, p. 583-590.

Noiriel, C., F. Renard, M.-L. Doan, and J.-P. Gratier, 2010, Intense fracturing and fracture sealing induced by mineral growth in porous rocks: Chemical Geology, v. 269, p. 197-209.

Nur, A., 1982, The origin of tensile fracture lineaments: Journal of Structural Geology, v. 4, p. 31-40.

Ode, H., 1956, A note concerning the mechanism of artificial and natural hydraulic fracture systems: The 1st US Symposium on Rock Mechanics (USRMS).

Olson, J. E., 1993, Joint pattern development: Effects of subcritical crack growth and mechanical crack interaction: Journal of Geophysical Research: Solid Earth, v. 98, p. 12251-12265.

Olson, J. E., 2004, Predicting fracture swarms — the influence of subcritical crack growth and the crack-tip process zone on joint spacing in rock: Geological Society, London, Special Publications, v. 231, p. 73-88.

Olson, J. E., S. E. Laubach, and R. H. Lander, 2009, Natural fracture characterization in tight gas sandstones: Integrating mechanics and diagenesis: AAPG Bulletin, v. 93, p. 1535-1549.

Olson, J. E., and D. D. Pollard, 1991, The initiation and growth of en échelon veins: Journal of Structural Geology, v. 13, p. 595-608.

Ortega, O., and R. Marrett, 2000, Prediction of macrofracture properties using microfracture information, Mesaverde Group sandstones, San Juan basin, New Mexico: Journal of Structural Geology, v. 22, p. 571-588.

Osborne, M. J., and R. E. Swarbrick, 1997, Mechanisms for generating overpressure in sedimentary basins: a reevaluation: AAPG bulletin, v. 81, p. 1023-1041.
Parris, T. M., R. C. Burruss, and P. B. O'Sullivan, 2003, Deformation and the timing of gas generation and migration in the eastern Brooks Range foothills, Arctic National Wildlife Refuge, Alaska: AAPG Bulletin, v. 87, p. 1823-1846.
Paterson, M. S., and T.-f. Wong, 2005, Experimental Rock Deformation: The Brittle Field: Netherlands, Springer Berlin Heidelberg, 314 p.
Peacock, D., 2001, The temporal relationship between joints and faults: Journal of Structural Geology, v. 23, p. 329-341.
Penczak, R. S., and R. Mason, 1997, Metamorposed Archean epithermal Au-As-Sb-Zn-(Hg) vein mineralization at the Campbell Mine, northeastern Ontario: Economic Geology, v. 92, p. 696-719.
Petit, J.-P., 1995, Palaeostress superimposition deduced from mesoscale structures in limestone: the Matelles exposure, Languedoc, France: Journal of Structural Geology, v. 17, p. 245-256.
Philip, Z. G., J. W. Jennings, J. E. Olson, S. E. Laubach, and J. Holder, 2005, Modeling Coupled Fracture-Matrix Fluid Flow in Geomechanically Simulated Fracture Networks: SPE Reservoir Evaluation & Engineering, v. 8, p. 300-309.
Pittman, E. D., 1979, Porosity diagenesis and productive capability of sandstone reservoirs.
Pollard, D., and A. Aydin, 1988, Progress in Understanding Jointing over the Past Century: Geological Society of America Bulletin, v. 100, p. 1181-1204.
Pollard, D., and P. Segall, 1987, Theoretical displacements and stresses near fractures in rock: with applications to faults, joints, veins, dikes, and solution cavities, *in* B. K. Atkinson, ed., Fracture mechanics of rock: London, Academic Press, p. 277-350.
Pollard, D. D., P. Segall, and P. T. Delaney, 1982, Formation and interpretation of dilatant echelon cracks: Geological Society of America Bulletin, v. 93, p. 1291.
Potluri, N. K., D. Zhu, and A. D. Hill, 2005, The Effect of Natural Fractures on Hydraulic Fracture Propagation, Society of Petroleum Engineers.
Price, N. J., 1966, Fault and joint development in brittle and semi-brittle rock: Oxford, Pergamon Press 176 p.
Ramsay, J. G., 1980, The Crack-Seal Mechanism of Rock Deformation: Nature, v. 284, p. 135-139.
Reed, R. M., and K. L. Milliken, 2003, How to overcome imaging problems associated with carbonate minerals on SEM-based cathodoluminescence systems: Journal of Sedimentary Research, v. 73, p. 328-332.
Renard, F., M. Andréani, A.-M. Boullier, and P. Labaume, 2005, Crack-seal patterns: records of uncorrelated stress release variations in crustal rocks, *in* D. Gapais, J. P. Brun, and P. R. Cobbold, eds., Deformation Mechanisms, Rheology and Tectonics: From Minerals to the Lithosphere Special Publication, v. 243: London, Geological Society, London, p. 67-79.
Renshaw, C. E., and D. D. Pollard, 1995, An experimentally verified criterion for propagation across unbounded frictional interfaces in brittle, linear elastic

materials: International Journal of Rock Mechanics and Mining Sciences & Geomechanics Abstracts, v. 32, p. 237-249.
Reyes, O., and H. Einstein, 1991, Failure mechanisms of fractured rock-a fracture coalescence model: 7th ISRM Congress.
Rijken, P., J. Holder, J. E. Olson, and S. E. Laubach, 2002, Predicting Fracture Attributes in the Travis Peak Formation Using Quantitative Mechanical Modeling and Structural Diagenesis: Gulf Coast Association of Geological Societies Transactions, v. 52, p. 837-847.
Robertson, E. C., 1955, Experimental study of the strength of rocks: Geological Society of America Bulletin, v. 66, p. 1275-1314.
Rossmanith, H. P., 1983, Rock fracture mechanics, v. no. 275: Wien, Springer-Verlag.
Sack, R. A., 1946, Extension of Griffith's theory of rupture to three dimensions: Proceedings of the Physical Society, v. 58, p. 729-736.
Scholz, C. H., 1972, Static fatigue of quartz: Journal of Geophysical Research, v. 77, p. 2104-2114.
Schultz, R. A., 2000, Growth of geologic fractures into large-strain populations: review of nomenclature, subcritical crack growth, and some implications for rock engineering: International Journal of Rock Mechanics and Mining Sciences, v. 37, p. 403-411.
Secor, D., 1969, Mechanics of natural extension fracturing at depth in the earth's crust: Research in tectonics: Geological Survey of Canada Special Paper, p. 68-52.
Secor, D. T., 1965, Role of fluid pressure in jointing: American Journal of Science, v. 263, p. 633-646.
Segall, P., 1984, Formation and growth of extensional fracture sets: Geological Society of America Bulletin, v. 95, p. 454-462.
Segall, P., and D. D. Pollard, 1983, Joint formation in granitic rock of the Sierra Nevada: Geological Society of America Bulletin, v. 94, p. 563-575.
Shen, B., O. Stephansson, H. H. Einstein, and B. Ghahreman, 1995, Coalescence of fractures under shear stresses in experiments: Journal of Geophysical Research: Solid Earth, v. 100, p. 5975-5990.
Smart, K. J., D. A. Ferrill, and A. P. Morris, 2009, Impact of interlayer slip on fracture prediction from geomechanical models of fault-related folds: AAPG bulletin, v. 93, p. 1447-1458.
Soeder, D. J., and P. Chowdiah, 1990, Pore Geometry in High- and Low-Permeability Sandstones, Travis Peak Formation, East Texas: Society of Petroleum Engineers Symposium on Gas Technology, p. 239-252.
Spencer, C. W., 1987, Hydrocarbon generation as a mechanism for overpressuring in Rocky Mountain region: AAPG bulletin, v. 71, p. 368-388.
Srivastava, D. C., and T. Engelder, 1990, Crack-propagation sequence and pore-fluid conditions during fault-bend folding in the Appalachian Valley and Ridge, central Pennsylvania: Geological Society of America Bulletin, v. 102, p. 116-128.
Stearns, D. W., and M. Friedman, 1972, Reservoirs in fractured rock: Geologic exploration methods: AAPG Memoir, v. 16.

Swain, M., J. Williams, B. Lawn, and J. Beek, 1973, A comparative study of the fracture of various silica modifications using the Hertzian test: Journal of Materials Science, v. 8, p. 1153-1164.

Taber, S., 1916, The origin of veins of the asbestiform minerals: Proceedings of the National Academy of Sciences of the United States of America, v. 2, p. 659-664.

Tang, M., J. Zhang, H. Ma, and S. Lu, 2013, Fracture modelling based on the stochastic extended finite element method: Petroleum Geoscience.

Twiss, R. J., and E. M. Moores, 1992, Structural Geology, W. H. Freeman.

Underwood, C. A., M. L. Cooke, J. A. Simo, and M. A. Muldoon, 2003, Stratigraphic controls on vertical fracture patterns in Silurian dolomite, northeastern Wisconsin: AAPG Bulletin, v. 87, p. 121-142.

Urai, J. L., P. F. Williams, and H. L. M. Van Roermund, 1991, Kinematics of crystal growth in syntectonic fibrous veins: Journal of Structural Geology, v. 13, p. 823-836.

Van Noten, K., P. Muchez, and M. Sintubin, 2011, Stress-state evolution of the brittle upper crust during compressional tectonic inversion as defined by successive quartz vein types (High-Ardenne slate belt, Germany): Journal of the Geological Society, v. 168, p. 407-422.

Walderhaug, O., 1994a, Precipitation rates for quartz cement in sandstones determined by fluid-inclusion microthermometry and temperature-history modeling: Journal of Sedimentary Research, v. 64.

Walderhaug, O., 1994b, Temperatures of quartz cementation in Jurassic sandstones from the Norwegian continental shelf--evidence from fluid inclusions: Journal of Sedimentary Research, v. 64.

Walderhaug, O., and J. Rykkje, 2000, Some Examples of the Effect of Crystallographic Orientation on the Cathodoluminescence Colors of Quartz: Journal of Sedimentary Research, v. 70, p. 545-548.

Weinberger, R., 1999, Initiation and growth of cracks during desiccation of stratified muddy sediments: Journal of Structural Geology, v. 21, p. 379-386.

Weyl, P. K., 1959, Pressure solution and the force of crystallization: a phenomenological theory: Journal of Geophysical Research, v. 64, p. 2001-2025.

Wilkins, S. J., 2007, Fracture intensity from geomechanical models: application to the Blue Forest 3D survey, Green River Basin, Wyoming, USA: Geological Society, London, Special Publications, v. 292, p. 137-157.

Williamson, M. A., and C. Smyth, 1992, Timing of gas and overpressure generation in the Sable Basin offshore Nova Scotia: implications for gas migration dynamics: Bulletin of Canadian Petroleum Geology, v. 40, p. 151-169.

Wiltschko, D. V., and J. W. Morse, 2001, Crystallization pressure versus “crack seal” as the mechanism for banded veins: Geology, v. 29, p. 79-82.

Wong, R. H., and K. Chau, 1998, Crack coalescence in a rock-like material containing two cracks: International Journal of Rock Mechanics and Mining Sciences, v. 35, p. 147-164.

Woodworth, J. B., 1896, On the Fracture System of Joints: With Remarks on Certain Fractures: Boston Society of Natural Historical Proceedings, v. 27, p. 164-183.
Wu, H., and D. D. Pollard, 1992, Propagation of a set of opening-mode fractures in layered brittle materials under uniaxial strain cycling: Journal of Geophysical Research: Solid Earth, v. 97, p. 3381-3396.
Yang, S. Q., D. S. Yang, H. W. Jing, Y. H. Li, and S. Y. Wang, 2012, An Experimental Study of the Fracture Coalescence Behaviour of Brittle Sandstone Specimens Containing Three Fissures: Rock Mechanics and Rock Engineering, v. 45, p. 563-582.
Yukutake, H., 1992, Fracture nucleation process in intact rocks: Tectonophysics, v. 211, p. 247-257.
Zinkernagel, U., 1978, Cathodoluminescence of quartz and its application to sandstone petrology: Contributions to Sedimentology, v. 8: Stuttgart, Germany, Schweizerbart Stuttgart.
Zoback, M. D., 2010, Reservoir geomechanics: Cambridge, Cambridge University Press.

Vita

Yaser Alzayer was born and raised in Dhahran, Saudi Arabia. After graduating from high school, he was awarded a full scholarship to study abroad at the University of Kansas (KU). Yaser was very active as an undergraduate and was a member of several organizations including being an elected president of the International Student Association and a member of the student senate foreign relations committee. He graduated with a Bachelor of Science degree in geology and a minor in business from KU with distinction and was awarded departmental honors for his senior thesis titled Quantifying Slip Rates on Andean Thrust Faults in Colombia and Argentina.

After graduating, Yaser joined Saudi Aramco, the national oil company of Saudi Arabia. During his two years employment at Saudi Aramco he completed several rotational assignments in exploration, carbonates core description, and well site geology. In the fall of 2012, he joined the graduate program in geology at the University of Texas at Austin. Yaser's was part of the Fracture Research and Application Consortium at the Bureau of Economic Geology. During his graduate school career he presented his research in poster sessions at the Jackson School of Geosciences Annual Symposium as well as in the Annual FRAC conference. He also presented a poster at the AAPG Annual Conference and Exhibition in Houston. He plans to pursue a PhD degree after completing his master's degree.

Permanent email: zayer.y@gmail.com

This thesis was typed by the author.